Search for Resonant Slepton Production in a DiMuon + Jets Final State with CMS Data

von

Matthias Endres

Masterarbeit in Physik

vorgelegt der
Fakultät für Mathematik, Informatik und Naturwissenschaften
der
Rheinisch-Westfälischen Technischen Hochschule Aachen

im Oktober 2012

angefertigt am

III. Physikalischen Institut A

Prof. Dr. Thomas Hebbeker

Abstract

Presented is a search for the resonant production of a slepton. The production mechanism is based on an R-parity violating, supersymmetric scenario, called baryon-triality, making use of the CMSSM theory. The search is restricted to the Yukawa coupling λ'_{211} that generates a slepton of the second generation, a single smuon or a muon sneutrino. As final state, the decay into two muons and jets is chosen, a final state that allows to completely reconstruct the slepton mass as well as masses of gauginos that are produced in the slepton decay, as it does not provide a source for missing transverse energy. Several cuts are performed to select the event topology of the signal and reduce background contributions. Thereby is taken advantage of the possible lepton number violation by applying a same charge cut to the muons, that allows to strongly reduce the Standard Model backgrounds. As no significant deviation from the expectation can be observed, limits are set in the plane of the SUSY-parameters m_0 and $m_{1/2}$, exceeding the limits of a direct search from D0, Tevatron significantly.

The search is performed on *pp*-data, that were recorded in 2011 by the CMS experiment at the LHC, CERN, at a center of mass energy of $\sqrt{s} = 7\,\text{TeV}$. The amount of data analysed corresponds to an intgrated luminosity of $4.98\,/\text{fb}$.

Zusammenfassung

Präsentiert wird eine Suche nach resonanter Slepton-Produktion. Die Produktion geschieht auf Basis eines R-Paritäts verletzenden, supersymmetrischen Szenarios, das Baryon-Triality genannt wird und die Theorie des CMSSM nutzt. Die Suche konzentriert sich auf die Yukawa-Kopplung λ'_{211}, die ein Slepton der zweiten Generation, also ein Smyon oder ein Myonsneutrino erzeugt. Der Zerfall in zwei Myonen und Jets ist der gewählte Endzustand. Dieser bietet keine Quelle für fehlende transversale Energie, weswegen es möglich ist, sowohl die Sleptonmasse als auch die Massen von während des Zerfalls erzeugten Eichbosinos zu rekonstruieren. Verschiedene Schnitte werden angewandt, um die Ereignistopologie des Signals zu selektieren und Untergrundbeiträge zu unterdrücken. Dabei wird die mögliche Leptonzahl-Verletzung genutzt, indem auf gleiche Myonladungen geschnitten wird, was den Standardmodell-Untergrund stark reduziert. Da keine signifikante Abweichung von der Vorhersage beobachtet werden kann, werden Limits in der Ebene der SUSY-Parameter m_0 und $m_{1/2}$ bestimmt, wobei sie die Limits einer direkten Suche von D0, Tevatron deutlich übertreffen.

Durchgeführt wird die Suche mit *pp*-Daten, die 2011 vom CMS-Experiment am LHC, CERN bei einer Schwerpunktsenergie von $\sqrt{s} = 7\,\text{TeV}$ aufgezeichnet wurden. Die Menge der analysierten Daten entspricht einer integrierten Luminosität von $4.98\,/\text{fb}$.

Contents

Chapter 1

Introduction

The word that probably is most often mentioned in this thesis is SYMMETRY. Symmetries play a fundamental role in nature. Looking at ones own hands, some principles of symmetries can be seen. For example, it is not possible to twist one hand, so that it matches the other one. Only the help of a mirror allows that operation. Many things in nature show symmetries, from tiny atoms or molecules up to objects like stars or galaxies that have spherical and radial symmetries.

In physics, symmetries are strongly connected to laws of nature. Not only do the symmetric properties of a round star have their origin in physics laws, some symmetries provide fundamental physical follow-up in the sense of conserved quantities. For example the symmetry of space, that means that the outcome of any experiment is independent of the point in space where it is performed, directly leads to the conservation of momentum. In particle physics, looking at the most fundamental parts of matter, symmetry principles are rediscovered. The discovery of antiparticles is a very famous example. Particles and antiparticles are absolutely equal (symmetric) except for their charges.

So far, symmetries run like a golden thread from particle physics to daily life. But there is another golden thread closely connected to symmetries. This is the breaking of those. Coming back to the example of the hands it becomes comprehensible, that when having a closer look, there are small differences between both of them that do not follow the symmetry principle. The same can be observed for stars, galaxies and so on. Also in the case of symmetries connected to physics laws this breaking can be observed. When having a close look, in quantum physics extremely small deviations of some conservation laws appear. And also the matter-antimatter symmetry is obviously somehow broken: Otherwise matter and antimatter would have annihilated after the big bang.

This thesis deals with the search for a hypothetical symmetry very similar to the antimatter symmetry. It is called Supersymmetry, uses another very fundamental property of particles, their spin, and is a possible extension to the Standard Model. Symmetry breaking also plays an important role in this theory.

The Standard Model (SM) of elementary particle physics was developed in the last century. It is the theory of the most fundamental particles and their interactions that form the world we live in. Most theoretical predictions given by the model can be experimentally tested and confirmed with extreme accuracy. Nevertheless some questions still need to be answered and some mysteries still need to be solved. For instance, the existence of the Higgs-Boson needs to be proven and the nature of approximately 95% of our Universe is completely unknown. The latter are called Dark Matter and -Energy. For this reason and in spite of several decades of research, elementary particle physics is a very active field of ongoing studies.

The Standard Model will be introduced in the next chapter before concentrating on an introduction of the theory of Supersymmetry. After that, the experiment that was used for this search is presented, followed by the description of the analysis performed.

Chapter 2

Theoretical Foundations: The Standard Model

If no other references are given, this chapter is based on [1].

2.1 Overview

The theory describing the most fundamental parts our universe consists of, as well as their interactions, is the so called Standard Model of Particle Physics. It was developed in the last century when new particles where discovered when collisions and decays of other particles where examined. As it was done before when developing the Periodic Table of Elements, one tried to sort systematically the new particles to find the underlying structure. The situation known today is as follows:

The particle zoo can be divided in two major groups, which are the fermions (Spin $\frac{1}{2}$) and bosons (integer Spin). The first group contains the particles that form the known matter and is divided into subgroups: The leptons and the quarks. Both of them are again divided into three so called families or generations (compare table 2.1).

Concentrating on the **Leptons**, each family contains one charged lepton (l) and a neutral neutrino (ν) that hardly ever interacts with matter and thus is able to pass through most barriers. The charged lepton of the first family is the well known electron (e), the others are called muon (μ) and tau (τ), which have equal properties but higher masses. Accordingly, the neutrinos are called ν_e, ν_μ, ν_τ.

Quarks have charge $\pm\frac{2}{3}$ or $\pm\frac{1}{3}$, each family containing two quarks with one of the charge configurations. A single quark cannot be observed. They always appear in combinations of three or at least two quarks. Such combinations are called hadrons, in particular a $q\bar{q}$-pair is called a Meson, a drilling Baryon.

The stable matter our environment consists of is composed of particles from the first family. For example, the most famous baryons consisting of first family quarks are the proton (uud) and the neutron (udd). They form the nucleus of an atom which is surrounded by the first family lepton, the electron. With higher family numbers, the particles tend to have higher masses and thus become unstable. That means if they are produced, they will more or less quickly decay into particles of lower families (e.g. $\mu \rightarrow e + \nu_\mu + \bar{\nu}_e$).

So far the matter particles were described, but how do they interact? That is the function of the **Bosons** (see table 2.2). Four interactions are known. The electromagnetic force is the force underlying the interaction of charges. It is for example responsible for the electrons to stay on their orbits outside the nucleus. The weak force causes decays of composed particles like nuclei. It converts fermions into each other. Its particles are the

Family	1	2	3
Leptons (mass)	**e** (511 keV) $\boldsymbol{\nu_e}$ (< 2 eV)	$\boldsymbol{\mu}$ (105.7 MeV) $\boldsymbol{\nu_\mu}$ (< 0.2 MeV)	$\boldsymbol{\tau}$ (1.78 GeV) $\boldsymbol{\nu_\tau}$ (< 18.2 MeV)
Quarks (mass)	up (**u**) ($1.7 - 3.3$ MeV) down (**d**) ($4.1 - 5.8$ MeV)	charm (**c**) (1.27 GeV) strange (**s**) (101 MeV)	top (**t**) (172 GeV) bottom (**b**) (4.19 GeV)

Table 2.1: The Fermions ($S = \frac{1}{2}$), values taken from [2]

Force	Boson	Mass	Spin	Charge	Range /m
Electromagnetic	Photon ($\boldsymbol{\gamma}$)	0	1	0	∞
Weak	Z/W ($\mathbf{Z^0}/\mathbf{W^\pm}$)	91.2/80.4 GeV	1	$0/\pm 1$	10^{-13}
Strong	Gluon (**g**)	0	1	0	10^{-15}
Gravity	Graviton (**G**)	0	2	0	∞

Table 2.2: The Bosons, values taken from [2]

W for the charged- and the Z for the neutral current. Quarks interact via the strong force. That means, that baryons are held together by gluons, the bosons of the strong force, that are also responsible for the stability of atomic nuclei. The fourth force, gravity, is responsible for the interaction of masses and such the formation of stars, solar systems, galaxies and so on. Until now, it cannot satisfactorily be described similarly to the other forces and no sign of the graviton as the particle of the interaction has been discovered yet.

The theoretical formulation of the particles and their interactions as well as some additions to the Standard Model will be described in the following sections.

2.2 Gauge Theories

The Standard Model is formulated as a locally invariant gauge theory:

In analogy to the Lagrange formalism of classical mechanics, where the motion of a particle is described by the Lagrange function, in particle physics a relativistic, quantised solution is used, that considers the spin of the particles.

In this case, the Lagrange function describes the field the interaction is based on. It is called the "Lagrangian" $\mathcal{L}$ and inserted into the Euler-Lagrange equation

$$\partial_\mu \left(\frac{\partial \mathcal{L}}{\partial \left(\partial_\mu \Psi_i \right)} \right) = \frac{\partial \mathcal{L}}{\partial_\mu \Psi_i}. \tag{2.1}$$

The solutions Ψ_i are fields that describe the particle. In case of the basic interactions of the Standard Model, they are called *spinor* and describe the fermions. Other possibilities exist and will be described later.

Lagrangians are invariant under global gauge transformations:

$$\Psi \rightarrow e^{i\Theta}\Psi \tag{2.2}$$

Also claiming invariance under local transformation leads to interesting consequences. Doing so is motivated by the fact, that a shift in space should not change the physical conditions:

$$\Psi \rightarrow e^{i\Theta(x)}\Psi \tag{2.3}$$

When this modified spinor is inserted into equation the Lagrangian, terms appear because of the derivation of $\Theta(x)$. To let the complete lagrangian be invariant under local transformation, new terms have to be added that absorb those of the derivation. As it turns out, these extra terms are able to exactly describe the interaction particles we observe, the gauge bosons. An explicit example of this principle will be shown in the following section, introducing quantum electro dynamics.

2.3 Quantum Electro Dynamics

In Quantum Electro Dynamics (**QED**) one has to find the Lagrangian for a spin$\frac{1}{2}$ vector-field. The result is the Lagrangian:

$$\mathcal{L} = \left[i\hbar c\overline{\Psi}\gamma^{\mu}\partial_{\mu}\Psi - mc^2\overline{\Psi}\Psi\right] - \left[\frac{1}{16\pi}F^{\mu\nu}F_{\mu\nu}\right] - \left(q\overline{\Psi}\gamma_{\mu}\Psi\right)A_{\mu} \tag{2.4}$$

This solution already implies several steps. The first term in the brackets is the lagrangian of a free Dirac fermion. It is invariant under global gauge transformation but not for a local one. The other terms, with $F^{\mu\nu} = (\partial^{\mu}A^{\nu} - \partial^{\nu}A^{\mu})$ and the vector field A^{μ} need to be introduced to guarantee local gauge invariance. Latter is only possible if the new field is massless.

The gauge transformation is a multiplication with a unitary matrix (in this case 1×1):

$$\Psi \rightarrow U\Psi, \text{ with } U^{\dagger}U$$

The outcome of this operation is that a new massless field A_{μ} was introduced, that represents the photons. They are the gauge bosons of the electromagnetic interaction and couple to any charged particle. As they are not charged, a selfcoupling is forbidden.

Using other symmetry groups (SU_3, SU_2), it was found that it is possible to describe the other interactions in the same manner. This will be shown in the following sections.

2.4 Quantum Chromo Dynamics

The same principle as before in now applied using a SU_3 symmetry group. The Dirac Spinor is now a three component vector. Each component stands for a colour and is a four component Dirac spinor itself:

$$\Psi = \begin{pmatrix} \Psi_r \\ \Psi_b \\ \Psi_g \end{pmatrix} \tag{2.5}$$

The result are eight new gauge fields that represent the gluons with their different colour charges. As they are carriers of the strong force and unlike the photons of QED are charged themselves (in terms of colour), they interact with each other as well as with quarks. Due to the description of the colour charge, this theory is referred to as Quantum Chromo Dynamic (**QCD**).

Summing up, each quark exists in three different types (r, b, g) that define the strong charge, the colour. They interact through the exchange of gluons, that carry colour themselves and are able to self-interact. Quarks are always combined into bound states of two or three, whereas the combined state itself is colour-neutral. For baryons every three colours have to be present, in mesons colour and anti-colour are combined.

2.5 Electro Weak Interaction

The weak interaction is connected to the families (flavours) of leptons and quarks and thus is called Quantum Flavour Dynamic (**QFD**). There are two "types" of weak interaction. One with the exchange of charges resulting in changes of the flavour and a neutral one that causes pair production and annihilation. They are called charged- (CC) and neutral current (NC).

The charged current has one remarkable characteristic: It maximally violates parity by only coupling to left-handed particles. The chosen symmetry group is $SU(2)_L$, its charge is called the *weak isospin I*. Left handed fermions are sorted in isospin doublets. Right handed neutrinos do not exist, hence the remaining right handed fermions are isospin singlets.

That leads to a problem: A third (neutral) current is predicted that cannot be identified as the neutral Z^0-Boson as that one also couples to right handed particles. The solution is to include the electro-magnetic current and to introduce an analogon to the weak isospin, the hypercharge Y:

$$Q = I^3 + \frac{1}{2}Y \tag{2.6}$$

with the electromagnetic charge Q and the third component of the weak isospin I^3. Thus a $SU(2)_L \times U(1)_Y$ gauge group was built which is a unification of the weak and electromagnetic forces. Using that in a locally invariant gauge symmetry leads to four bosons: W^1_μ, W^2_μ, W^3_μ and B_μ. The latter two are neutral. Linear combinations of them lead to the known (table 2.2) measurable gauge bosons:

$$\begin{aligned} W^\pm_\mu &= \sqrt{\frac{1}{2}}\left(W^1_\mu \mp i W^2_\mu\right) \\ A_\mu &= B_\mu \cos\theta_W + W^3_\mu \sin\theta_W \\ Z_\mu &= -B_\mu \sin\theta_W + W^3_\mu \cos\theta_W \end{aligned} \tag{2.7}$$

whereas A_μ is the massless Photon and Z_μ is the Z^0-Boson. θ_W is called the electroweak mixing angle or Weinberg angle that cannot be calculated but has to be measured.

So far the Standard Model is able to describe the known interactions and phenomena with high accuracy. But there is one considerable discrepancy between the model's prediction and the observation from measurements. It will be described in the following section and a possible solution will be presented.

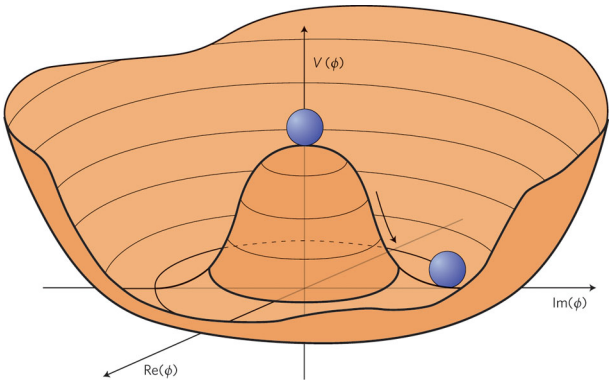

Figure 2.1: The symmetric Higgs potential with an asymmetric ground state. From [5].

2.6 The Higgs Mechanism

The Standard Model described in the previous section is not able to describe the masses of the weak gauge bosons W and Z. In fact, the gauge bosons that appear when locally invariant symmetry is considered have to be massless, otherwise invariance is not possible. This is a great discrepancy to the measured masses of ≈ 90 GeV (compare table 2.2). A possible solution is the principle of spontaneous symmetry breaking and the so called Higgs Mechanism, proposed by Peter Higgs.

Following this idea, a new complex field

$$\Phi = \Phi_1 + i\Phi_2 \tag{2.8}$$

is added into the lagrangian:

$$\mathcal{L} = \frac{1}{2}\left(\partial_\mu \Phi\right)^* \left(\partial_\mu \Phi\right) + \frac{1}{2}\mu^2 \left(\Phi^* \Phi\right) - \frac{1}{4}\lambda^2 \left(\Phi^* \Phi\right)^2 \tag{2.9}$$

That contains a potential that is symmetric but does not have its minimum at 0. Thus, the lagrangian and therewith the equations of motion stays symmetric, while the energetic ground state is not (compare fig. 2.1). The additional term is then expanded around the minimum of the potential leading to terms in the lagrangian that explain the masses of the weak gauge bosons as well as a new particle of mass $\approx 100\,\text{GeV}$ and interaction terms. Masses of other particles can be explained by their interactions with that new Higgs field.

On 4th of July this year, the two CERN experiments CMS and ATLAS held an open seminar of the latest results of the Higgs Boson searches. There, they announced the discovery of a new Boson with a significance of about five standard deviations. The new Boson has a mass of about 125 GeV (see figure 2.2). The final prove, that it really is the Higgs Boson that was found, still has to be given [3][4].

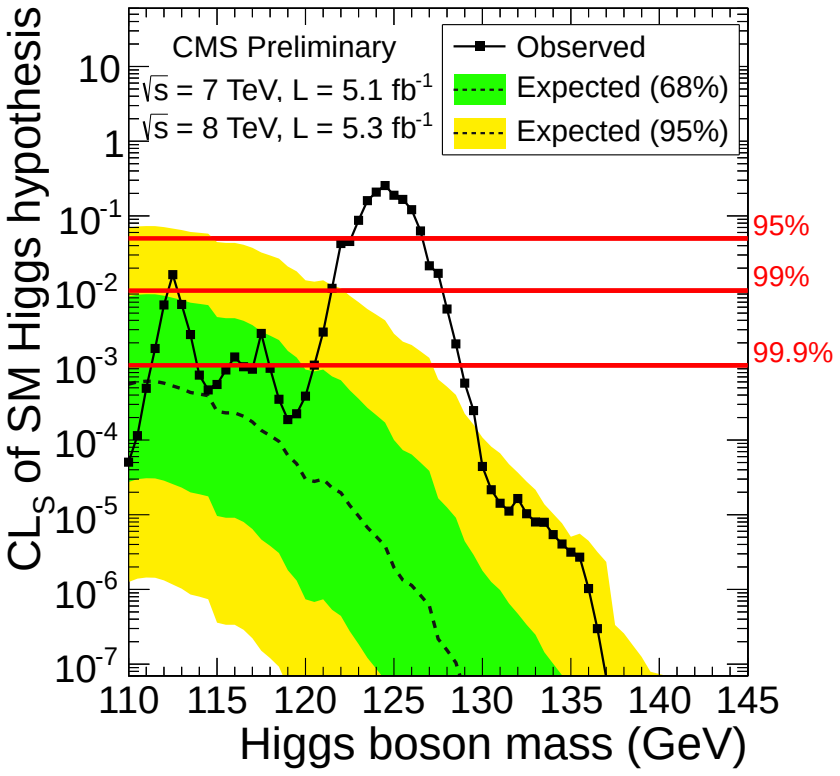

Figure 2.2: Significant excess in the combined Higgs search at 125 GeV. Taken from [4]. It shows the value of CL_s depending on the Higgs boson mass. CL_s is a measure for the confidence into either a signal- or a background hypothesis (compare sec. 5.7). The dashed line with the coloured error bands shows the expected result of CL_s as computed just from simulations under the assumption that no Higgs exists. The dots represent the measured results. A signal hypothesis is excluded by CL, if $1 - CL_s < CL$, as given by the horizontal red lines.

Chapter 3

Supersymmetry

3.1 Limitations of the Standard Model

Assuming the proof for the Higgs will be found soon, confirming the formulation of a locally invariant gauge theory, there are still several gaps, discrepancies and unsolved questions. Three of them, that will be presented here, can be explained by an extension to the Standard Model, called Supersymmetry, that is introduced in this chapter and gives the theoretical basis for this thesis.

3.1.1 Dark Matter

One unsolved mystery comes from astronomy/cosmology and is called Dark Matter. It was discovered that the amount of matter that can be observed is not able to explain the gravitational effects that were measured. For example, when examining the rotational spectra of galaxies, it was noticed that the velocity of stars moving around the center of a galaxy did not fulfil the expectation. The stars were discovered to move much too fast with increasing distance from the center, so that the galaxy would dissolve if it was not held together by additional masses [6].

One can think of several possibilities such as not self illuminating masses like cold gas or small stars where the fusion was not initiated ("brown dwarfs"). Unfortunately all these are not able to explain the effect as the amount of matter needed is so high, that they would become visible by the absorption of light emitted by more distant sources. The dark matter has to have mass to provide the gravitational effects but cannot interact via the electromagnetic force in order to stay invisible. At that point particle physics is needed if one assumes that these particles were created in early times by some fundamental mechanism. QCD is not able to be the underlying mechanism, as its coupling is much to strong and would allow a direct discovery without much effort. The weak force is a popular candidate for that task, that is why the hypothetical particles are called weakly interacting massive particle ("WIMP"). Some models of supersymmetry are able to provide a particle with exactly that properties, an effect that is sometimes called the WIMP-miracle.

3.1.2 Gauge Coupling Unification

There were multiple cases in the past, where physical interactions (forces) were successfully unified. Maxwell, for example, showed that magnetic and electric forces have a common origin, the electro-magnetic force. Later on, as described in chapter 2.5, the electromagnetic force was unified with the weak force. Physicists would like to continue with that principle to discover a possible underlying single unified force, all other interactions are

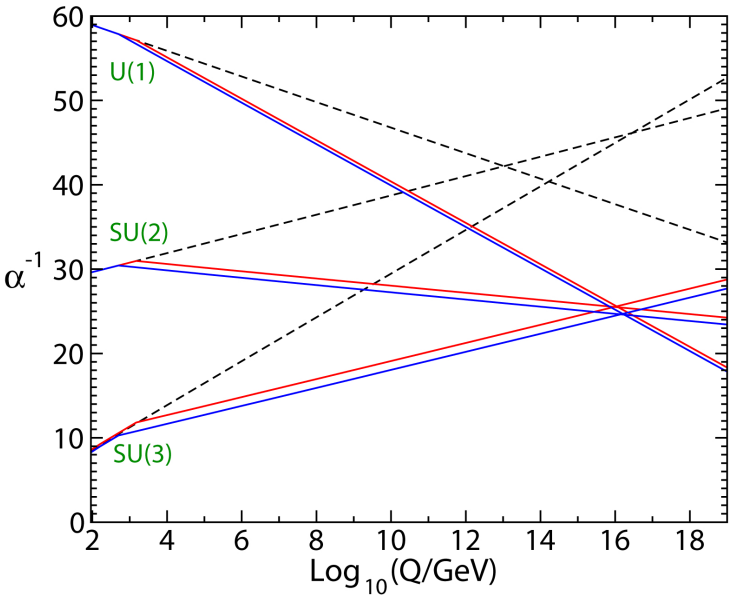

Figure 3.1: Unification of gauge couplings at the GUT-scale. Dashed lines show the Standard Model case, coloured lines could be realised in a SUSY scenario.
Taken from [7]

based on. If the coupling constants of the Standard Model, which are not constants with respect to the energy scale, would meet at a single point, this would give a strong hint for a unified theory. Unfortunately, according to today's knowledge that is not realized by the known forces (compare figure 3.1). The striking discovery was, that introducing Supersymmetry would result in the fact, that all gauge coupling constants (at least electromagnetic, weak and strong force) meet in one point. The energy scale of that point is usually called the GUT (Grand Unified Theory) -scale and is estimated to be at $\approx 10^{16}$ GeV (see figure 3.1, coloured lines).

3.1.3 The Hierarchy Problem

The measurable mass of the Higgs boson (if it exists) consists of several components. On the one hand the bare mass of the boson, on the other hand contributions from additional quantum loop corrections. The bare mass is expected to be of the order of 100 GeV. The loop of a fermion (figure 3.2(a)) would for example lead to a corrective term

$$\Delta m_H^2 = -\frac{|\lambda_f|^2}{8\pi^2}\Lambda_{UV}^2 + \ldots, \tag{3.1}$$

where Λ_{UV}^2 is an ultraviolet momentum cut-off parameter that is needed to prohibit a phase space integral from diverging and usually is chosen to be at the order of the Planck scale [7]. That means, to add up to a Higgs mass of about 100 GeV, the bare mass has to be fine tuned, that is to say up to 30 orders of magnitude, which is very unlikely. But the problem can be solved by adding new particles with the same properties as those that are responsible for the corrections, but the fact that they are scalars. In that case the additional loop corrections would cancel the Standard Model corrections and the hierarchy problem is solved (fig. 3.2(b)). That exactly is the concept of Supersymmetry that will be introduced in the next section.

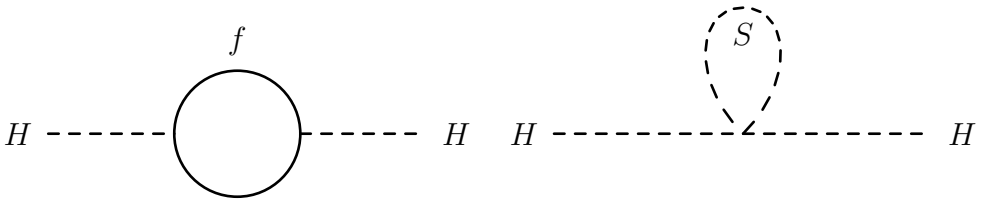

(a) Fermionic contribution. (b) Additional scalar loop.

Figure 3.2: Corrective terms to the bare Higgs mass.

3.2 Introduction to Supersymmetry: The MSSM

Supersymmetry was invented as some kind of thought experiment: It was wondered what would happen if the spin properties of the particles are changed, converting fermions into bosons and vice versa. It was found that this assumption would allow to solve the problems described in the previous section. In supersymmetry theories, these new particles are added to the particle content of the Standard Model. This means, that every particle gets its supersymmetric partner, or superpartner. Thus, supersymmetry is a symmetry of spin properties:

$$Q\,|Boson\rangle = |Fermion\rangle\,;\; Q\,|Fermion\rangle = |Boson\rangle \tag{3.2}$$

The fermions have a scalar partner which is indicated by an *s* at the beginning of the partner's name, they are called sfermion (slepton, selectron, smuon, squark, sup, ...). The superpartners of bosons are given the suffix *-ino* (gaugino, bosino, photino, Wino, ...).

Both, particle and its superpartner are combined to so called supermultiplets. Unlike the Standard Model, multiple Higgs Bosons are needed, that are sorted in two supermultiplets. Without those, Supersymmetry would on the one hand lead to gauge anomalies like those that were previously avoided, now with Higgsino loops. On the other hand, the electroweak symmetry breaking requires two Higgs supermultiplets in the supersymmetric extension. Table 3.1 sums up all multiplets.

Like in the Standard Model, where the measurable electroweak gauge bosons ($W^{\pm}$, Z^0, γ) are superpositions of the gauge eigenstates $W^{1,2,3}$ and B (compare sec. 2.5), the measurable (if existing, of course!) gauginos are combinations of different eigenstates including those of the higgs multiplets. Thus, the neutral gauginos, called neutralinos consist of:

$$\tilde{B}^0, \tilde{W}^0, \tilde{H}_u^0, \tilde{H}_d^0 \overset{\text{mix to}}{\rightarrow} \tilde{\chi}_{1,2,3,4}^0 \tag{3.3}$$

and the charginos:

$$\tilde{W}^{\pm}, \tilde{H}_u^+, \tilde{H}_d^- \overset{\text{mix to}}{\rightarrow} \tilde{\chi}_{1,2}^{\pm} \tag{3.4}$$

The Higgs gauge eigenstates also mix to mass eigenstates:

$$H_u^0, H_d^0, H_u^+, H_d^- \overset{\text{mix to}}{\rightarrow} h^0, H^0, A^0, H^{\pm} \tag{3.5}$$

This is the easiest solution of a supersymmetric theory and usually called the *Minimal Supersymmetric Standard Model* or **MSSM**. The terms of the Lagrangian that describe Supersymmetry are called the *superpotential* that is given by:

$$W_{MSSM} = \bar{u} y_u Q H_u - \bar{d} y_d Q H_d - \bar{e} y_e L H_d + \mu H_u H_d \tag{3.6}$$

Names	Acronym	spin 0	spin $\frac{1}{2}$
(s)quarks	Q	$\left(\tilde{u}_L\ \tilde{d}_L\right)$	$(u_L\ d_L)$
(3 families)	$\bar{u}$	$\tilde{u}_R$	u_R
	$\bar{d}$	$\tilde{d}_R$	d_R
(s)leptons	L	$(\tilde{\nu}\ \tilde{e}_L)$	$(\nu\ e_L)$
(3 families)	$\bar{e}$	$\tilde{e}_R$	e_R
Higgs (-inos)	H_u	$(H_u^+\ H_u^0)$	$\left(\tilde{H}_u^+\ \tilde{H}_u^0\right)$
	H_d	$\left(H_d^0\ H_d^-\right)$	$\left(\tilde{H}_d^0\ \tilde{H}_d^-\right)$
		spin $\frac{1}{2}$	spin 1
gluino, gluon		$\tilde{g}$	g
W (-ino)		$\tilde{W}^\pm\ \tilde{W}^0$	$W^\pm\ W^0$
B (-ino)		$\tilde{B}^0$	B^0

Table 3.1: The supermultiplets: chiral multiplets in the upper part, gauge multiplets below. Adopted from [7]

The y parameters are the Yukawa couplings. They are 3×3 matrices in family space [7]. The other symbols are the supermultiplets that describe the interacting particles and are listed in table 3.1.

3.3 Supersymmetry Breaking: The CMSSM

Supersymmetry has to be broken. This becomes clear when looking at the masses of the (s)particles. Masses of two superpartners cannot be equal, otherwise supersymmetric particles - e.g. a selectron of 511 keV - would already have been discovered. Their masses are therefore significantly larger. This is in contradiction to the MSSM described in the previous section, where sparticles have exactly the same properties as their superpartners but the spin number.

Besides, Supersymmetry needs to be generalized by making it locally invariant. In that case a new force needs to be added. There are several possibilities of which force that could be. For example it is possible to use gravity and the graviton/gravitino as gauge boson. This popular scenario is called *Supergravity* (**mSUGRA**) [8] or *Constrained Minimal Supersymmetric Standard Model* (**CMSSM**) [9].

Similar to the Higgs mechanism of the Standard Model, massless gauge fields appear when local invariance is used on supersymmetry. They are the spin-2 graviton and the spin-3/2 gravitino. Acquiring spontaneous symmetry breaking leads to an additional term, the goldstino, that can be combined with the gravitino, making the latter massive.

The masses of sparticles depend on the energy scale. In a CMSSM scenario it is possible that at a certain point, the GUT scale, the masses of all scalar sparticles, gauginos and higgsinos meet in one point, respectively (compare fig. 3.3). By unifying parameters at that the GUT scale, it becomes possible to reduce the 105 parameters of the MSSM to only five. They are [7]:

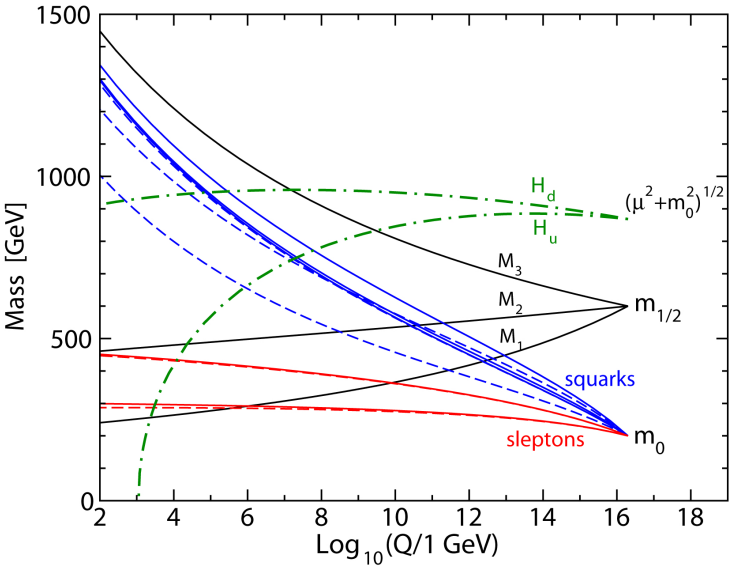

Figure 3.3: Unification of sparticle masses. Taken from [7]

- m_0: The unified mass of scalar sparticles at the GUT-scale
- $m_{\frac{1}{2}}$: The unified mass of gauginos at the GUT-scale
- A_0: Trilinear Higgs-coupling at the GUT-scale
- $\tan\beta$: The ratio of vacuum expectation values of H_u^0 and H_d^0
- $sign\,(\mu)$: The sign of the bilinear Higgsino mixing parameter

3.4 R-Parity and its Violation

Most SUSY-models make use of a quantity called R-parity:

$$R = (-1)^{2S+3B+L} \tag{3.7}$$

R-parity is a multiplicative quantum number consisting of spin (S), baryon- (B) and lepton number(L). It is 1 for Standard Model particles and -1 for sparticles. Usually it is regarded as a conserved quantity. From a theoretical point of view this might be fulfilled, but is not necessary. Both cases, conserved and violated R-parity, lead to remarkable effects that need to be discussed.

If R-parity is **conserved**, supersymmetric particles can only be produced in pairs. For example in colliders when using two Standard Model particles, the combined initial R-parity is $R = 1 \cdot 1 = 1$. The final state needs to have the same R-parity, namely if sparticles are produced $R = (-1) \cdot (-1) = 1$. The conservation also is important for the decay of the possibly produced sparticles. Each further vertex needs to conserve R. That means, if a sparticle decays, always one new sparticle has to be produced as well as one particle. This effect leads to long decay chains (cascades), because the probably short living sparticles fast decay into a lighter sparticle under the emission of one Standard Model particle.

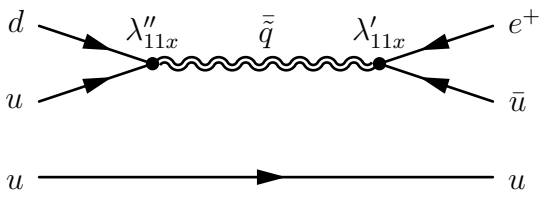

Figure 3.4: A possible proton decay, if lepton- and baryon number violating terms are allowed.

At a certain point, the decay will stop, namely when a sparticle is produced, that is the lightest of the mass spectrum. Such a particle is usually called the *Lightest Supersymmetric particle* (LSP). That one cannot decay further without violating R-parity and thus is stable. If it is also neutral, it is the most favoured dark matter candidate.

3.4.1 R-Parity Violation

As this thesis is about an analysis of an R-parity **violating** (RPV or $\not{R}$) scenario this will be discussed in more detail in the following:

The superpotential 3.6 is in fact not the most general solution that guarantees gauge invariance [7]. For that case, additional terms have to be added. They are [9]:

$$W_{RPV} = \epsilon_{ab}\left[\frac{1}{2}\lambda_{ijk}L_i^a L_j^b \bar{e}_k + \lambda'_{ijk}L_i^a Q_j^b \bar{d}_k + \kappa_i L_i^a H_2^b\right] + \frac{1}{2}\epsilon_{xyz}\lambda''_{ijk}\bar{u}_i^x \bar{d}_j^y \bar{d}_k^z \qquad (3.8)$$

This extension can also be attached to the previously described CMSSM to create a more sophisticated RPV-Model. It consists of four new couplings where superfields (multiplets) interact via the Yukawa couplings λ, λ', λ'' and κ. Thus, the amount of unknown variables (compare sec. 3.3) is increased. The other symbols are the previously described supermultiplets and the antisymmetric tensor ϵ. Indices i, j and k represent the family numbers. The remarkable property of the new terms is that they either violate the lepton number (the terms in the brackets) or the baryon number (the latter term). As R-Parity depends on these numbers (eq. 3.7), it is violated too.

Another effect is that on the one hand, (resonant) single sparticle production is possible, on the other hand no stable LSP is possible and thus the idea of a supersymmetric dark matter candidate has to be abandoned. The decays differ strongly from those of a R-conserving scenario, in particular the cascades are rare, instead it leads to very clear and easily reconstructible signatures as no "invisible" particle needs to leave the detector.

R-Parity was originally introduced to prevent the proton from fast decays. But it can be shown that there exist other $\mathbb{Z}_3$ -symmetries that allow baryon- or lepton number violation and stable protons simultaneously [10], and which are able to serve as the discrete gauge symmetry of the MSSM [11].

Here, the B_3 or baryon triality -symmetry will be used. It only allows the lepton number violating term of the superpotential 3.8, while the violation of baryon number is forbidden. Looking at figure 3.4, it can be seen, that the suppression of λ'' avoids the proton decay. The B_3-model is furthermore able to explain light neutrino masses and their mixing by introducing new higher order mass corrections [12].

3.5 Existing Limits

Until now, no direct hint for the existence of Supersymmetry has been found although every major experiment for particle physics had groups searching for it. Hence, the SUSY parameter space could be excluded over wide ranges. Figure 3.5(a) shows a plot with the m_0-$m_{1/2}$-plane. The coloured lines indicate the exclusion limits of the (RPC-) CMSSM parameters that were found by different analyses that used $\sqrt{s} = 7\,\text{TeV}$ data measured in 2011 with CMS.

Figure 3.5(b) is from a direct search for RPV-SUSY from the D0 experiment at Tevatron [13]. More exactly, it is from a search for resonant slepton production using the yukawa coupling λ'_{211}. It shows the 95% C.L. exclusion limits on λ'_{211} in the m_0-$m_{1/2}$-plane and is until now the most stringent limit on this parameter obtained from a direct search.

A reinterpretation of searches for dijet resonances and like-sign leptons with CMS and ATLAS $\sqrt{s} = 7\,\text{TeV}$-data leads to even stricter limits for the coupling λ'_{211}. For masses of $m(\tilde{l}) = 300\,\text{GeV}$ and $m(\tilde{\chi_0}) = 150\,\text{GeV}$ an upper bound of $\lambda'_{211} < 0.001$ has been found [14]. Figure 3.5(c) shows the results in the slepton-neutralino mass plane.

An indirect limit comes from cosmological neutrino mass constraints or from demanding the absence of tachyons. For a parameter set of $m_0 = 100\,\text{GeV}$, $m_{1/2} = 250\,\text{GeV}$, $A_0 = -100\,\text{GeV}$, $\tan\beta = 10$ and $\text{sign}(\mu) = +$, an upper bound for λ'_{211} of 1.8×10^{-3} is quoted [15].

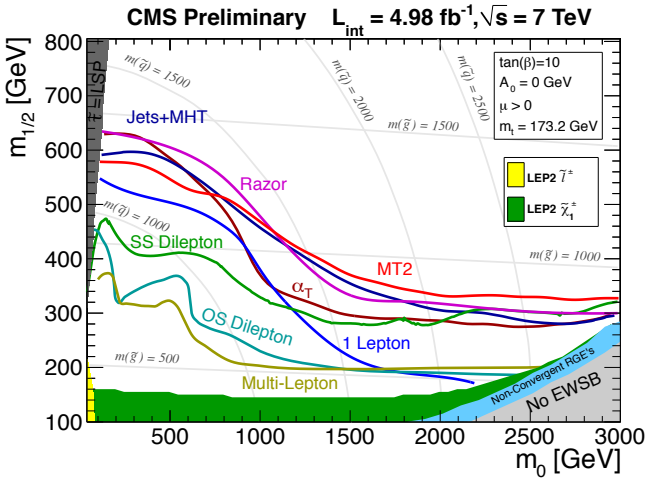

(a) CMSSM exclusion lines in the m_0-$m_{1/2}$-plane. The lines are the results of different CMS-analyses with $\sqrt{s} = 7$ TeV data [16].

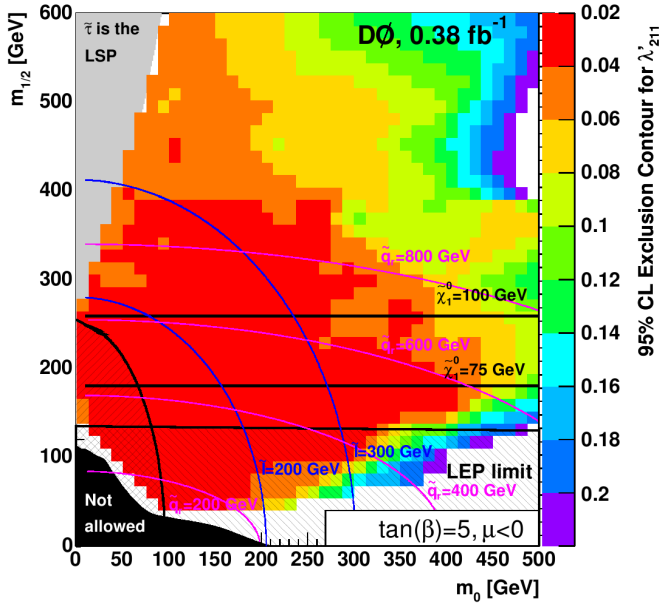

(b) Limits on λ'_{211} from a search for RPV-SUSY at D0, Tevatron [17].

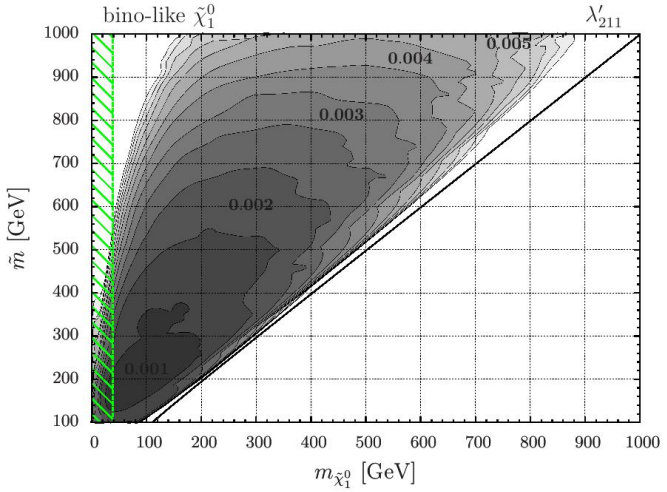

(c) Limits on λ'_{211} from a reinterpretation of searches for like-sign dileptons with ATLAS data [14].

Figure 3.5: Limits of SUSY searches

Chapter 4

Experiment: LHC & CMS

This analysis is based on data that was taken by the CMS experiment at CERN near Geneva during the 2011 period. CMS is part of the LHC complex, the worlds largest and most powerful particle collider. Both, LHC and CMS will be introduced in this chapter.

4.1 The Large Hadron Collider

The Large Hadron Collider (**LHC**) [18] is the worlds largest particle collider. It has a circumference of 26.7 km and was relaunched at the beginning of 2010. The original start was in 2008, but due to a bad electrical connection, several dipoles were destroyed and the launch had to be postponed. Located in the tunnel of the former LEP collider, it can be operated with protons or heavy ions like lead nuclei. As this thesis is based on proton-proton collisions, the following sections concentrate on the use of protons.

During the years 2010 and 2011, LHC was operated with an energy of 3.5 TeV for each beam; In 2012 the energy was raised to 8 TeV. Originally, the machine was designed for a center of mass energy of $\sqrt{s} = 14$ TeV, a goal that had to be postponed after the incident in 2008.

The second relevant property of a collider is its luminosity. The instantaneous luminosity L is a measure for the collision rate delivered by the collider. Integrating with time gives the total luminosity $\mathcal{L}$ from which it is possible to predict the event number of processes of interest. E.g. if one wants to measure a process x, the number of events of that process one can expect is given by

$$N_x = \mathcal{L} \cdot \sigma_x, \tag{4.1}$$

where σ_x is the cross-section of that process.

Before the protons enter the LHC, they are accelerated in several steps using other accelerators (figure 4.1). Protons coming from ionized gas are accelerated in a linear accelerator (LINAC 2) to a kinetic energy of 50 MeV. After that, they enter the Proton Synchrotron Booster (PSB) that increases the kinetic energy to 1.4 GeV. The following steps in the chain are the Proton Synchrotron (PS) accelerating to 25 GeV and the Super Proton Synchrotron (SPS) with 450 GeV. Then the protons are split into two beams and are ready to be injected into the LHC where they are further accelerated to the final energy.

The beam is guided by superconducting dipoles, designed to deliver a magnetic field of 8 T. Beam focussing and cleaning are done by quadrupoles, sextupoles, and octupoles. Acceleration is performed by cavities made from superconducting niobium. There are interaction points, where the beams cross each other's paths. At four of them, the experiments are located where the collisions are performed. The four major experiments are ATLAS [20] and CMS [21], which are huge multi-purpose detectors, as well as LHCb [22],

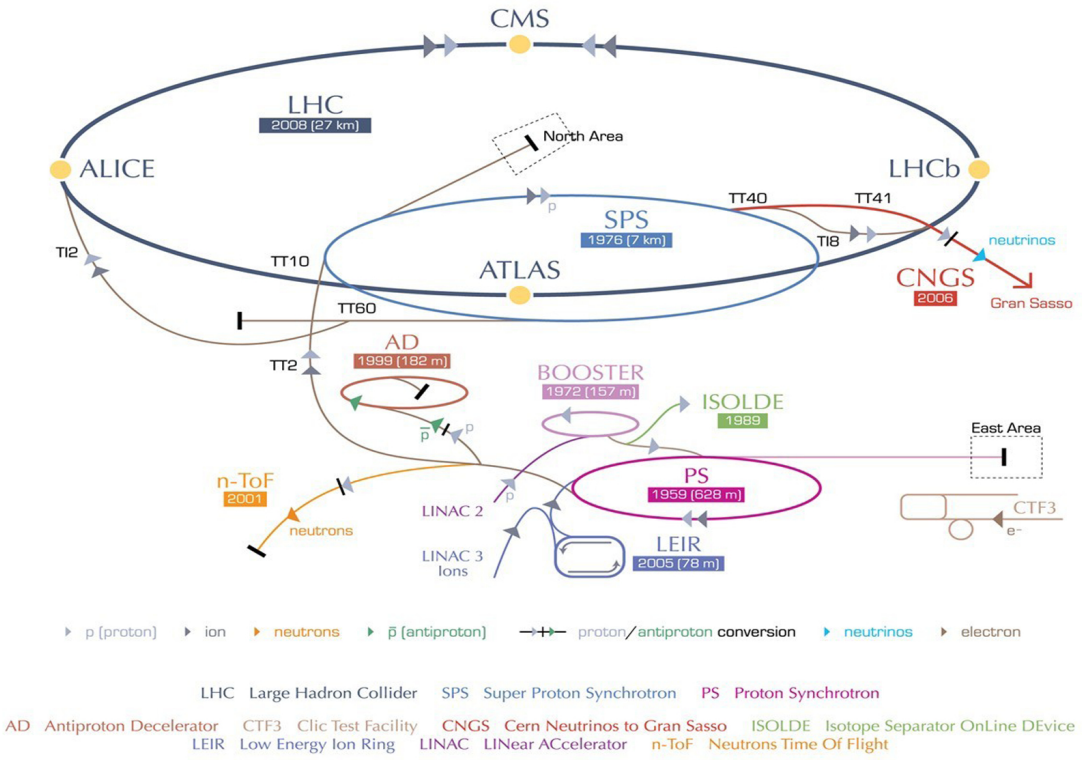

Figure 4.1: The CERN accelerator complex. Adopted from [19].

specialized on physics with b-quarks, and ALICE [23] for heavy-ion studies. CMS will be further presented in the following section.

4.2 The Compact Muon Solenoid

The Compact Muon Solenoid (**CMS**) [21] is a multi purpose particle detector located at LHC's interaction point IP5 in a cavern about 100 m underground near the French town Cessy. It was designed to measure all types of particles that are being produced in collisions by using various subdetectors. Those are arranged in a so called barrel and two endcaps to cover almost the whole solid angle around the interaction point (cf. figure 4.2). Each subdetector is designed to measure different particle properties so that, by combining information from all subdetectors, different types of particles can be distinguished. The subdetectors are presented in the following sections.

There is a coordinate system being defined to describe the orientation of particle tracks inside the detector. The origin is located at the center of CMS, where the collisions are supposed to happen. It is a right handed system with the y-axis pointing upwards, while the x-axis points in the direction of the center of LHC. Thus the z-axis is oriented longitudinally to the beam. The coordinates that are usually used in analyses are the azimuthal angle ϕ, measured with respect to the x-axis, perpendicular to the beam axis. As polar coordinate, the pseudorapidity

$$\eta = -\ln \tan\left(\frac{\theta}{2}\right) \tag{4.2}$$

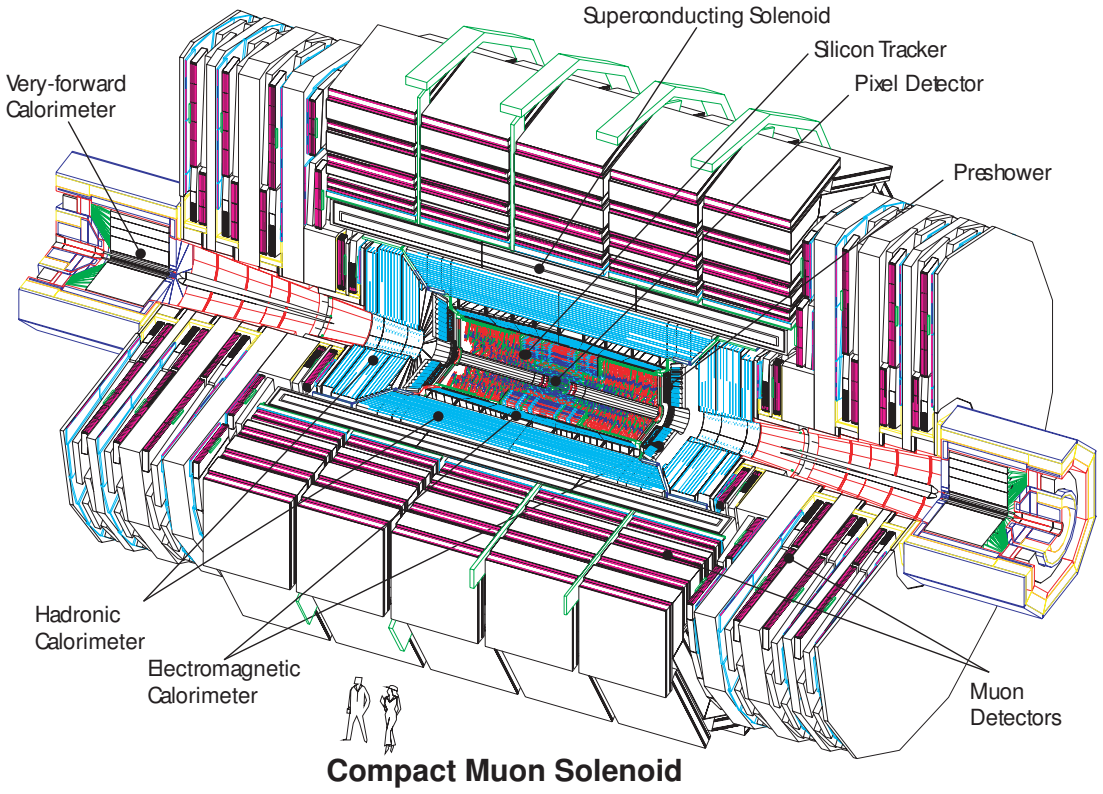

Figure 4.2: View inside the CMS detector [24]

is used instead of the polar angle θ. Differences in pseudorapidity are invariant under Lorentz transformations, a fact that is useful when working with an unknown boost of the rest frame due to the proton substructure. Using the pseudorapidity, a spatial distance can be defined:

$$\Delta R = \sqrt{\Delta\phi^2 + \Delta\eta^2}. \tag{4.3}$$

4.2.1 The Inner Tracker

The inner tracker consists of two different sub-components. They are the pixel- and the strip detector. Like the rest of CMS, both consist of a central barrel part and an endcap. Their task is to precisely measure the tracks of charged particles to determine the momentum using the curvature of the track and to reconstruct single vertices. For that reason, the tracker has to be as close to the beamspot as possible. In that region it has to resist high radiation levels. To handle high luminosities, it needs a fast response. To achieve these goals, both parts are semiconductive detectors made from silicon and approach the beamspot to 4.4 cm.

The **pixel detector** consists of three layers in the barrel part and two layers in the endcap. It measures hits from particles with its overall 66 million pixels, each having a size of $100 \times 150\,\mu\text{m}^2$, that cover an area of $1\,\text{m}^2$.

The **strip detector** on the other hand consists of different sub-components which are the tracker inner barrel (TIB) and tracker inner disc (TID) both located inside the tracker outer barrel (TOB), as well as the tracker end cap (TEC). The measurements are taken

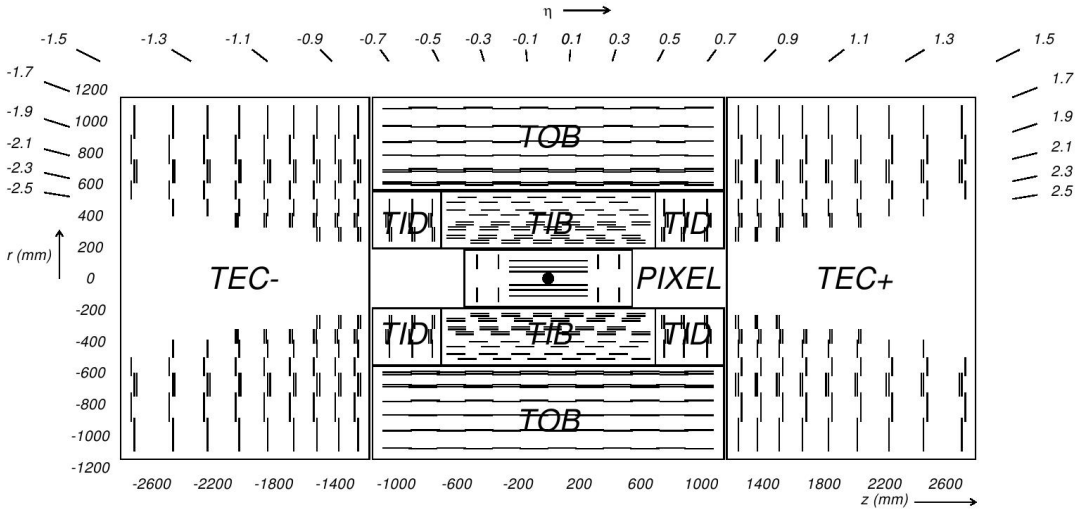

Figure 4.3: The CMS tracker [21]

by several layers. In contrast to the pixel detector, that is able to do a pointlike measurement, the coordinate measurement in the strip detector is reduced to only one dimension. In order to achieve a measurement of the missing coordinate, some layers have an additional strip module that is attached with a stereo angle of 100 mrad. Those modules are illustrated by a double line in figure 4.3. The single strips have a pitch from 80 μm to 184 μm. Overall the inner tracker extends up to a radius of 113.5 cm, covering 198 m^2 with 9.3 million strips. Its point resolution varies from 23 μm in the TIB to 530 μm in the TOB.

The tracker is able to identify single (primary) vertices with an accuracy of 32 μm in z-direction and of the order of the beam position smearing in the transversal plane. The relative transverse momentum resolution is of the order of a few percent: $\sigma_{p_T} \approx 1 - 2\%$ [25].

4.2.2 The Electromagnetic Calorimeter

The electromagnetic calorimeter (ECAL) is vital to measure the energy deposit of light particles, which are basically electrons and photons. It consists of 61200 crystals made from lead tungstate ($PbWO_4$) in the barrel part and 7324 additional crystals in the endcap. The particles are supposed to traverse the inner tracker without loosing too much of their kinetic energy to enter the crystals. There, the molecules of the ECAL material are excited and emit scintillation light. With a length of $220 - 230$ mm, a crystal corresponds to about 25 radiation lengths. The amount of light is a measure for the energy of the initial particle. Light detection is done by avalanche photodiodes (APD) in the barrel part and by vacuum phototriodes (VPT) in the endcaps that are attached to the rear end of the crystals. The front ends of the crystals are smaller than the rear ones so that each crystal faces the nominal beam spot. Their width at the front end (22×22 mm^2) corresponds approximately to one Moliere radius, that is a measure of the width of the electromagnetic shower. Thus a good spatial resolution is guaranteed.

Overall, the ECAL fills a volume of more than 11 m^3 and has a weight of more than 80 t.

It was designed for an energy resolution of

$$\frac{\sigma_E}{E} = \sqrt{a^2 \cdot \frac{\mathrm{GeV}}{E} + \sigma_n^2 \cdot \frac{\mathrm{GeV}^2}{E^2} + c^2}, \tag{4.4}$$

where a is a stochastic term determined by fluctuations, σ_n is the contribution of noise from electronics and pileup, whereas c is a constant [26]. Their design values are $a = 2.8\%$, $\sigma_n = 12\%$ and $c = 0.3\%$.

4.2.3 The Hadronic Calorimeter

Most electrons and photons can be stopped in the ECAL and so their energy can be measured. But the ECAL is not able to completely stop hadrons as the nuclear interaction length is much greater than the electromagnetic one. Massive materials over wide ranges and radiation lengths are needed to fully absorb hadrons. On the other hand, such an absorber would not allow to measure their energy because no photons would reach a detector. That is why the hadron calorimeter (HCAL) is composed of many thin layers of absorber alternating with scintillators.

The HCAL consists of four different subcomponents. They are the hadron barrel (HB), endcap (HE), outer (HO) and and forward (HF) calorimeters. The latter is located outside the main detector in regions of the pseudorapidity ($\eta > 2.7$). Those regions are usually not considered in analyses to reconstruct particles but HF has a significant impact on the calculation of missing transverse energy.

The **HB** is located between ECAL and magnet and extends from radii of 1.77 m to 2.95 m. It consists of 16 layers of absorber material that are made from steel (the outermost) and brass, having thicknesses of $40 - 75$ mm. That corresponds to a minimum of 5.82 interaction lengths in the direction perpendicular to the beam axis. Between the absorbers, the scintillating tiles are located. They are made of plastic and have a thickness of 3.7 mm. Produced light is collected by a wavelength-shifting fibre and finally read out by a hybrid photodiode (HPD).

The **HE** is constructed in the same way as the HB. The only difference is, that stacked layers are transverse to the beam axis in contrast to the parallel ones of the barrel.

The **HO** is located outside the magnet coil. It uses the magnet material as absorber and is supposed to measure hadrons that were not completely stopped in the HB. Thus it is only present in the barrel region of the detector. The barrel wheel 0 contains HO elements with two layers of scintillator each with a thickness of 10 mm, the other wheels only have one.

The combined energy resolution for hadronic showers of both, ECAL and HCAL was designed to reach [27]

$$\frac{\sigma_E}{E} = \sqrt{(100\%)^2 \cdot \frac{\mathrm{GeV}}{E} + 4.5\%}. \tag{4.5}$$

4.2.4 The Magnet

The magnet is necessary to bend the paths of charged particles on their way through the detector. Only in that way momenta can be measured and charges be determined.

As the bending radius largens with increasing momentum, a strong magnetic field is needed. That is why a superconducting magnet was chosen, that produces a field up to 4 T. The magnet is a solenoid, resulting in a magnetic field parallel to the beam axis. The particle trajectories are thus bent in the plane perpendicular to the beam and the transversal component of the momentum -usually called p_T- can be measured. An iron yoke is responsible to return the magnetic field outside the magnet.

4.2.5 The Muon System

For many analyses, both Standard Model and beyond, muons are crucial final state particles. Besides, muons are minimal ionizing particles, meaning they have only very low energy losses due to ionization when they cross matter. As a consequence, it is not possible to do a complete calorimetric measurement of muons as most of them will leave the detector and their momentum has to be reconstructed from the trajectory only. To do the latter with greatest precision, the outermost component is the muon system.

Like the previously described subdetectors, the muon system consists of several subcomponents and is divided into a central barrel part with five wheels and two endcaps to cover a wide solid angle. The components are three different types of gaseous detectors [28] and cover an overall plane of 25000 m^2.

In the wheels, **drift tube** (DT) chambers or -stations are located. They are mounted between the layers of the magnetic return yoke. Each wheel contains four layers of stations. The first three of them contain three superlayers of drift tubes. Of these three superlayers, the outer ones measure the $r-\phi$ component of the momentum, the one in the middle observes only the component in z-direction. In the fourth station, the z measurement is not applied. A superlayer has four layers of drifttubes. The drifttubes, 2.4 m long, are filled with a mixture of argon (85%) and carbon-dioxide (15%). In the middle of every tube (172000 altogether) a wire is located, acting as anode, cathode strips are mounted to the tube walls. A muon that traverses such a tube will ionise the gas and a current can be measured. DTs were chosen in this region because they provide a robust measurement at low rates and magnetic field on the one hand, and are inexpensive on the other hand. A picture of a DT-chamber and a cross section with electric field lines of a drift tube can be seen in figure 4.4

Cathode strip chambers (CSC) are installed only in the endcaps. Overall, there are 468 strip chambers in four layers. They have a trapezoidal shape with angles of 10° or 20° and consist of seven panels that have cathode strips attached to them. The strips are oriented in radial direction pointing towards the beam axis. Perpendicular, in the gas filled gap between the panels, planes of anode wires are located. This layout allows measurements of all coordinates of a muon track. CSCs were chosen for this region because they provide a reliable muon measurement at high rates and in a non-uniform magnetic field. Their spatial resolution in the $r-\phi$-plane is $75-150\,\mu$m.

The third type of muon detector is called **resistive plate chamber** (RPC). RPCs consist of four plates made of phenolic resin with a high electric resistance ($10^{10}-10^{11}\,\Omega$cm) [28]. Between the inner plates, read-out strips are located. Between the two inner plates and their respective outer neighbour is a gas-filled gap. RPCs are operated in avalanche mode and have the advantage of a very fast response leading to high detection rates. In the barrel region, two RPCs are attached to both sides of the two innermost DTs and one

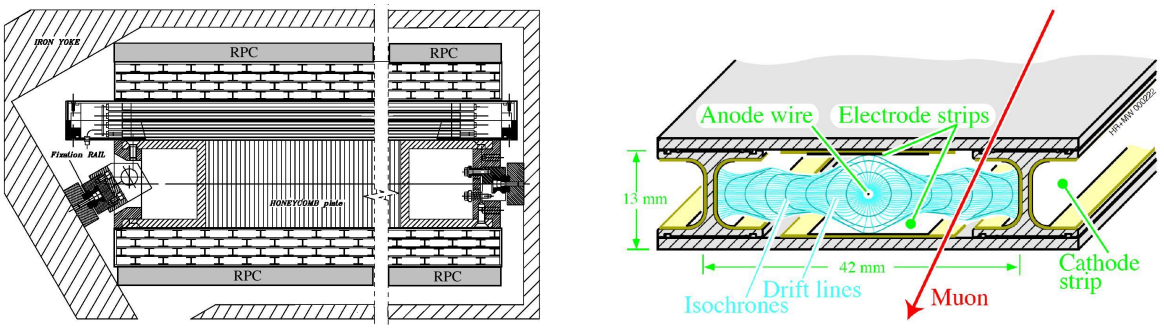

Figure 4.4: Schematic view of a DT chamber (left) and a single drift tube (right) [21]

on the inner side of the two outer DT layers. Here, the readout strips are parallel to the beam axis. In the endcap, overall four layers of RPCs are mounted whereas some are still missing in the high η-region.

The muon momentum resolution can be enhanced by combining the information from the muon system with those from the tracker. On that way, a relative transverse momnentum resolution of 5% can be reached for high energetic muons ($p_T \approx 1\,\text{TeV}$).

4.2.6 Triggering, Data Acquisition and Computing

LHC was designed to deliver bunch crossings in a 25 ns interval, which was reduced to 50 ns in 2011. This corresponds to an eventrate of 40 MHz, and an amount of data (traffic) that is impossible to handle. Therefore it is necessary to reduce the number of recorded events by only selecting those with an interesting physics content. This task has to be done fast before the event is stored. The devices that are supposed to achieve this goal are called triggers.

In CMS, there are two major levels of triggers. The first one, the so called Level-1 (L1) trigger is mainly based on electronic devices and located in different components inside the CMS detector or its (service) cavern. Many single triggers monitoring detector components provide coarse object information that are all collected by a global trigger. The latter makes a rough reconstruction of the event content and decides which events pass the L1 (cf. fig. 4.5). During this time, all the detailed event information have to be stored by the front-end for about 3.2 μs. The L1 reduces the event rate to $30 - 100$ kHz.

The second trigger is the high level trigger (HLT). It is completely software based and runs on commercial processors. Having access to the complete data, it is possible to do more complex selections than the L1. The combination of HLT and L1 reduce the event rate by a factor 10^6 to a few 100 Hz.

Before being sent to the mass storage at the CERN data centre, the data is completely reconstructed and processed at the local storage near the experiment using the CMS reconstruction software CMSSW. From the computing centre, the data is distributed to the different subcentres of the world wide LHC computing grid, the Tier-1 and -2, where it can be accessed by the analysts.

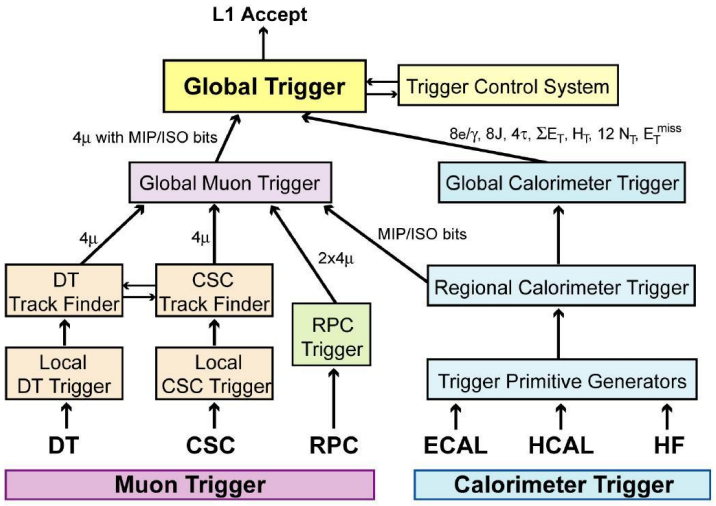

Figure 4.5: The Level-1 Trigger [21]

4.2.7 Particle Reconstruction

All detector components provide certain information about hits they measured. All these have to be collected and combined to reconstruct single physics objects.

Muons can be measured in the muon system and, as they have a charge, in the tracker. In the muon system, the reconstruction is done using a Kalman filter technique [29] that develops a track from a seed with an iterative trajectory building algorithm. Muons that were reconstructed using only information from the muon system are called *standalone muons*. The type of muon mostly used is the *global muon*. In this case, the identification benefits from additional information from the tracker. The trajectory of a reconstructed muon is extended to the surface of the tracker, considering effects from the calorimeter material in between, like multiple scattering and Bremsstrahlung. If a track can be matched, a global muon of higher quality is found [30]. Another possibility is to identify a muon in the tracker, a *tracker muon*. Here, all tracks in the silicon tracker are identified as a candidate muon and then compared to hits in the muon system. If a match is found, the track is used as a muon [31].

Electrons and **photons** are measured and reconstructed using the ECAL. When showering in an electromagnetic cascade, every single electron or photon deposits its energy in a cluster of a size of about 5×5 crystals of the ECAL. The whole cascade is reconstructed by searching for so called superclusters. They result from electron paths that are bent into the ϕ-direction due to the magnetic field, that radiate a photon tangentially. In contrast to photons, it is possible to assign a track to a supercluster when reconstructing an electron. To reconstruct electron tracks, an optimisation of a non-linear Gaussian Sum Filter is used [32].

Jets are clusters of many, mostly hadronic, particles coming from one initial particle like a quark or a gluon. To determine the properties of the latter, those of the complete jet have to be measured. This is done by jet algorithms that combine all secondary particles to one physics object.

An often used **jet algorithm** is the **anti $\mathbf{k_T}$** clustering method [33]. It belongs the class of so called sequential cluster algorithms like the k_T or Cambridge/Aachen algorithms

[34, 35]. These algorithms are collinear and infrared safe. The latter means, that the finding of a jet is not affected by soft radiation. Additionally, the anti-k_T algorithm provides jets with a conical structure of a given radius. Here, anti-k_T jets with a radius $R = 0.5$ will be used.

Because of the high resolution performance of the CMS detector, analyses can benefit from the **particle-flow algorithm** [36]. This algorithm tries to reconstruct every single particle in the event by using all available detector components. Thus it composes the whole event content, meaning every single muon, electron, charged hadron and so on. With these information, for example jets can be measured with much higher precision because also low energetic particles that are bent out of the main jet and lead to separated hits in the calorimeters are assigned to the right jet. With jet measurements just in the calorimeters, this assignment is not possible. Also the resolution for the missing transverse energy is improved, taus can be reconstructed with higher precision and it is possible to reconstruct a more sophisticated charged lepton isolation by measuring the distance to other particles.

Missing transverse energy ($\not{E}_T$ or MET) is calculated by summing up vectorially the transverse energies of all reconstructed objects. The result is the negative $\not{E}_T$. It gives a hint for neutral particles that left the detector undetected, such as neutrinos or possible new particles.

Chapter 5

Analysis

The aim of this analysis is the search for resonant slepton production. That means an RPV-SUSY model is used. Concentrating on the coupling constant λ'_{211} implies, that a smuon or a muon sneutrino is resonantly produced by two quarks (fig 5.1). The slepton can then decay into a lepton and a gaugino that further might decay into a lepton and, again violating RP, into quarks. Other decays are possible, for example the muons can be replaced by neutrinos, or the intermediate gaugino is a chargino that can radiate W- or Z-Bosons. Concerning the decay, the search is limited to the channel with two muons and two quarks (compare fig 5.1).

The latter decision has two major advantages: first of all, as no undetectable neutrino or escaping stable sparticle is produced, the final state is completely reconstructible and hence the mass of the resonantly produced slepton can be measured. Secondly, it is possible to take advantage of the lepton number violation the Yukawa coupling λ'_{211} provides. Thus it is likely (about 50%) that the two muons have equal charges. Using this property for cutting dramatically reduces the Standard Model background and increases the possibility to discover something. More about that in this chapter.

5.1 Datasets

5.1.1 Data

The CMS data that is used for this search was taken during the whole 2011 period with $\sqrt{s} = 7$ TeV. It corresponds to 5 /fb integrated luminosity. The datasets used are dimuon triggered as listed in table 5.1. It shows five data samples of the 2011 period with the

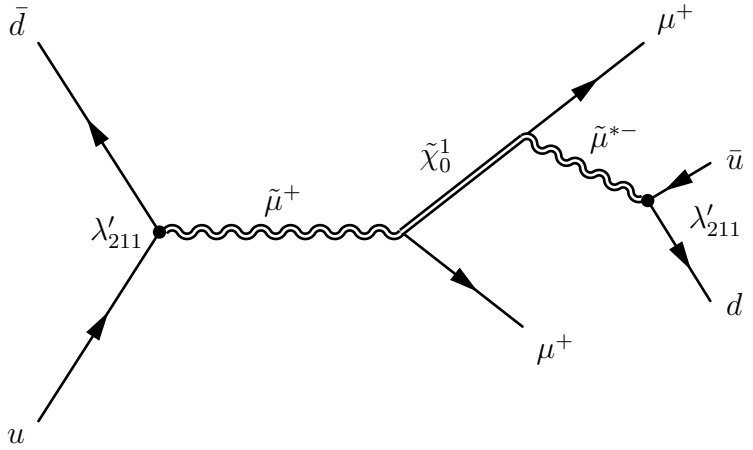

Figure 5.1: An example diagram for the resonant slepton production with two muons of the same charge and jets.

Dataset	Run Range	Int. Lumi.(/pb)
/DoubleMu/Run2011A-May10ReReco-v1/AOD	160431 – 163869	215.0
/DoubleMu/Run2011A-PromptReco-v4/AOD	165088 – 167913	955.3
/DoubleMu/Run2011A-05Aug2011-v1/AOD	170826 – 172619	389.9
/DoubleMu/Run2011A-03Oct2011-v1/AOD	172620 – 173692	706.7
/DoubleMu/Run2011B-PromptReco-v1/AOD	175860 – 180252	2714.0
sum	**160431 – 180252**	**4980.9**

Table 5.1: Used datasets

names in the first column. Thereby, "DoubleMu" means that events that entered this sample need to have triggered any di-muon trigger. The next part of the name describes the period, when the data was recorded. Between run A and B, was a technical stop, when some updates, for example in the trigger table, were applied. The following part describes the date, when the data was published. "AOD", as the names last part is the name of the data format, the data is described with.

The choice of the trigger path is affected by two major problems. First of all, one wants to use triggers that are applied in data as well as they are simulated in Monte-Carlo to create similar conditions. Secondly, the trigger prescale is raised with increasing instantaneous luminosity. A prescale means that not every event that triggers is recorded in order to keep the recording rate constant. When using a prescaled trigger, the effect has to be considered in the integrated luminosity. Triggers tend to be introduced unprescaled and the prescale is then raised in later runs. When that happens, usually a new unprescaled trigger is included that has higher thresholds or tighter requirements. So instead of considering the prescale and loose luminosity, it is possible to change the trigger at that points. This method is used here. Figure 5.2 shows the prescales of the analysis triggers as they developed during the 2011-runs. It can be seen, that each time a prescale raises from one to a higher value, another trigger takes over. In the analysis for each event the shown triggers are required using an *or*-logic under the condition that one of the existing triggers is unprescaled. The used triggers are

- HLT_DoubleMu6
- HLT_DoubleMu7
- HLT_Mu13_Mu8
- HLT_Mu17_Mu8

All of them require two muons. The numbers in their names indicate the p_T-thresholds. Thus, the first two require two muons with $p_T > 6(7)\,\mathrm{GeV}$, whereas the thresholds of the latter two differ for the two muons.

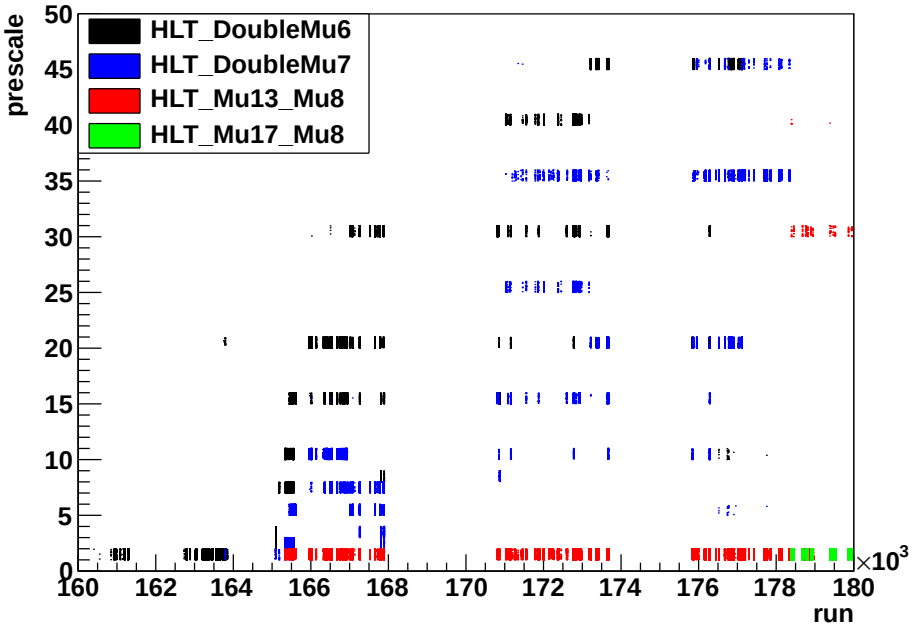

Figure 5.2: The triggers that are used in this analysis. Shown is their prescale factor depending on the run number.

5.1.2 Standard Model Background Monte Carlo

The principle idea of this analysis is to make a prediction, how many events one awaits in a certain channel and distribution and to compare it to the measured data. If the data significantly exceed the prediction, this is a hint that one discovered something. Therefore it is absolutely necessary to have a reliable prediction. This is achieved by using so called Monte-Carlo (MC). Monte-Carlo is a simulation of various physical processes where single events are produced due to their probability to appear within a certain sample.

The theoretical probability for a certain type of event to appear in a given set of data is given by the total integrated luminosity of that set times the cross section of the process. Of course, it is not possible that every analyst produces his own MC corresponding to the amount of data he uses. Hence mc samples are processed centrally and have to be weighted event by event depending on the number of generated events in the sample. The event weight is calculated using the formula

$$w = f \cdot \frac{\sigma \cdot L}{N} \tag{5.1}$$

where σ is the cross section of the process that is simulated, L the integrated luminosity and N is the number of events that were generated in the sample. The factor f can be used to scale the whole mc sample and will be used later. Usually it is 1 or, if not, of the order of 1.

All processes that are able to provide two muons and jets have to be included. Figure 5.3 shows two exemplary diagrams. The Drell-Yan process is the dominating background before applying a same-charge cut on the muons. It provides two muons and with initial state radiation or pileup contamination it is possible to measure additional jets. After

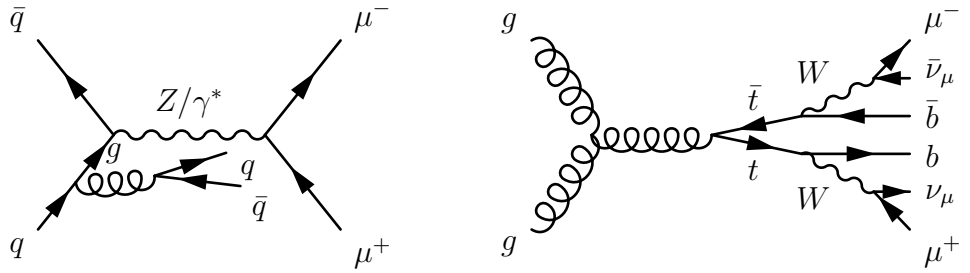

(a) Drell-Yan+Jets (Z/γ^*). (b) Top quark pair production ($t\bar{t}$).

Figure 5.3: The dominating Standard Model background contributions.

this cut, top-quark pair production is dominating. Including possible decays of the b-quarks, two quarks of the same charge are possible. Table 5.2 lists all processes that were considered in this analysis, as well as their cross-section and the Monte-Carlo scale factor that was calculated using equation 5.1.

Most of the samples that are used in this analysis have been produced with the generator Madgraph [37]. The others use Pythia [38] or Powheg that is specialised to heavy quark production [39]. The decay of taus is simulated with Tauola [40]. A detailed list of all used samples with information about the generator that was used can be found in appendix A.

5.1.3 Signal Monte Carlo Production

In contrast to the Standard Model Monte Carlo, there does not exist any centrally produced simulation of the signal processes. Hence this was done within the Aachen RPV-SUSY group. The production chain is only summarized here, for more details see [47].

Two different sets of signal Monte-Carlo were produced. They differ in the choice of the five CMSSM parameters (compare sec. 3.3). The first set is motivated by the choice of the CMS SUSY benchmark points [48, 49]. They are named LMx or HMx, meaning **L**ow **M**ass or **H**igh **M**ass. Those samples are used for signal studies and to find cut values. The parameter constellation of that points is shown in table 5.3. For each point, 100000 events were produced.

The second set was produced to do a wide parameter scan in the m_0-$m_{1/2}$-plane, while the other parameters were set to $\tan\beta = 20$, $sign(\mu) = +$, $A_0 = 0$ and $\lambda'_{211} = 0.01$. The scan is performed in ranges of $100\,\text{GeV} < m_0 < 2000\,\text{GeV}$ in steps of 100 GeV and $50\,\text{GeV} < m_{1/2} < 1000\,\text{GeV}$ with a 50 GeV spacing. For each point, 50000 events were simulated.

Some regions of that plane lead to unphysical solutions that result in no electroweak symmetry breaking, missing Renormalization Group Equation convergence or tachyons. Those points were excluded from the generation procedure, so that a grid of 354 signal samples was left. The grid can be seen in figure 5.4, right.

Monte-Carlo sample	σ [pb]	Weight
$Z/\gamma^* \to ll$ ($10\,\mathrm{GeV} < M(ll) < 50\,\mathrm{GeV}$)	9611	1.530
$Z/\gamma^* \to ll$ ($M(ll) > 50\,\mathrm{GeV}$)	$3048 \pm 34 **$	0.4219
$t\bar{t}$	$165 \pm 10 ***$[41]	0.0167
$W + \mathrm{Jets} \to l\nu$	$31314 \pm 407 **$	2.602
$QCD\ \mu-$Enriched ($15\,\mathrm{GeV} < p_T(\mu) < 20\,\mathrm{GeV}$)	$579.2 \cdot 10^6$	3240.31
$QCD\ \mu-$Enriched ($20\,\mathrm{GeV} < p_T(\mu) < 30\,\mathrm{GeV}$)	$236.3 \cdot 10^6$	663.44
$QCD\ \mu-$Enriched ($30\,\mathrm{GeV} < p_T(\mu) < 50\,\mathrm{GeV}$)	$53.07 \cdot 10^6$	274.34
$QCD\ \mu-$Enriched ($50\,\mathrm{GeV} < p_T(\mu) < 80\,\mathrm{GeV}$)	$6351 \cdot 10^3$	64.41
$QCD\ \mu-$Enriched ($80\,\mathrm{GeV} < p_T(\mu) < 120\,\mathrm{GeV}$)	$785.1 \cdot 10^3$	17.31
$QCD\ \mu-$Enriched ($120\,\mathrm{GeV} < p_T(\mu) < 150\,\mathrm{GeV}$)	92950	2.840
$QCD\ \mu-$Enriched ($150\,\mathrm{GeV} < p_T(\mu)$)	47580	3.633
t (s − channel)	$3.19 \pm 0.06 ***$[42]	0.0611
t (t − channel)	$41.92^{+1.59}_{-0.21} **$[43]	0.0535
t (tW − channel)	$7.87 \pm 0.20 **$[44]	0.0481
$\bar{t}$ (s − channel)	$1.44 \pm 0.01 ***$[42]	0.0520
$\bar{t}$ (t − channel)	$22.65 \pm 0.50 **$[43]	0.0580
$\bar{t}$ (tW − channel)	$7.87 \pm 0.20 **$[44]	0.1212
$WW \to 2l2\nu$	$4.51 \pm 0.16*$	0.0188
$WZ \to 2l2q$	$1.24 \pm 0.05*$	0.0066
$WZ \to 3l1\nu$	$0.60 \pm 0.02*$	0.0024
$ZZ \to 2l2\nu$	$0.238 \pm 0.006*$	0.0010
$ZZ \to 2l2q$	$0.83 \pm 0.02*$	0.0041
$ZZ \to 4l$	$0.060 \pm 0.002*$	0.0003
$W + \gamma \to \mu\nu\gamma$	114.6	1.098
$t\bar{t}W \to 2l^+2\nu$	0.0068	0.0007
$t\bar{t}W \to 2l^-2\nu$	0.0027	0.0003
$t\bar{t}Z \to 2l^+2\nu$	0.0020	0.0003
$t\bar{t}Z \to 2l^-2\nu$	0.0019	0.0003
$W^-W^- \to 2l2\nu$	0.0016	0.0002
$W^+W^+ \to 2l2\nu$	0.0042	0.0004
$WWW \to 2l^-2\nu$	0.0041	0.0013
$WWW \to 2l^+2\nu$	0.0152*[45]	0.0017

Table 5.2: Standard Model Background Monte-Carlo: *NLO, **NNLO, ***NNLL cross-sections. Higher order cross-sections from [46], if no other source is given. Cross sections without further information are from the generator output. The given systematic uncertainties are from the variation of the factorization and renormalization scale. More about that in section 5.6.

Name	m_0	$m_{1/2}$	A_0	$tan(\beta)$	$sgn(\mu)$	σ [pb]	Weight
LM0	200	160	−400	10	+	10.09	0.51
LM1	60	250	0	10	+	18.98	0.95
LM2	185	350	0	35	+	3.23	0.16
LM2mhf360	185	360	0	35	+	3.02	0.15
LM3	330	240	0	20	+	1.71	0.11
LM4	210	285	0	10	+	4.09	0.22
LM5	230	360	0	10	+	2.23	0.11
LM6	85	400	0	10	+	3.71	0.22
LM7	3000	230	0	10	+	$1.41 \cdot 10^{-5}$	$1.1 \cdot 10^{-6}$
LM8	500	300	−300	10	+	0.39	0.020
LM9	1450	175	0	50	+	$3.57 \cdot 10^{-3}$	0.0002
LM9p	1450	230	0	10	+	$3.39 \cdot 10^{-3}$	0.0003
LM9t75	1450	175	0	50	+	$3.57 \cdot 10^{-3}$	0.0002
LM10	3000	500	0	10	+	$8.46 \cdot 10^{-6}$	$5.3 \cdot 10^{-7}$
LM11	250	325	0	35	+	2.33	0.12
LM12	2544.58	246.56	−865.75	47.59	+	$5.04 \cdot 10^{-5}$	$2.6 \cdot 10^{-6}$
LM13	270	218	−553	40	+	3.34	0.17
HM1	180	850	0	10	+	0.21	0.01
HM2	350	800	0	35	+	0.16	0.008
HM3	700	800	0	10	+	$4.20 \cdot 10^{-2}$	0.002
HM4	1350	1350	0	10	+	$3.6944 \cdot 10^{-3}$	0.0002

Table 5.3: Signal points following the CMS benchmark points [48, 49]

The parameters of each point were entered into SoftSusy 3.1.7 [50, 51] to compute the sparticle mass spectrum. These results enter Isajet 7.64 [52] to compute the decay widths and branching ratios.

The event production was then performed with Herwig 6.5 [53, 54] which provides parton showering hadronisation and decays and that was updated to be able to handle supersymmetric processes, including the simulation of PDFs , the underlying event, the Fall11 pileup scenario and the detector response.

With a NLO calculator [55] the NLO k-factors were calculated. Figure 5.4, left shows the NLO correction to the resonant smuon production with respect to the smuon mass, while the plot on the right side shows the LO cross sections of the grid signal points. The k-factors vary from 1.17 to 1.40 and tend to decrease with higher values of m_0 while they change little with $m_{1/2}$.

5.2 Signal Properties

Before searching for signs of the signal within real data, the produced signal and its properties have to be examined carefully. For that purpose, it is useful to take advantage

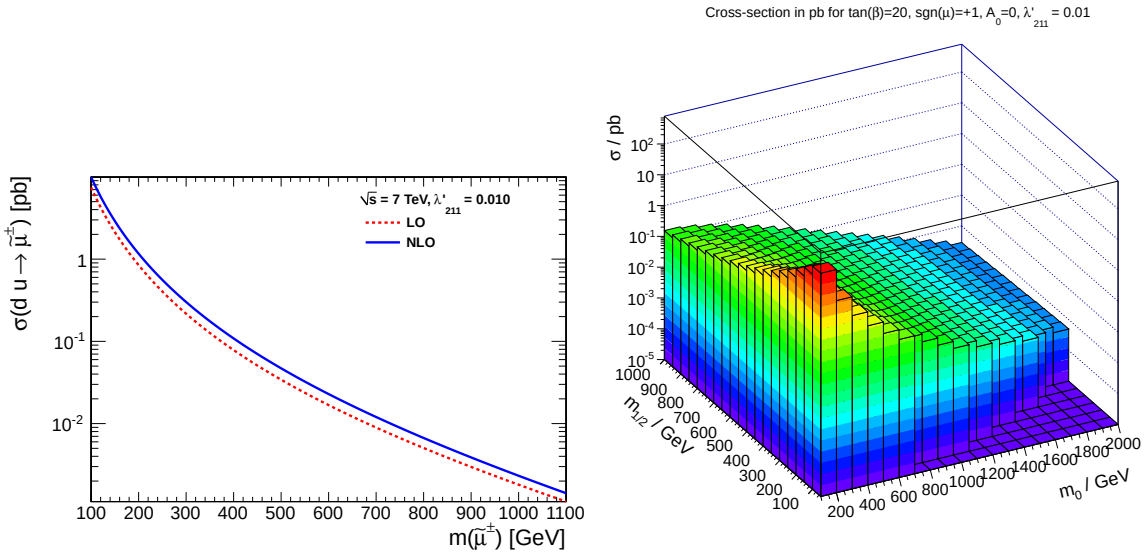

Figure 5.4: Left: Cross section and NLO correction of the resonant smuon production depending on the smuon mass; Right: Cross sections of the signal grid. Both plots from [47]

of generator informations. Those are details saved from different steps of the Monte-Carlo production chain, like tree-level information before the parton-showering or about single particles after that. Physics objects (muons, quarks, etc.) on generator level are referred to as gen-particles. After the full simulation including the detector, they are CMS RECO-objects.

For this study the signal samples are used that were produced using the parameters of the CMS-benchmark points (cf. table 5.3). The plots presented here show three example points that are LM1, HM1 and HM3. Their sparticle masses are listed in table 5.4. Those are from separated regions in the m_0-$m_{1/2}$-plane and are able to point out different signal properties.

Simulated was the resonant second generation slepton production with the yukawa coupling λ'_{211} including all possible decays. The event counts of events where a sneutrino or a smuon is the resonantly produced slepton is shown in figure 5.5(a). The channel with two muons in the final state is only one possibility of how the final state can look like. Others include neutrinos and thus $\not{E}_T$. Figure 5.5(b) shows the number of muons at tree level. It can be seen, that only a fraction of the generated events fulfil the dimuon requirement, so that the selection efficiency already is considerably affected. Naively one would await one fourth of the events to have two muons, if one assumes that the two muons can be replaced by neutrinos respectively with equal probabilities. The high mass points show that behaviour. In case of LM1 the situation is worse, which has its reason in a special characteristic of the sparticle mass hierarchy (cf. also table 5.4). There, in contrast to the smuon, the resonant sneutrino is lighter than $\tilde{\chi}_2^0$ and $\tilde{\chi}_1^\pm$. That means, that these particles can only be produced by an off-shell sneutrino which suppresses the cross section for that process. The dominant decay of the sneutrino is that into a neutrino and the lightest neutralino (compare also figure 5.7). Concerning the other signal points, smuon and sneutrino are on equal steps of the mass hierarchy leading to similar possibilities of decay.

Decays with more than two muons are realized if additional decays appear. For example if a sneutrino decays into a muon and a chargino, the chargino often decays into a neutralino under emission of a W-boson. Another possibility is, that a heavier $\tilde{\chi}_2^0$ is produced. This obviously tends to happen in higher regions of the parameter space at the points HM1 and HM3.

In case that less than two muons are produced, they are substituted by neutrinos leading to considerably large amounts of missing transverse energy. The search-signal does not provide this source for $\not{E}_T$, hence a requirement for low $\not{E}_T$ can be used to reject Standard Model Backgrounds with neutrinos like $t\bar{t}$. In this case, a cut value has to be found, that does not affect the signal too much. Figure 5.5(c) shows various $\not{E}_T$-distributions. The dots represent particle-flow-$\not{E}_T$ (RECO) without any further requirement. Especially the higher-mass signals show contributions in the higher $\not{E}_T$-regions. In case two muons on tree level are required, the distributions reduce to those given by the triangles. High $\not{E}_T$-values almost disappear and a tight cut $\not{E}_T < 50\,\text{GeV}$ can be used without removing much of the search-signal.

The following distributions are obtained by requiring two muons on tree level. The p_T-distributions of the leading and second leading muon (cf. fig. 5.5(e), 5.5(f)) show that the muons used in this search have rather low or medium momenta. To keep signal efficiency in all regions of the parameter space, the muon momenta should be as low as possible. How low that can be, is given by the trigger strategy. The p_T-cut should be chosen to be at least as high as the trigger thresholds. Better, they are slightly higher to avoid low efficiencies at the turn-on region. Hence the muon momenta are chosen to be $p_T > 20\,\text{GeV}$ for the leading-, and $p_T > 15\,\text{GeV}$ for the second leading muon.

A similar problem comes with the jet momenta. They also are quite low for some signal points and should be chosen to be as low as possible. This will be discussed later, when jets are introduced.

This analysis will take benefit of the lepton number violation the yukawa coupling provides, by requiring both muons to have same charges. Looking at figure 5.5(d) it can be seen, that about half of the di-muon events contain muons with equal charges. Thus, a cut on that property will remove about half of the signal, while the effect on the backgrounds is expected to be much more drastic.

As the gaugino mass as well as the slepton mass are reconstructible the most interesting distributions are the invariant di-jet-muon and di-jet-di-muon masses. HM3 shows an interesting behaviour when plotting them (fig. 5.6, black triangles). There are structures in the distributions that are not possible to be identified as sparticle masses. The reason is, that the resonant sleptons are even heavier than $\tilde{\chi}_2^0$ and $\tilde{\chi}_1^\pm$, which are then produced with relatively high frequency. When they decay, they produce an additional particle, mostly a W-boson that further decays into jets. If those jets are not included into the invariant mass calculation, the result is distorted. If on the other hand all jets are included, all sparticle masses can be reconstructed (green dots). The other signal points are not considerably affected by that operation and are not shown for reasons of clearness. The ability of heavy gaugino production also is the reason for the double structure in the distributions of the muon momenta of HM3 in figure 5.5(e). This is the reason that in mass reconstructions shown here all jets will be included and not only two.

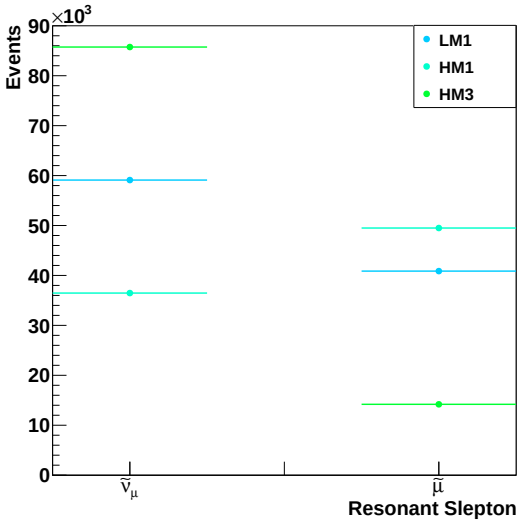

(a) Number of events, where the resonantly produced slepton was either a smuon or a sneutrino.

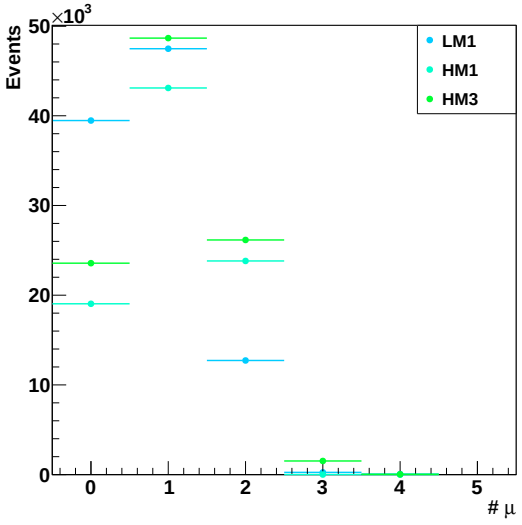

(b) Muon multiplicities at tree level.

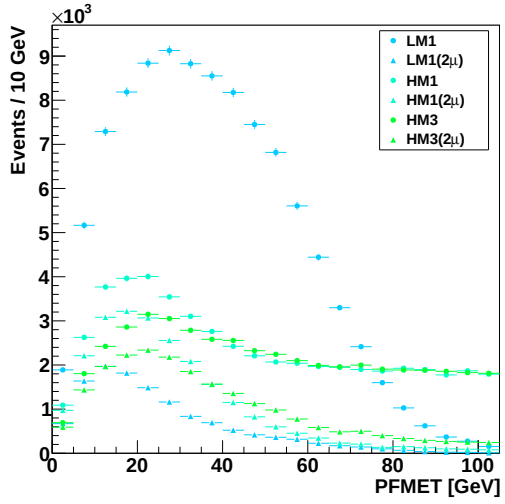

(c) PF-$\not{E}_T$-distributions. Without further requirements (dots) and when two muons are required on tree level (triangles).

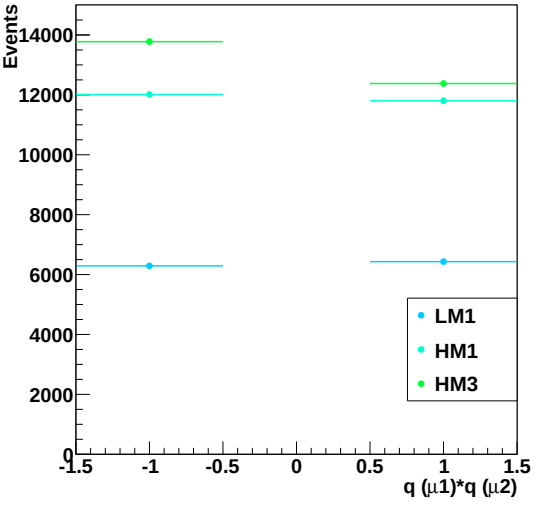

(d) Number of events with opposite- and same sign muon pairs. The product of the charges defines the type: $-1 = OS$, $1 = SS$.

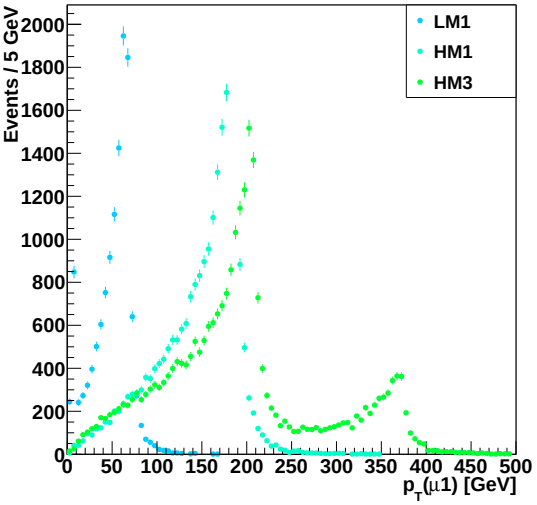

(e) Transverse momentum of the leading muon.

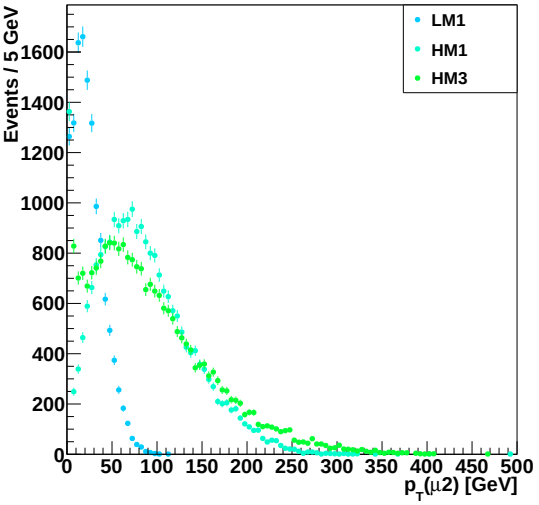

(f) Transverse momentum of the second leading muon.

Figure 5.5: Plots from the signal study obtained using generator information.

Sparticle	LM1	HM1	HM3
$\tilde{\mu}_L$	187	598	880
$\tilde{\nu}_{\mu L}$	167	588	874
$\tilde{\chi}_1^0$	97	359	339
$\tilde{\chi}_2^0$	178	677	640
$\tilde{\chi}_1^{\pm}$	178	678	641

Table 5.4: Sparticle masses of the three example signal points. Values in GeV.

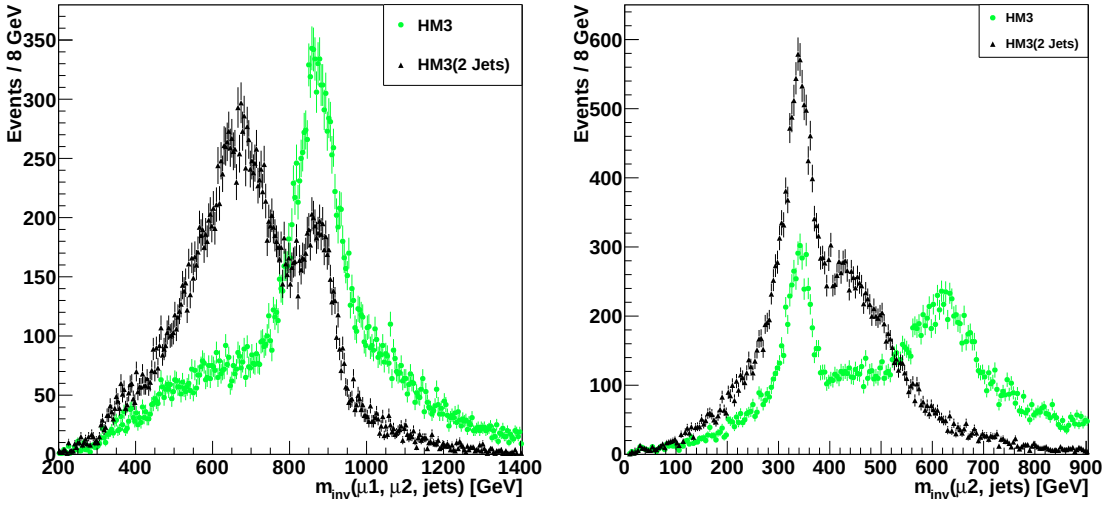

(a) Reconstructed smuon mass of benchmark point HM3.

(b) Reconstructed gaugino mass of benchmark point HM3.

Figure 5.6: Plots from the signal study obtained using generator informations and requiring two muons on tree level.

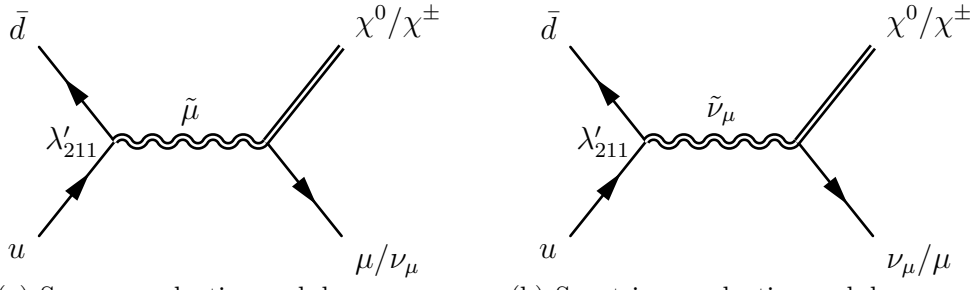

(a) Smuon production and decay.

(b) Sneutrino production and decay.

Figure 5.7

5.3 Object Selection

The physical objects that are recorded need to fulfil certain criteria. They are necessary to only select properly reconstructed objects in the analysis and reject fakes as well as possible in a first step. Fakes are reconstructed objects that are in fact of another type as the reconstruction provided. For example a pion that traverses the HCAL and enters the muon system could fake a muon.

The object identification (ID) criteria are presented in the following sections. They are studied, provided and recommended by the CMS physics objects groups (POG) and adopted for this analysis. The corresponding $N-1$ plots can be found in appendix B.

5.3.1 Muons

Muons that are usually not wanted in an analysis are those that come from non-prompt decays. Those can be produced by hadronic decays, for example in jets and need to be rejected. Another possibility is that a particle that is no muon is misidentified as one. That happens often in a so called punch through, where a hadron enters a muon chamber. The ID criteria for muons are called "Tight Muon" and used for muons with intermediate p_T [56]:

- The muon has to be reconstructed as a *global muon*. That means that its track is a combination of information from the tracker ("tracker track") and the muon system ("standalone muon track") using a Kalman-filter technique [29].
- $\chi^2/N_{dof} < 10$ for the global muon fit. This rejects effectively hadronic punch-through and decay in flight muons [57].
- At least one valid hit in the muon chamber has to be included into the global track fit. It has a similar effect as the cut before.
- Segments in at least two muon stations have to be hit. This cut avoids hadronic punch-through and gives consistency to the muon trigger.
- The impact parameter must fulfil $d_{xy} < 0.2\,\text{mm}$; it is measured with respect to the primary vertex. The task of this cut is to reduce cosmic muons. It is very unlikely that a cosmic muon passes in that short distance. Furthermore that cut reduces muons from decays in flight [57].
- The muon has to hit at least one pixel in the tracker.
- More than ten hits have to be measured in the whole silicon tracker.

5.3.2 Jets & Missing Transverse Energy

The jets used in this analysis were reconstructed using the anti k_T jet algorithm with $R < 0.5$ (*ak5*) and the particle flow algorithm (sec. 4.2.7). The latter is also used for calculating the missing transverse energy.

Certain criteria are recommended by the CMS JET/MET-POG for a better offline selection of jets ([58] and updates on [59]). Here, the "loose ID" was used:

- Constituents > 1: Number of particles the jet consists of.
- Neutral hadron fraction < 0.99 :Energy fraction deposited in the HCAL by neutral particles.
- Charged hadron fraction > 0: Energy fraction deposited in the HCAL by charged particles.
- Neutral EM fraction < 0.99: Energy fraction deposited in the ECAL by neutral particles.
- Charged EM fraction < 0.99: Energy fraction deposited in the ECAL by charged particles.
- Charged multiplicity > 0: Number of charged particles belonging to the jet.

5.3.3 Electrons

Electrons have a rather low importance on this analysis as they are just used for vetoing. Every event containing an electron that has $p_T > 15\,\text{GeV}$ and fulfils the ID criteria of the *Simple Cut Based Ele ID* using the working point *WP80* [60] is rejected. For conversion rejection the cuts are:

- No missing expected hit: From the measured track, it is possible to estimate the hits that it should have in the silicon tracker.
- Distance to a potential conversion partner [61]: Dist $> 0.02\,\text{cm}$
- Angle to a potential conversion partner [61]: $\Delta \cot\theta > 0.02$

Conversion means, that an initial photon produces an electron pair. Hence it is possible to search for the corresponding partner to reject such events.
Additional cuts in the barrel (endcap) -region are:

- The angle between supercluster and track: $\Delta\eta_{i\eta} < 0.004(0.007)$
- The angle between supercluster and track: $\Delta\phi_{i\eta} < 0.06(0.03)$
- Measure of the supercluster spread in η-direction in units of crystals: $\sigma_{i\eta i\eta} < 0.01(0.03)$
- Ratio of the energy deposits in HCAL over ECAL: $H/E < 0.04(0.025)$
- Combined relative isolation criterion: $\text{Iso}_{comb} < 0.07(0.06)$

Multiple calorimeter entries in η-direction originating from one electron are called a supercluster. They evolve from the bending of electron trajectories that radiate photons tangentially. Isolation is the sum of transverse momentum(energy) contributions in the tracker(calorimeters). It will be described in more detail later.

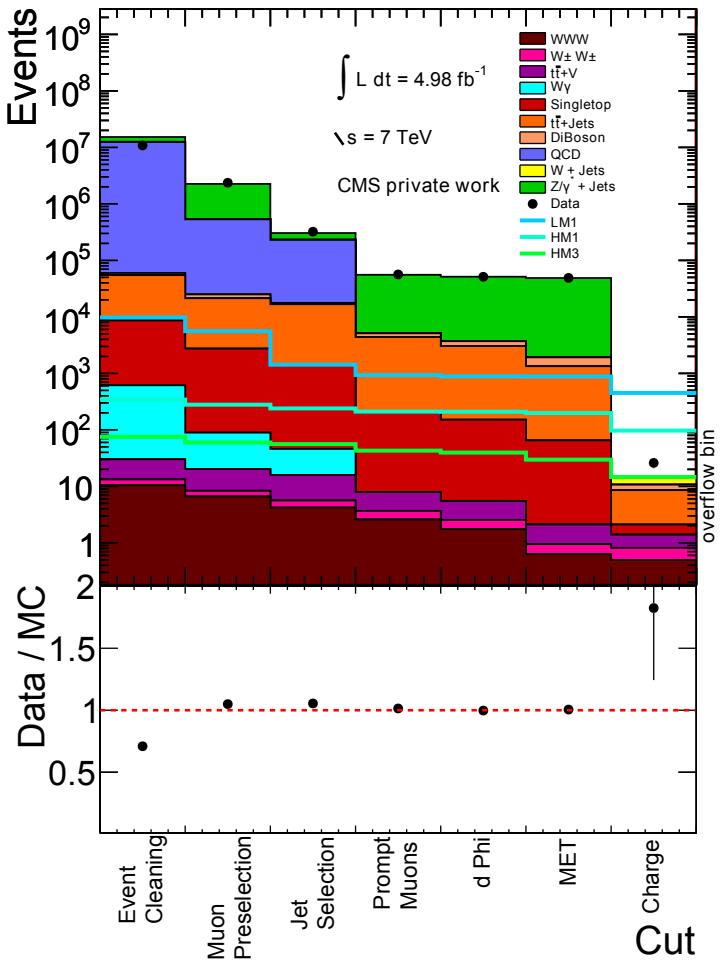

Figure 5.8: Analysis cutflow: The event count of data, background and signal are shown after each major cutstage.

5.4 Event Selection

To increase the ratio of signal to background, selections for events to be accepted are made. An overview of the single analysis steps is given by the so called cutflow, shown in figure 5.8. It shows the total number of events after each stage for all, data, background and signal. A stage is a point in the analysis, where one or several certain cuts are applied. Thus, the individual impact of the cuts can be observed.

5.4.1 Event Cleaning

At the first stage, some basic clean-up criteria are used. To pass, an event has to have at least one **properly reconstructed vertex**. To reduce **noisy cells** in the ECAL, that could fake a signal, single hot cells resulting in a spiky topology are vetoed. To do so, those with an energy entry of more than 3 GeV are searched. If the ratio of measured energy in the 3×3-matrix of cells surrounding the central one to the central one exceeds 0.9, the event is rejected.

At the same point, an **electron veto** is used. This means, every event containing an electron that fulfils the criteria of section 5.3 and $p_T > 15$ GeV is rejected.

It has to be mentioned, that at this point already some very basic selection cuts are applied, that are needed to reduce the amount of data that is stored locally. They are applied on data and background Monte-Carlo and require two muons with $p_T > 15\,\text{GeV}$ for the leading and $p_T > 7\,\text{GeV}$ for the second leading one. The muons do not have to fulfil any further ID criteria. In the same step, some additional recommended filters are used to improve the quality of the used samples.

Monte-Carlos that were produced by using Pythia6 for hadronisation, while the generation of matrix elements was done by external programs, passing the information with LHE-files, have a non-conservation of energy and momentum in some events. Those events need to be removed using the so-called TotalKinematicsFilter. This affects for example samples being produced with Madgraph or Powheg.

Additionally, the HBHE-noise filter is used. It is a recommended filter to reduce noise in the HCAL [62].

5.4.2 Muon Preselection

Before applying signal specific kinematic cuts, events containing the basic objects are selected. Hence in this stage, a loose muon selection is done. That means, that events are required, that need to have at least two muons fulfilling the muon ID criteria, whereas the leading muon must exceed $p_T > 20\,\text{GeV}$ and the second leading one $p_T > 15\,\text{GeV}$. These thresholds are chosen because of the choice of triggers as described in section 5.2. Later on, the constraints on the muons will be tightened and single muons will fail the selection. That is the reason why at this point at least two muons are chosen instead of exactly two.

5.4.3 Jets

In this stage, at least two jets are selected. As usual they need to fulfil the ID criteria. Additionally, every jet needs $p_T > 30\,\text{GeV}$.

The signal that is searched for provides two quarks that end up in two jets in most cases. Additional jets can occur due to initial or final state radiation and of course pileup effects. Hence it is beneficial to require leastwise two jets instead of exactly two. Requiring multiple jets is a powerful tool against the Drell-Yan background (compare figure 5.9, left).

The signal LM1 in this plot seems to contradict this argument, as it has its major contribution in the one-jet bin. The reason for that can be seen in the right plot of figure 5.9, that shows the p_T-distribution of the second leading jet. It illustrates, that the low mass benchmark point does not provide enough jets fulfilling the $p_T > 30\,\text{GeV}$ criterion. That also is the reason for the huge impact of that cut when regarding figure 5.8. As the LM1 expectation still is relatively large after all cuts, this loss is acceptable.

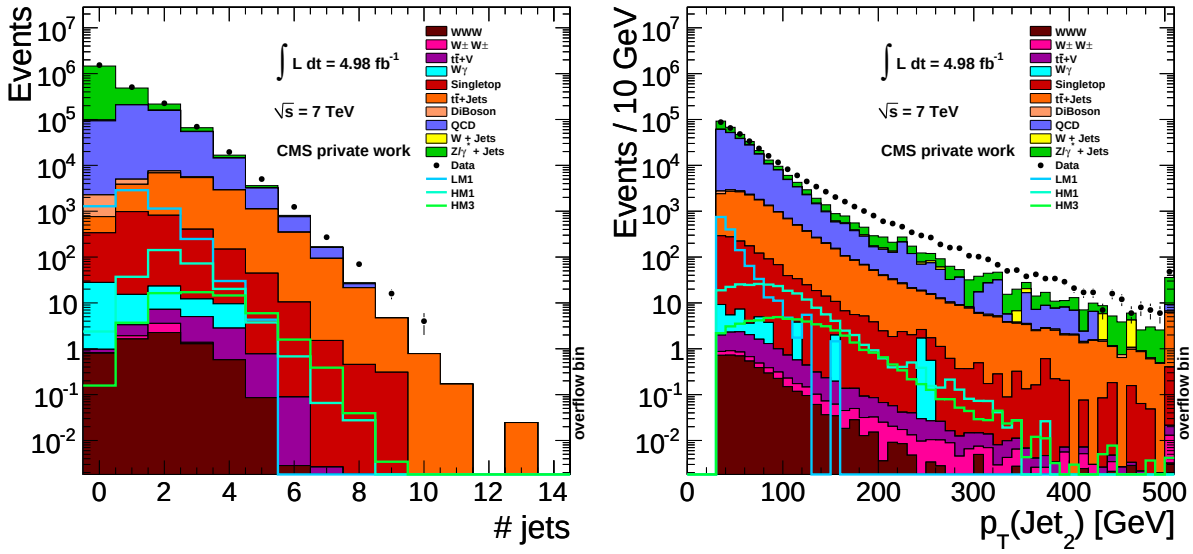

Figure 5.9: Left: Jet multiplicity before jet requirement; Right: p_T-distribution of the second leading jet.

5.4.4 Prompt Muon Selection

After selecting the basic objects in the events, further constraints on the event topology are done. This stage concentrates on muons again by requiring exactly two isolated muons that come from the same vertex. Again, the leading muon has to fulfil $p_T > 20\,\text{GeV}$ and the second $p_T > 15\,\text{GeV}$.

The muons of the signal are prompt ones that come directly from the location of the interaction. Non-prompt muons are those that are produced by decays in flight or hadronic decays inside jets. To avoid such effects, two countermeasures are taken. They are, that the muons have to be isolated and have to come from the same vertex.

Muon **isolation** can be measured in the tracker, the ECAL and the HCAL, respectively. In general, it is defined by summing up all transverse energies (transverse momenta in the tracker) that are deposited inside a cone of $R = 0.3$ around the muon track. The muon itself is excluded. Here, a variation is used that contains the previously defined isolations and that will be referred to as *semi-relative combined isolation*. It is defined as

$$Iso_{rel} = \frac{Iso_{trk} + Iso_{ECAL} + Iso_{HCAL}}{Min(p_T^{\mu}, 20\,\text{GeV})}. \tag{5.2}$$

Combined isolation means, that the single isolation contributions from the different detector parts are added. A relative isolation is one that is measured relative to the particle momentum. The reason to choose a relative isolation is to better reject muons that are being produced by decays inside jets. High energetic jets tend to have components with higher momenta, leading to an increased isolation value and muon momentum. Making the isolation semi-relative by using the Min-function in the denominator of equation 5.2 helps to avoid pileup dependencies of low energetic muons. Those tend to be swallowed by pileup pollution. Figure 5.10 shows the isolation of the leading muon. It can be seen, that most of the multijet background is removed when cutting at $Iso_{rel} = 0.15$.

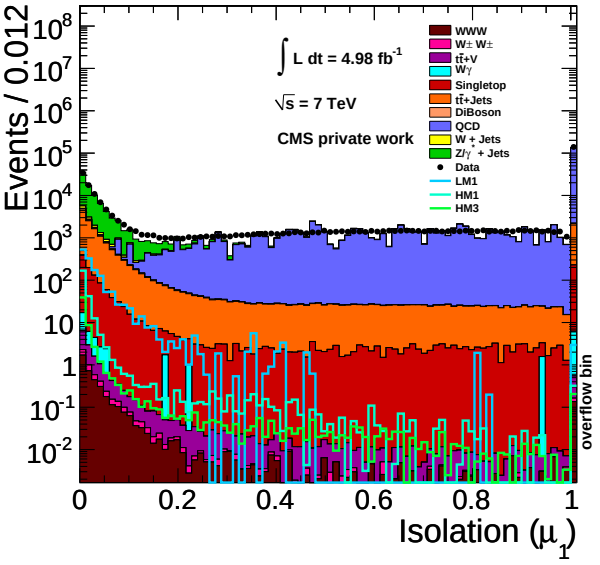

Figure 5.10: Semi-relative combined isolation of the leading muon.

Another way to avoid jet-induced muons is to require a spacial distance between muons and jets. Hence, both muons have to be separated by $\Delta R > 0.4$ from any jet. Figure 5.11(a) shows the corresponding distribution. It can be seen that in the region that is cut away, the distribution has an edge. The muons are required to fulfil the isolation criterion before this distribution is filled. Most muons that are close to a jet will not pass this condition that is why the distribution shows the strange behaviour.

The requirement, that both muons have to originate from the same vertex is not easily available and thus a makeshift has to be found. Here, a ΔZ requirement will be used. First, one has to get a feeling for the possible minimal distance that on the one hand can be distinguished by the tracker and on the other hand is typically found between two neighbouring vertices. Figure 5.11(b) shows in blue the distance ΔZ of every properly reconstructed vertex to its closest neighbour avoiding double-counting. It illustrates that only few vertices are closer than 0.1 cm. On the other hand, the muon ΔZ (in black, same plot) can be measured with much higher accuracy. Hence, a cut of $\Delta Z(\mu, \mu) < 0.08\,\text{cm}$ can be applied.

Furthermore it is required that both muons have triggered the event.

5.4.5 Invariant Dimuon-Mass & $\Delta\phi$

In the previous stage, exactly two high quality prompt muons were selected. Now, combined properties of both are used for further cutting.

The first cut affects the **invariant dimuon mass**. This cut is not motivated by physics but by a lack of Monte-Carlo. The Drell-Yan Monte-Carlo sample that is used, is only produced down to an invariant mass of $M(\mu, \mu) \geq 10\,\text{GeV}$ on generator level. To avoid a deficit of Monte-Carlo in that region, a general cut on the invariant mass is used. In order not to be affected by turn-on effects because of the detector resolution, the cut is

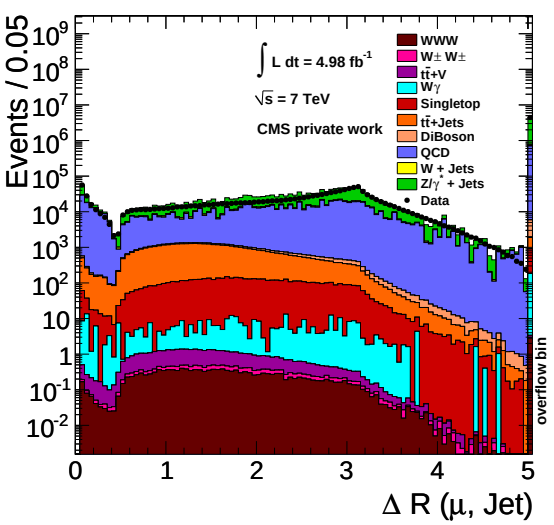

(a) ΔR between a muon and the next jet.

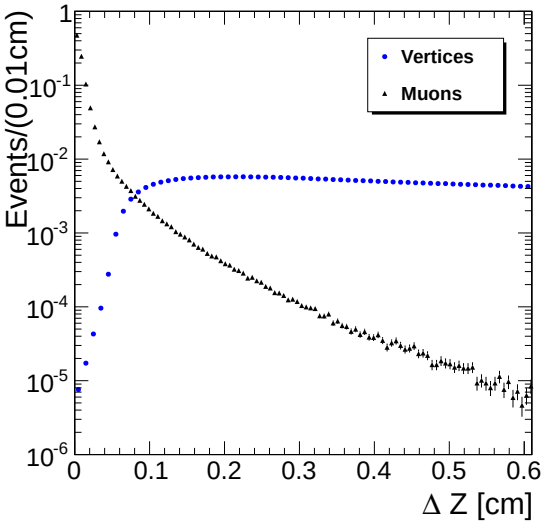

(b) ΔZ of each vertex to its next neighbour and between the two muons measured in data.

Figure 5.11: Prompt muon selections

chosen to be slightly higher than the generator cut, namely

$$M(\mu, \mu) > 15\,\text{GeV}. \tag{5.3}$$

Muon tracks can be measured very precisely. Thus it is favourable to use an **angular correlation** $\Delta\phi$ for further selection. Unfortunately, the second muon recoils against two jets, leaving the angle between the two muons a bad choice for a cut. The solution is to reconstruct the gaugino's four momentum using the momenta of the second muon and the jets. The comparison of both angles can be seen in figure 5.12(a). Including the jet momenta concentrates the signal at values of $\Delta\phi$ around π. The cut on the angle between the first muon and the gaugino candidate is chosen to be:

$$\Delta\phi(\mu_1, \chi) > 2\,\text{rad}. \tag{5.4}$$

At that value, the signal separates from the flat background shape. Figure 5.12(b) shows the distribution of $\Delta\phi$ before the cut. It allows discrimination of manly single top and $t\bar{t}$ backgrounds.

5.4.6 Missing Transverse Energy Rejection

In section 5.2 it was shown, that the channel that is used in this analysis does not provide sources for large amounts of MET. The cut was chosen to be

$$\not{E}_T < 50\,\text{GeV} \tag{5.5}$$

The distribution can be seen in figure 5.13(a).

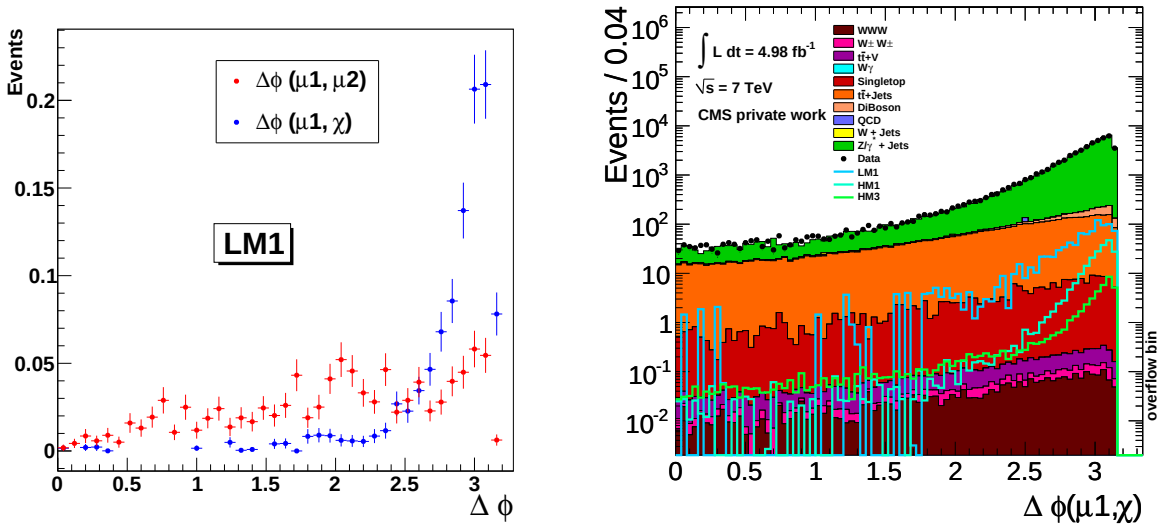

(a) Comparison of the angle between the two muons (red) and the one between the leading muon and the gaugino candidate calculated from the jets and the second muon (blue). Both distributions are scaled to the same area and obtained using the LM1 signal sample.

(b) Distribution of the angle between leading muon and gaugino candidate.

Figure 5.12: The $\Delta\phi$ variable

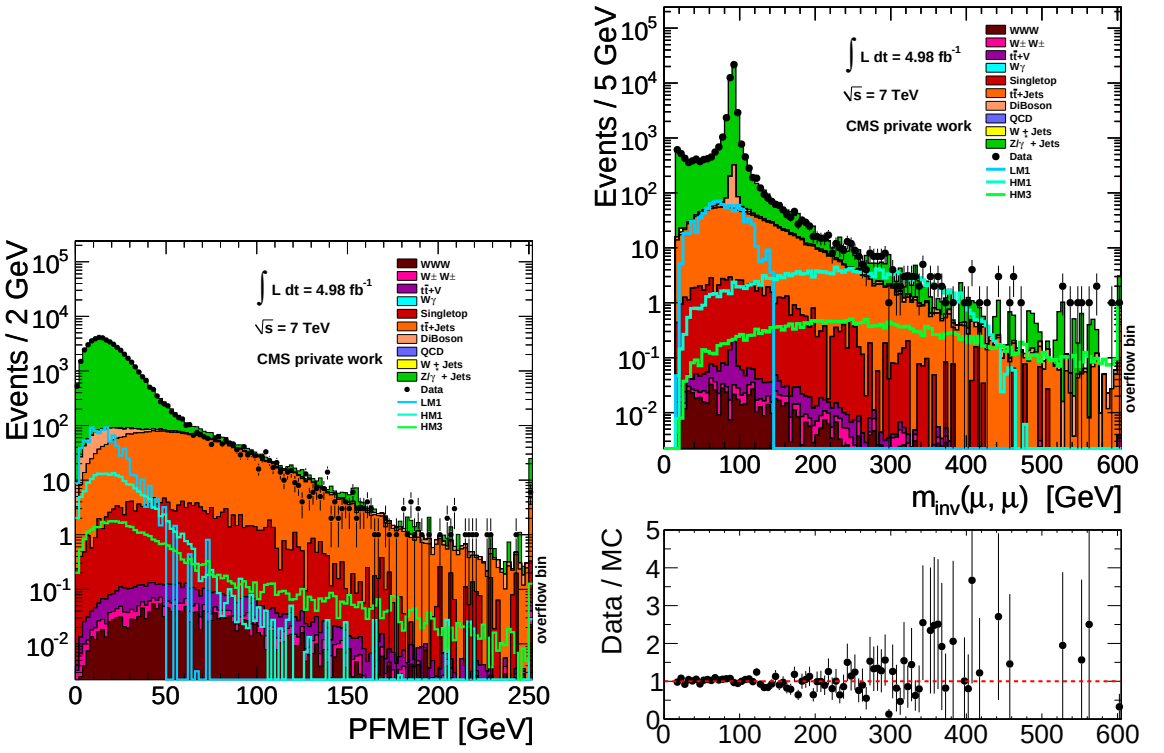

(a) The $\not{E}_T$-distribution

(b) The invariant di-muon mass before applying the same charge cut

Figure 5.13

5.4.7 Intermezzo

The next step in the chain of cuts would be the same charge requirement. This cut will drastically remove most standard model backgrounds, especially Drell-Yan, which is up to now the dominant background. Hence it is advisable to check for consistency at that point. For that reason figure 5.13(b) shows the distribution of the invariant mass of both muons. The Drell-Yan background was over-predicted and hence scaled down by a factor of 0.88. That was done by using the Z-peak as standard candle. The complete Drell-Yan sample was scaled, until it matched the Z-peak. This procedure is legitimate as the complete Drell-Yan background will be removed by the same-sign requirement and thus not enter the limit calculation. Furthermore, the factor is still smaller than the used NNLO k-factor. The scale factor as well as other corrections that will be described in section 5.6 are applied to all distributions if not mentioned otherwise. Overall, a good agreement can be found and at that point there is no hint for new physics.

5.4.8 Same Sign Muons

The final and most radical cut is the requirement, that both muons need to have equal charge signs. It reduces the Standard Model background by almost four orders of magnitude, removing Drell-Yan Monte-Carlo completely. Only about half of the signal is lost, thus the signal to background ratio is raised significantly. The overall event-count at this point is 26 for data and 14.28 for Standard Model background. The plots in figure 5.14 show the reconstructed masses of the gaugino (left) and the resonantly produced slepton (right).

An excess in data with respect to the background expectation can be observed. Its origin needs to be further investigated. The fact, that the excess is spanned over the whole range of the search distributions of figure 5.14 indicates, that the description of the Standard Model background is not sufficient, instead of a real discovery, that would concentrate the excess in a more narrow region. Hence, the following section describes a method to predict background expectations using a data driven method.

5.5 Data Driven Background Estimation

Two muons with the same charge sign are extremely rare in Standard Model processes. Thus it is highly probable that additional same sign events are caused by some kind of mismeasurement that is not properly simulated in Monte-Carlo. Those can be so-called "fake muons" and can have different origins. For example they can be non-prompt muons that are produced inside jets and are not rejected by the isolation criteria (comp. sec. 5.4.4). Another possibility is, that a muon is faked by another particle, e.g. a pion, that is not completely stopped in the HCAL or magnet and hence enters the muon system. The latter are "true fake muons". As both effects usually are treated in combination, they are both referred to as fakes. The influence of such fakes can be determined using data driven methods.

Another reason to estimate backgrounds from data is insufficient Monte-Carlo statistics. Processes with large cross sections are produced in such large amounts at the LHC, that

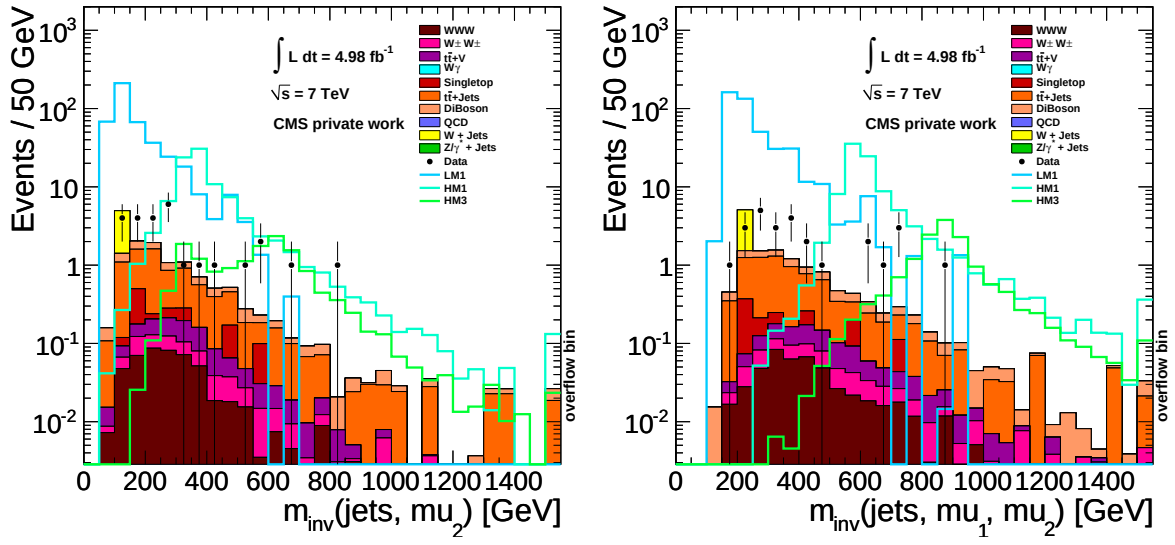

Figure 5.14: Distributions of the invariant masses of the second muon and all jets (left) and both muons and all jets (right) after all cuts. They represent the reconstructed masses of the gaugino from the slepton decay and that of the resonantly produced slepton itself.

it is not possible to generate enough Monte-Carlo events. The result is that the existing events have to be weighted using large factors (compare equation 5.1). The strongly affected backgrounds are the W+Jets and QCD-multijet samples. They have weighting factors up to several thousand (see table 5.2), so that in principle thousands of QCD events in the final distribution are possible but not simulated properly. Besides, the simulation of multijet events is quite complex and the results are usually not satisfactory.

The principle idea of a data driven background determination is, to measure the prediction of a certain background in a data sample that is independent from that the search is based on and then transfer the prediction into the latter. The method that will be performed in the following sections is able to make an estimation of QCD and W+Jets contributions that will then be used in the final result, as well as for other backgrounds like $t\bar{t}$ that will be used for consistency checks.

5.5.1 The Tight to Loose Ratio Method

The method is called *tight-to-loose ratio* (T/L) method or fake rate method [63]. It is used in various CMS analyses, for example in SUSY [64], Higgs [65] and heavy majorana neutrino [66] searches. The basic idea is to loosen an ID criterion of the muons - in this case the isolation - and measure the probability of such a *loose muon* to be one with the original requirement - a *tight muon*. This information can then be used to predict the number of fake tight muons in the search sample using a sample with loose muons.

A loose muon has all the ID criteria of the muons in the standard analysis. Only the isolation (eq. 5.2) is relaxed from $Iso_{rel} < 0.15$ to $Iso_{rel} < 0.4$. This implies, that every tight muon is also a loose one but not every loose muon also is a tight one. With that information, different subsamples of data are distinguished by sorting events by their number of tight and loose muons, see figure 5.15(a).

To measure T/L, those data-samples are used, that contain exactly one loose muon. The numbers of T/L are obtained by dividing the event counts of events with a tight by those with a loose, or with respect to the areas in figure 5.15(a)

$$T/L = \frac{t}{t+l}. \tag{5.6}$$

The next step is to predict the contribution of fake-events to the search sample the analysis is performed on, which is A in figure 5.15(a). An event of the last stage of the search can be faked in two different ways. If it is a double fake, both muons are fakes as it would happen with surviving QCD events. A single fake event has one prompt and one faked muon. This is the case for W background but also $t\bar{t}$. The prediction of fake events in the analysis sample is done using orthogonal samples that have two muons. Using the one with two loose but no tight muons (sample DF) predicts the number of double fakes, the one with one tight and one loose but not tight muon (sample SF) predicts the number of single fakes. To do the prediction, each of the events is weighted with the loose muon's probability to be a tight one. Using equation 5.6 the event weight is given by:

$$w = \frac{T/L}{1 - T/L} \tag{5.7}$$

The total number of double fakes is also the number of QCD contributions. It is calculated by:

$$N_{DF} = N_{QCD} = \sum_{2loose} w(\mu_1) \cdot w(\mu_2) = \sum_{2loose} \frac{T/L_1}{1 - T/L_1} \cdot \frac{T/L_2}{1 - T/L_2} \tag{5.8}$$

In this case, the assumption has to be made, that T/L for each of the muons is independent of that of the respective other one.

The same procedure is then applied to the single fake sample (SF), where every event is weighted with the probability corresponding to the loose muon:

$$N_{SF} = \sum_{1loose} w(\mu_{loose}) = \sum_{1loose} \frac{T/L}{1 - T/L} \tag{5.9}$$

This does not already correspond to the correct number of W+Jets events because the single fake sample contains contaminations from the double fakes sample, where one muon is faked. Applying the single fake weight to those events will lead to a double counting of QCD. Hence, the event count of the QCD prediction has to be subtracted from the single fake number to achieve the prediction of faking W+Jets events:

$$N_{W+Jets} = \sum_{1loose} \frac{T/L}{1 - T/L} - \sum_{2loose} \frac{T/L_1}{1 - T/L_1} \cdot \frac{T/L_2}{1 - T/L_2} \tag{5.10}$$

So far the principle. The next section will present the measurements to determine T/L and further measures that have to be taken. The results will be used to determine the background contributions of QCD and W+Jets.

5.5.2 Measurement & Background Prediction

The tight-to-loose ratio is measured depending on p_T and η of the loose muon. The result is shown in figure 5.15(b). It is quite high and increases with increasing muon p_T. The

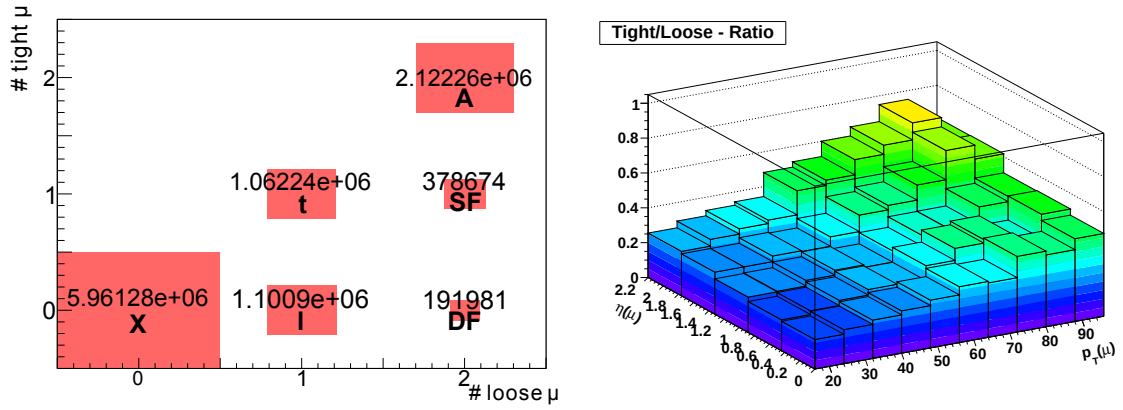

(a) The subsamples that are used for the T/L-method: It is measured using t and l. These samples contain exactly one loose muon. SF and DF are used for the prediction of fake contributions to the analysis sample A, all containing exactly two loose muons. X contains no muon and is not used.

(b) Measurement of T/L depending on muon p_T and η.

Figure 5.15

latter is not expected for non-prompt muons as they are bent less in the magnetic field with increasing energy and thus are more easily allocated to a jet. Figure 5.16(a) gives a hint what the reason for the increasing of T/L could be. It shows T/L in a one-dimensional projection, plotted for data and the same procedure performed on various Standard Model backgrounds. It can be seen that backgrounds that have a prompt muon result in a high T/L whereas QCD and thus events with non-prompt muons follow the expected behaviour of a decreasing T/L measurement. The conclusion is, that the samples that are used for the measurement of T/L are contaminated with processes that distort the measurement.

To reduce those contributions and only select QCD events that really contain faking muons, cuts are performed. The remaining contamination is then subtracted.The cuts are:

- At least two jets.
- $m_T(\mu, \not{E}_T) < 50\,\text{GeV}$ to suppress W.
- $80\,\text{GeV} < m_{inv}(\mu, \mu) < 100\,\text{GeV}$ against Drell-Yan, using any other muon that has not to fulfil any requirement.
- $\not{E}_T < 50\,\text{GeV}$ against W and $t\bar{t}$.

The N-1 plots corresponding to the cuts can be seen in figure 5.17. There are two arguments, why at least two jets have to be in an event to be chosen for the measurement of T/L. First of all, in the analysis a dijet requirement is used and single jet events could lead to a T/L-measurement that would not fit the conditions of the analysis. The second argument is given by the plots in figure 5.18 and confirms the first one. The left plot shows the p_T projected measurement of T/L for different jet multiplicities. It can be seen that for the case of one single jet, the result differs quite significantly. Hence, it will not be used for the measurement of T/L. The right plot shows the dependence of T/L on the

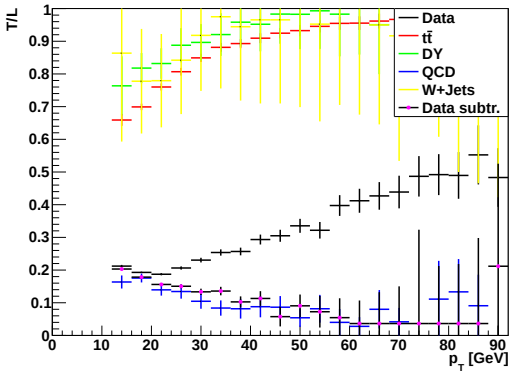

(a) T/L versus p_t for data and various Monte-Carlos, as well as the MC-subtracted data.

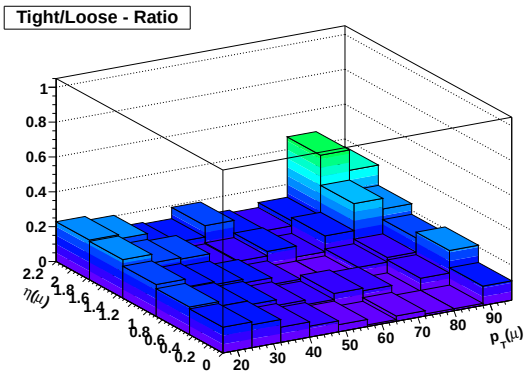

(b) T/L measurement after MC-subtraction. The large bins in the high p_T-η-regions are relics from low statistics in the used distributions.

Figure 5.16

angle ΔR between the jets as a function of the muon p_T in the case of exactly two jets. No significant dependence can be observed, hence it will not be considered furthermore.

After the cuts are applied, still remaining contributions of backgrounds with non-prompt muons are subtracted corresponding to their Monte-Carlo prediction. Thus, this estimation is not completely independent of simulation. Due to low statistics, especially in the high p_T and η regions, this procedure can lead to bins that have contents with negative values or (in principal) larger than one. Those are replaced by the mean of neighbouring bins. The resulting measurement of T/L can be seen in figure 5.16(b). In regions of high p_T and η the histogram shows an unsteady behaviour of bins fluctuating upwards. This has its reason in the low statistics. Thus, only values $p_T < 70\,\text{GeV}$ are used for the further procedure. If a muon momentum exceeds that value, the bin content of 70 GeV is used.

This statistical subtraction of the prompt muon backgrounds is also displayed in the projected histogram of figure 5.16(a) by the coloured data points ("Data subtr."). It can be seen that the Monte-Carlo subtracted data follow the distribution of the QCD Monte-Carlo as expected.

The histogram of figure 5.16(b) is the final T/L measurement that is used to estimate the fake contributions. Therefore the analysis is rerun twice. In a first run, the prediction of double fakes is estimated. That means, all ID criteria and analysis cuts are performed and only the muon isolation is relaxed to allow loose muons. All events containing two "loose but not tight" muons are weighted according to equation 5.7, where the muon p_T and -η dependent weighting factors are looked up in the histogram of figure 5.16(b). The resulting slepton mass distribution is shown in figure 5.19, left.

Similarly, the single fake contribution is determined. Events that contain one tight and one loose but not tight muon are weighted using the properties of the loose muon and the T/L-histogram. The prediction is shown in figure 5.19, right.

To estimate different components of the (single) fake measurement, the method is performed on Monte-Carlo too. As QCD and W+Jets background are about to be determined, they are thereby not considered. The only remaining backgrounds are $t\bar{t}$ and very

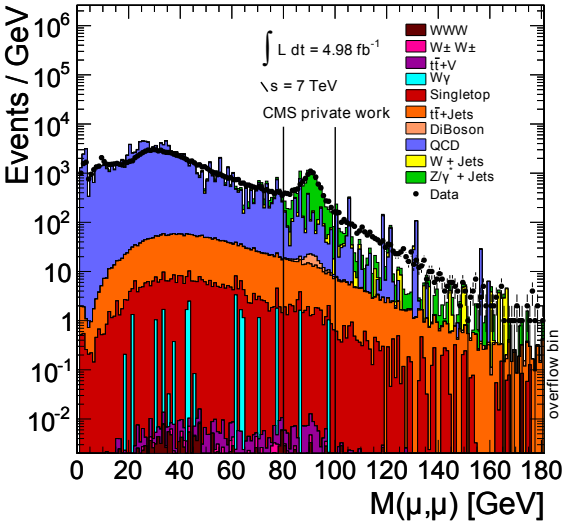

(a) $80\,\text{GeV} < m_{inv}(\mu,\mu) < 100\,\text{GeV}$: Z-veto

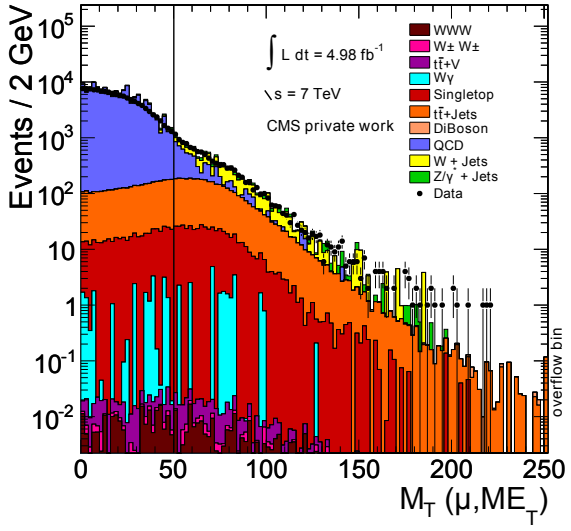

(b) $m_T(\mu, \not{E}_T) < 50\,\text{GeV}$: Against W+Jets, $t\bar{t}$ and single top contributions.

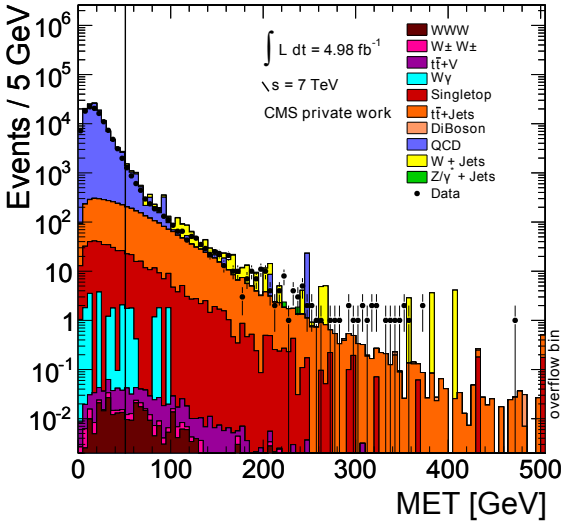

(c) $\not{E}_T < 50\,\text{GeV}$: To further reduce W+Jets and $t\bar{t}$ backgrounds.

Figure 5.17: Distributions corresponding to the cuts to reduce backgrounds that contaminate the T/L-measurement with prompt muons.

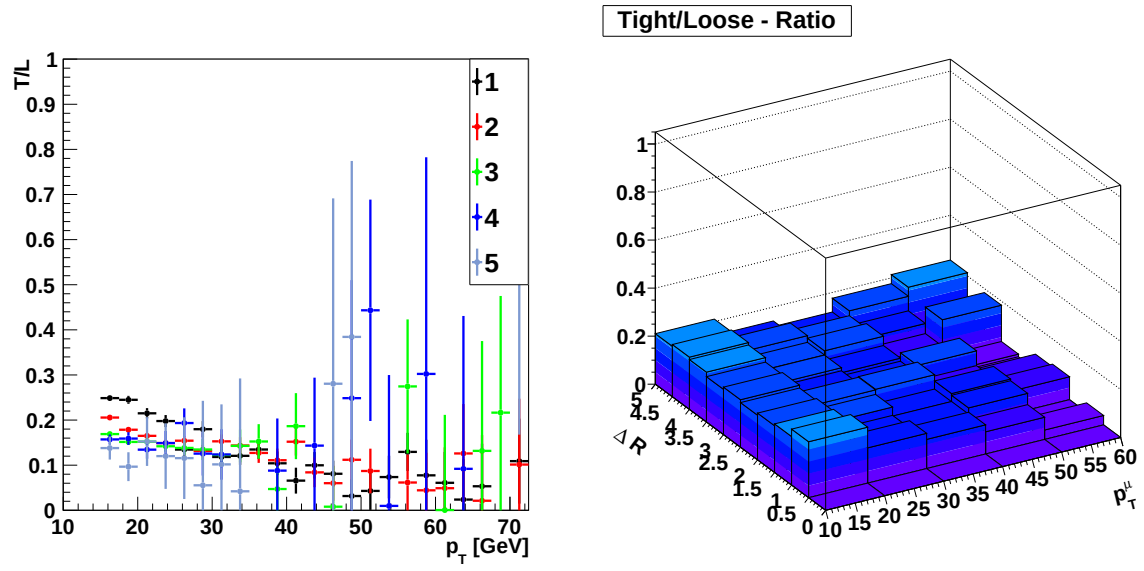

Figure 5.18: Dependence of T/L on the jet topology: Concerning the jet-multiplicity (left) and the angle between the jets in the two jet case (right).

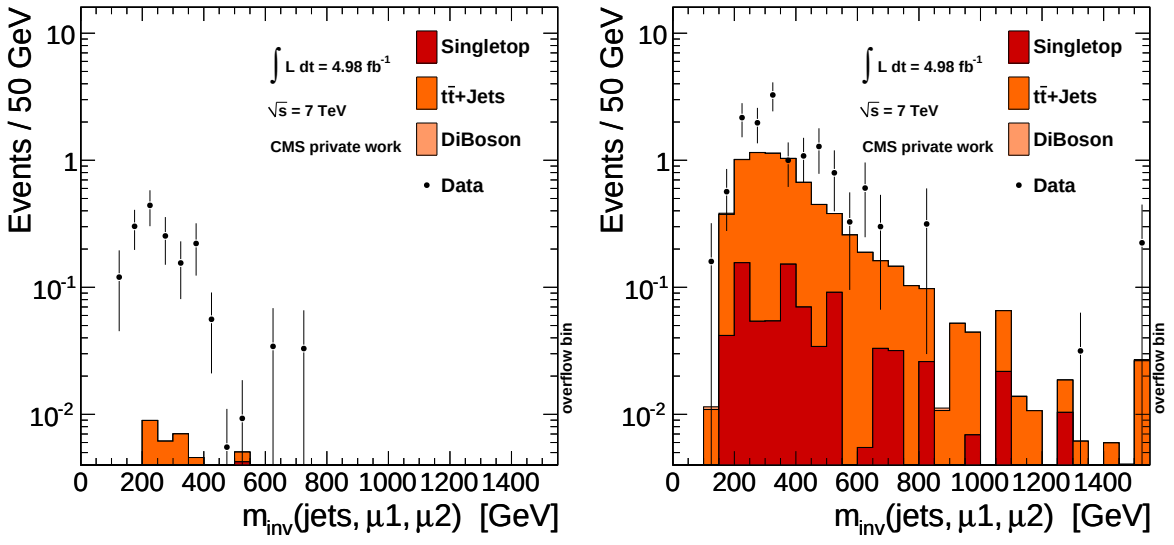

Figure 5.19: Predictions of the double- (left) and single fake contributions (right). When performed on data and Monte-Carlo.

few single top. Especially the measurement of the single fakes has large contributions from backgrounds like $t\bar{t}$. That will be used in the following section for cross-checks, but for the estimation of QCD and W backgrounds they have to be subtracted. The difference between the measurement in data and the contributions of Monte-Carlo are the searched estimations of QCD and W+Jets. Table 5.5 summarises the obtained results.

Sample	**double fakes**	**single fakes**
$t\bar{t}$+Jets	0.03	6.64
Other MC	0.01	0.86
Total MC	0.04	7.51
Data	1.63	14.09

Table 5.5: Results of the predictions based on the T/L method in data and Monte-Carlo.

Using these values, the individual predictions for W and QCD backgrounds can be achieved:

$$\begin{aligned} N_{QCD} &= N_{DF} = 1.63(Data) - 0.04(BG) = 1.59 \\ N_W &= N_{SF} - N_{DF} = \dots \\ \dots &= 14.09(Data) - 7.51(BG) - 1.59(QCD) = 4.99 \end{aligned} \tag{5.11}$$

5.5.3 Validation & Uncertainty

The predictions that are received with the tight-to-loose ratio method need to be verified. A usual approach is to compare the predictions from a data driven background estimation with those from Monte-Carlo. As in this case, only very few W- and no QCD Monte-Carlo events survive the analysis cuts, this does not lead to a reliable comparison.

The consistency check that is used here is based on the $t\bar{t}$ background. This background contributes to the final analysis selection by faking one muon and thus is also contained in the single-fake prediction. There, it cannot be separated from the W-prediction, thus there is no data-driven pure $t\bar{t}$-estimation to be compared to the Monte-Carlo prediction of the standard analysis. As a workaround, the T/L method performed on $t\bar{t}$ Monte-Carlo is compared with the standard analysis result. This can be seen in figure 5.20. It shows the reconstructed slepton (left) and gaugino (right) masses with the $t\bar{t}$ contribution from the standard analysis (orange area) and the prediction from the T/L method performed on $t\bar{t}$ Monte-Carlo (blue line). The shapes of both distributions agree well. The integral is 6.45 events from the analysis work flow and 6.79 from T/L, resulting in a difference of 5.3%. The good agreement gives confidence, that the T/L-method works well and provides a robust background estimation.

Finally, the method has to be tested for systematic influences. Therefore, the isolation requirement Iso_{rel} is varied between 0.3 and 0.5 to recalculate T/L and measure the influence on the QCD and W prediction. The resulting deviations are listed in table 5.6. Following these numbers, a total systematic uncertainty on the QCD and W+Jets prediction of 30% can be assigned.

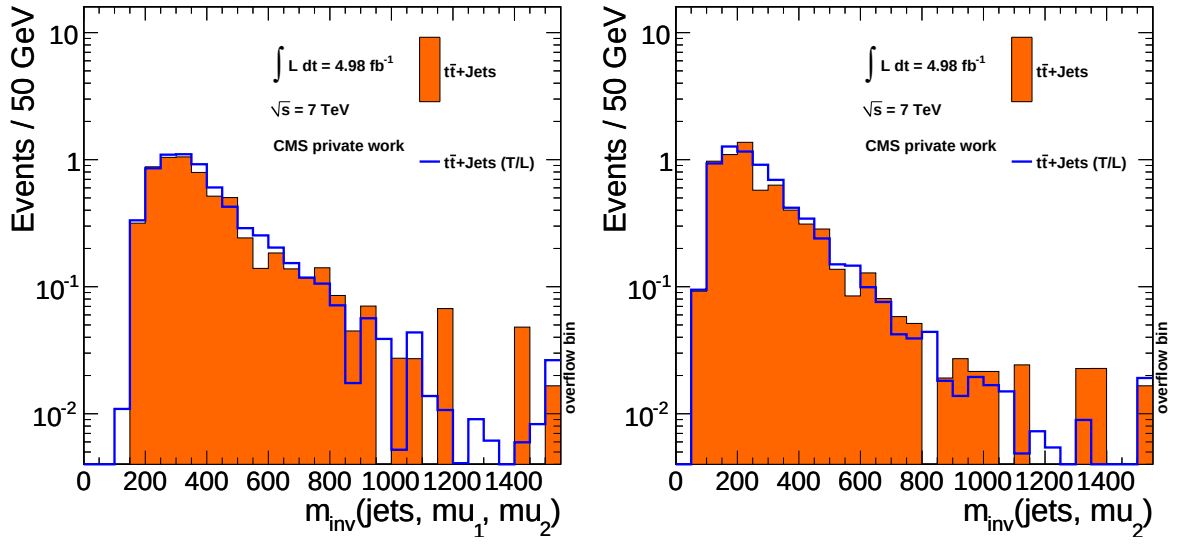

Figure 5.20: Closure test: The $t\bar{t}$ Monte-Carlo prediction from the analysis (orange area) and the T/L-method (blue line).

Variation	double fakes	single fakes	QCD [%]	W+Jets [%]
$Iso_{rel} = 0.3$	1.82	8.10	14.5	23.1
$Iso_{rel} = 0.5$	1.24	4.97	22.0	24.5

Table 5.6: Systematic influences on T/L-method results.

As a final plot of this method, it would be interesting to see the data driven background contributions with data, signal and Monte-Carlo backgrounds in one plot. Due to low statistics in some regions, the previously described background subtraction leads to negative entries in some bins. It is not possible to show that in a stacked histogram. That is why figure 5.21 shows the reconstructed invariant slepton and gaugino masses with the double-prompt backgrounds and the single fake contribution that contains QCD, $t\bar{t}$ and W-Jets and why the subtraction was performed on total event numbers and not on distributions.

5.6 Systematic Uncertainties & Corrections

5.6.1 Pileup

A huge effort of the 2011 data taking period and its future is the handling of the so called pileup. Pileup is the contamination of the event-content with contributions that are not from the interaction of interest. There are different contributions to pileup. The main influence comes from interactions of other protons in the same bunch crossing. Its amount strongly depends on the instantaneous luminosity which can be measured. Another contribution comes from the so called out-of-time pileup. This effect is caused

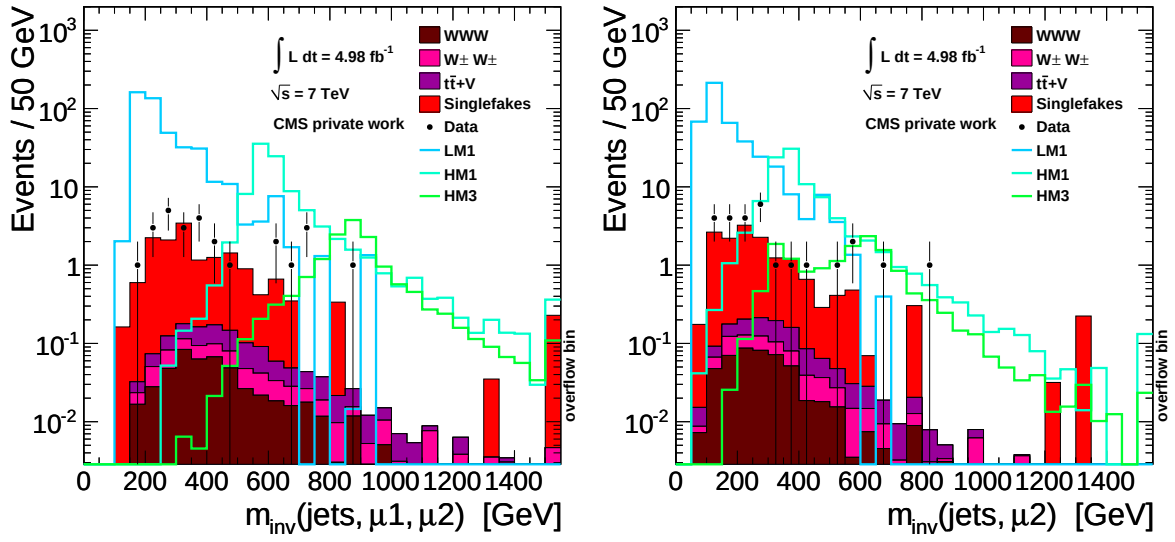

Figure 5.21: Reconstructed invariant slepton (left) and gaugino (right) mass with the single fake contribution of the T/L-method.

by remains of earlier crossings or contributions from already following ones and strongly depends on the bunch spacing and thus the frequency of collisions.

These effects have to be simulated in Monte-Carlo. When Monte-Carlo production was started, the actual influence of pileup contribution could only be estimated. Hence the simulation of pileup, which means the amount of added pileup events per event, follows a predefined distribution. For the *Fall11*-scenario, the distribution is shown in figure 5.22, red line. The information was taken from [67]. A corresponding distribution is estimated in data from the luminosity measurements. This is done by filling a histogram for each lumi section with a poisson distribution which has a mean of the expected number of pileup interactions estimated from the luminosity. The distribution is then weighted by the integrated luminosity and lifetime of that lumi section [68].

With these two pieces of information, it is possible to adjust the Monte-Carlo distribution to match that of the data by applying an event-by-event weight. The calculation of that event weight is done by a tool performing the so called 3D-reweighting [68]. Following this procedure, the weight is estimated considering all effects of in- and out-of-time pileup respectively. It uses the distribution of the number of pileup events that corresponds to the individual data used and calculates a $50 \times 50 \times 50$-matrix for all three pileup types. For each Monte-Carlo event, these three types are stored and the corresponding weight is looked up in the matrix.

The whole procedure should reweight the single event share, while the total event count should not be affected. To test this, the number of events is compared before and after reweighting without applying any other cuts as they might distort the result. Hence it is tested on a signal sample (LM1) as the background Monte-Carlo samples all have skimming cuts applied. The event count changes from 99969 to 100492, a difference corresponding to approximately 0.5%. This difference is acceptable.

The crucial distribution in an analysis with pileup dependencies is that of the number of reconstructed vertices. It is shown in figure 5.23 before the reweighting (left) and

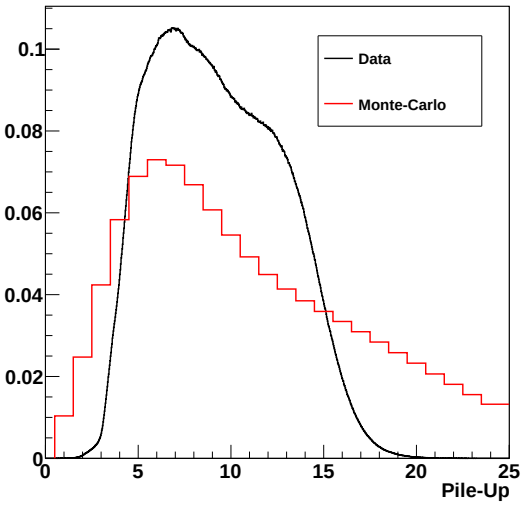

Figure 5.22: The number of contributing pileup events as used in Monte-Carlo generation and measured in data. Scaled to same areas.

after (right), after all cuts but the final same charge requirement have been applied. It can be seen that the data to Monte-Carlo agreement after the reweighting has improved significantly in comparison to the situation before.

Fur such a procedure, a systematic uncertainty has to be assigned. The dominant two sources are the uncertainties on the measurements of luminosity and total inelastic cross section. The recommendation how to estimate the systematic uncertainty on pileup is to redo the reweighting procedure and shift the number of interactions by ±5% [69]. The impact on the final event yield in the analysis is 2.5% in the background Monte-Carlos and about 1% for the signals.

5.6.2 Jet Energy Resolution

Figure 5.24, left, shows the $\not\!\!E_T$-distribution before applying the same charge- and $\not\!\!E_T$-cuts. Data and background prediction do not agree, a shift can be observed. An explanation for that effect is the jet energy resolution (JER). It was simulated to be better in Monte-Carlo than it is in fact in the measured data. This leads to a more narrow $\not\!\!E_T$-distribution as can be seen in the plot. The inaccuracy in the simulation can be corrected.

The JER-simulation is connected to the detector simulation step of the Monte-Carlo production chain (compare sec. 5.1). Thus one can get access to the resolution by comparing the properties of jets on generator level to those after the detector simulation, the RECO objects. This information can be used to apply an extra energy smearing to the jets using the following method.

The smearing is applied to every PFJets whose p_T exceeds 15 GeV. For each of those jets, generator jets (genjets) within a range of $\Delta R = \sqrt{\Delta\phi^2 + \Delta\eta^2} < 0.5$ are searched and their energy difference

$$\Delta E = E_{PFJet} - E_{GenJet} \tag{5.12}$$

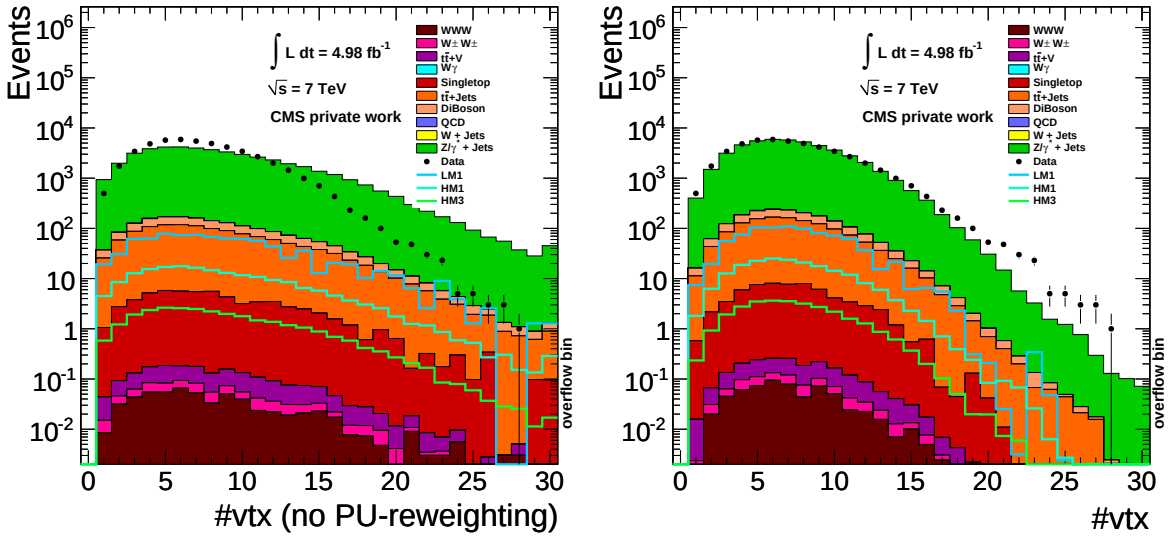

Figure 5.23: The multiplicity of reconstructed vertices before pileup reweighting (left) and after (right). All cuts but the same charge requirement are applied.

is computed. The GenJet resulting in the smallest ΔE is chosen for the further procedure. The energy of the PFJets is now modified by a fraction of ΔE:

$$E_{PFJet}^{new} = E_{PFJet}^{old} + f \cdot \Delta E \tag{5.13}$$

As ΔE is a measurement for the JER, this operation increases the resolution of the PFJets. This change has to be adopted to the momenta, that are changed by the same relative factor. In the same manner, the changes have to be propagated into $\not\!\!E_T$ applying them to the opposite direction respectively.

The factor f needs to be determined. In order to find an optimal value (f_0), it is varied between 0 and 0.3 in steps of 0.005. For each variation, the agreement of the $\not\!\!E_T$-distribution is determined using the χ^2-method. That means, the χ^2 for every bin in the distribution up to a certain value ${\not\!\!E_T}^{max}$ is calculated, summing all of them up. A parabola is fitted to the resulting χ^2-distribution, indicating the best value for f in its minimum. The result can be seen in figure 5.25(a). Table 5.7 shows the dependence of the result on ${\not\!\!E_T}^{max}$. In its first column, values for ${\not\!\!E_T}^{max}$ are shown. They are equal to the number of degrees of freedom. With increasing threshold, $\chi^2(f_0)$ increases as expected, but the ratio of $\chi^2(f_0)/N_{dof}$ improves. The corresponding optimized value f_0 is stable at 0.17 for not too small values of ${\not\!\!E_T}^{max}$. At values of $\not\!\!E_T > 200\,\text{GeV}$ the data- and Monte-Carlo statistic gets so low, that the calculation of χ^2 does not make sense.

${\not\!\!E_T}^{max}$ / GeV	$\chi^2(f_0)$	f_0
50	190	0.183
100	211	0.167
150	280	0.165
200	324	0.166

Table 5.7: Dependence on ${\not\!\!E_T}^{max}$

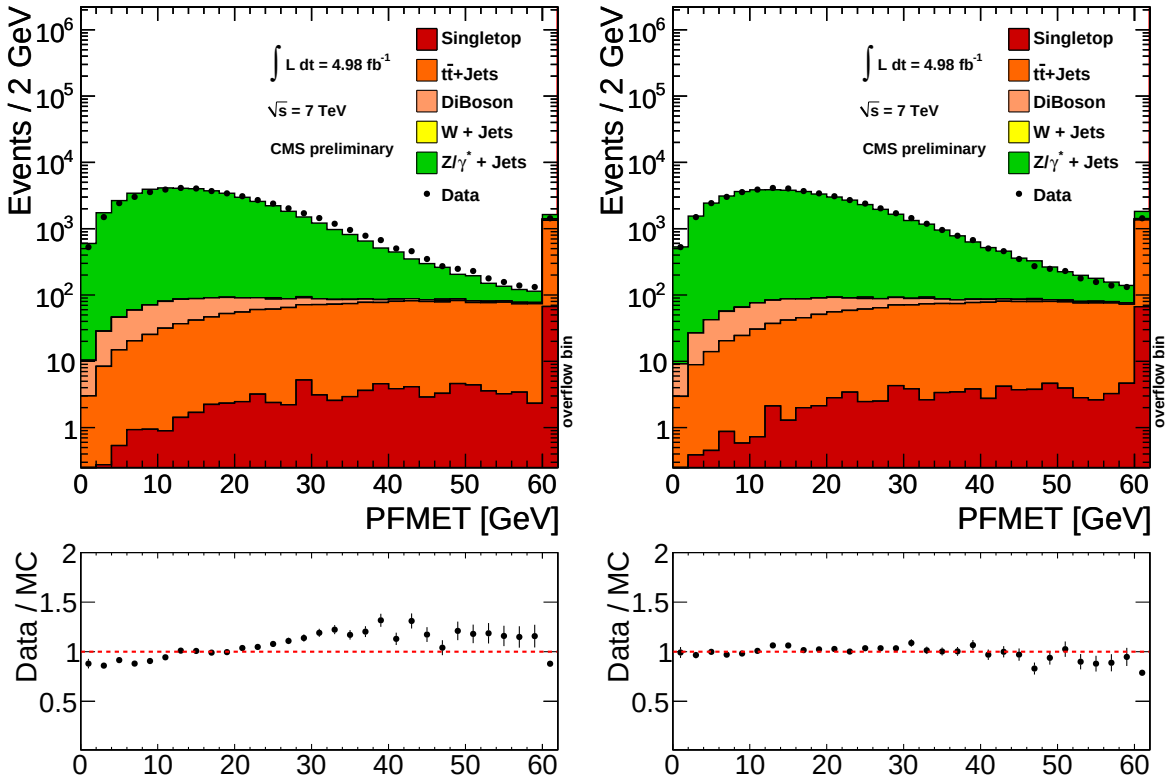

Figure 5.24: $\not\!\!E_T$-distributions before (left) and after (right) jet smearing.

The jet matching can of course only be done if a GenJet is found within $\Delta R < 0.5$. In case this does not happen, a solution has to be found how to smear those PFJets. Otherwise, the method would be sensitive to pileup (-jets) that cannot be matched but also have a wrong resolution in the simulation. For that reason, the ΔE of jet pairs that could be matched are plotted, as shown in figure 5.25(b) with black dots. This distribution is normalized to an area equal to one and a Breit-Wigner function is fitted (black line). Choosing this kind of function is the result from trying various functions, for example a Gaussian. Although the agreement is not perfect, especially in the outer regions, the result is quite satisfactory. In the analysis, the information of that fit is used to generate a random ΔE in case no matching GenJet is found. The red dots in the plot represent those jets.

The main source for a systematic uncertainty on this method is, that a PFJet is matched to a GenJet, that it not originally belongs to. This will most probably happen, when multiple GenJets are located in a narrow region. To estimate that effect, the method is modified for the case, that multiple GenJets lie inside the cone. In additional iterations of the method, always the GenJet with the highest energy ($f_0 = 0.1661$), the lowest energy ($f_0 = 0.1629$) and the sum of all jet energies ($f_0 = 0.1575$) is used to calculate ΔE. In this way, the most extreme variations are considered and the resulting systematic uncertainty should be a conservative estimation.

With the optimization procedure described above and the estimation of systematic influences, the smearing factor is assumed to be

$$f = 0.166 \pm 0.010. \tag{5.14}$$

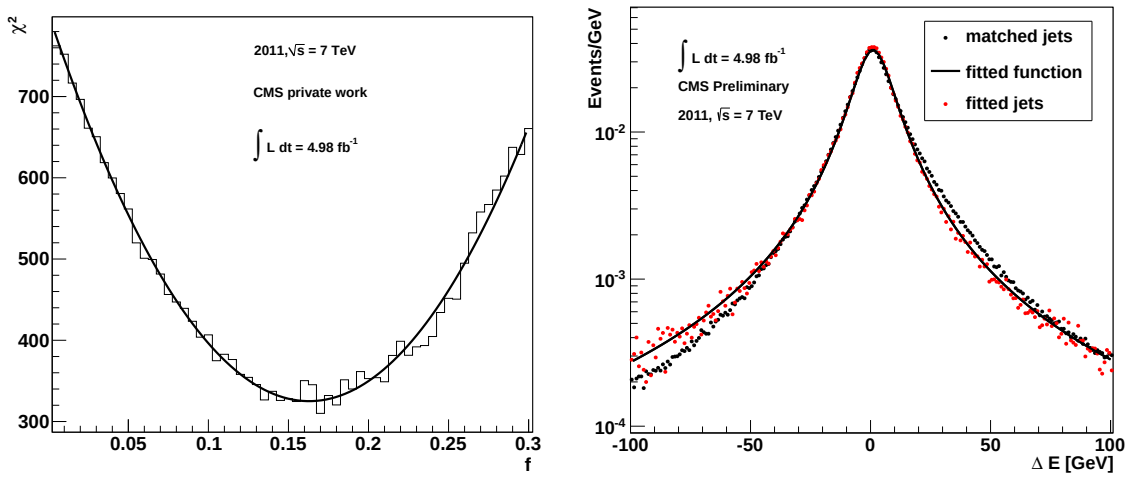

(a) χ^2-distribution depending on the f-variation with parabola fit.

(b) The ΔE of matched jet pairs (black dots) and a Breit-Wigner fit.

Figure 5.25

The impact on the final event yield is found to be 0.5% in the background- and 1% in the signal samples.

5.6.3 PDF & α_s-Uncertainties

PDF is an acronym for *parton distribution function*. PDFs describe the quark and gluon content of hadrons. As the LHC collisions are performed with interacting protons, it is mandatory to know their structure as precise as possible to create reliable Monte-Carlo events and predict cross-sections. The cross section for hadronic interactions is given by

$$\sigma = \sum_{i,j} \int_0^1 \int_0^1 \mathrm{d}x_1 \mathrm{d}x_2 \cdot f_i(x_1, Q^2) f_j(x_2, Q^2) \cdot \sigma_{ij}, \tag{5.15}$$

where i and j are possible initial state partons with the cross section σ_{ij} at the given center of mass energy. 1 and 2 denote the interacting partons. The functions f are the probability to find a parton with momentum fraction x at energy scale Q^2. These probabilities are given by PDFs. Figure 5.26 shows the results obtained by the MSTW-group with the PDF-fits of different partons depending on their momentum fraction x.

It is not possible to find a theoretical solution for PDFs. Thus they have to be obtained from experimental measurements of structure functions. This measurements were performed by different groups using different experiments. Those, that will be used here are from fixed-target or collider experiments examining electroproduction from deep-inelastic electron, muon and neutrino scattering or hadroproduction with Drell-Yan and jet production. The modelling of PDFs is then done by fitting a function to the measurements. There are two approaches how to fit the function and determine uncertainties. Following a *Hessian* approach, the functions are fitted by minimizing a log-likelihood χ^2-function. A *Monte-Carlo* approach generates replica of pseudo data containing exactly the same number of data points as the measurement. They are produced in a way, that the mean over corresponding points from all replicas results in the measurement [71].

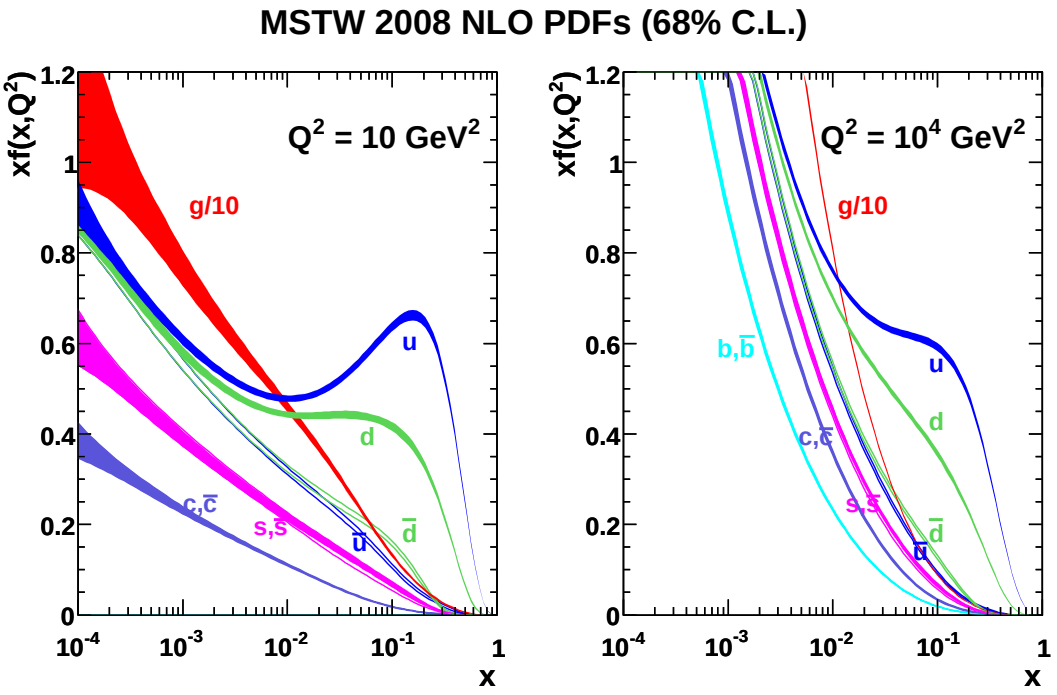

Figure 5.26: The PDF fit results depending on different partons with momentum fraction x as provided by MSTW2008. The coloured bands are the 1σ-confidence intervals. Results for an energy scale of 10GeV^2 (left) and 10^4GeV^2 [70].

The PDF4LHC-group [72] provides explicit recommendations of PDF sets from which groups should be used for LHC data [73], as well as a detailed recipe how to proceed with them [74]. They will be used to estimate the impact of PDF and α_s-uncertainties on the analysis. The recommended PDF sets with the Hessian approach are CT10 [75] and MSTW2008 [70][76]. The Monte-Carlo approach is used by NNPDF2.1 [77][78].

The most important theoretical uncertainty that influences the global fit of PDFs is the strong coupling constant α_s. Consequently it is common to handle these uncertainties simultaneously. Hence, α_s-uncertainties are computed using a fixed value for the PDF and vice versa. Both single uncertainties are then combined by adding in quadrature [71]:

$$\Delta X = \sqrt{\Delta X^2_{PDF} + \Delta X^2_{\alpha_s}} \tag{5.16}$$

The different groups have different values for $\alpha_s(m_Z)$. It is 0.118 for CT10, 0.119 for NNPDF2.1 and 0.120 for MSTW2008. The generalized 1σ-uncertainty is $\Delta\alpha_s = 0.0012$.

The Monte-Carlo samples used in this analysis have been produced using the *Pythia Tune Z2*. The tune describes the modelling of the underlying event (UE) and therefore also uses a PDF description. In case of Z2, the PDF set CTEQ6l1 [79] is used [80]. To be able to evaluate the uncertainties of other PDF sets one would either have to reproduce all Monte-Carlos applying the other PDFs, a procedure that is very impractical, or it is possible to reweight the existing samples. In the latter case, each background is examined for its content of the hard interaction and an event-by-event weight is applied to remodel the new PDF conditions. For this method, a tool provided by the LHAPDF-group is used [81].

The PDF sets contain different subsets, so called *members*. Usually, one member represents the best fit, the others model the uncertainties of the PDFs and α_s. The reweighting is done for all of these members. Applying the event weights and using the usual analysis cuts has an influence on the final event yield. Thus, the analysis is performed for every member and the overall uncertainty is obtained using the different final event numbers.

The PDF sets using the Hessian approach have one sample with members to estimate the PDF uncertainty and others for the α_s uncertainty determination. Assuming the members to be orthogonal, the PDF errors are determined using the formulas

$$\sigma(PDF,+) = \frac{1}{C_{90}}\sqrt{\sum_{i=1}^{N/2}\left(max\left[\mathcal{O}(2i-1)-\mathcal{O}(0),\mathcal{O}(2i)-\mathcal{O}(0),0\right]\right)^2} \tag{5.17}$$

$$\sigma(PDF,-) = \frac{1}{C_{90}}\sqrt{\sum_{i=1}^{N/2}\left(max\left[\mathcal{O}(0)-\mathcal{O}(2i-1),\mathcal{O}(0)-\mathcal{O}(2i),0\right]\right)^2}. \tag{5.18}$$

The number of members is $N = 53$ for CT10 and $N = 41$ for MSTW2008. $\mathcal{O}(i)$ denotes the observable, the final event yield, for member i. The best fit corresponds to $i = 0$. The factor $C_{90} = 1.64485$ is only used for CT10 whose uncertainty represents a 90% C.L. interval that needs to be adjusted to a 68% C.L. interval with that factor.

The error on α_s is obtained separately. In the case of CT10, members are provided that have the best fit and $\alpha_s = 0.118 \pm 0.001$. Using those the error is acquired by

$$\sigma^{CT10}(\alpha_s,\pm) = \frac{1}{C_{59}}\left(\mathcal{O}_{\alpha_s}(\pm)-\mathcal{O}(0)\right) \tag{5.19}$$

with $C_{59} = 5/6$ to adjust for the different value of $\Delta\alpha_s$ (0.001/0.0012).

The procedure is similar for MSTW2008, only there is a different scaling factor for the up- and down variation respectively ($C_{79} = 5/4$)

$$\sigma^{MSTW}(\alpha_s,+) = \left(\mathcal{O}_{\alpha_s}(+m)-\mathcal{O}(0)\right) \qquad \sigma^{MSTW}(\alpha_s,-) = \frac{1}{C_{79}}\left(\mathcal{O}_{\alpha_s}(-)-\mathcal{O}(0)\right) \tag{5.20}$$

The combined PDF- and α_s-error is then calculated as descried in equation 5.16 by adding them in quadrature, for both, CT10 and MSTW2008 respectively.

The procedure differs for the PDF set NNDPF2.1 using the Monte-Carlo approach. It has samples with varied α_s values, each containing 100 PDF-replicas. Assuming the α_s-uncertainty to be gaussian around the mean value of $\alpha_s^0 = \alpha_s(m_Z) = 0.119$, an equivalent number of replicas has to be chosen from the corresponding samples to enter the uncertainty calculation:

$$N_{rep}^{\alpha_s(j)} \propto \exp\left(-\frac{\left(\alpha_s(j)-\alpha_s^0\right)^2}{2\left(\Delta\alpha_s\right)}\right) \tag{5.21}$$

For the best statistic, the number of replicas at the central value is $N_{rep}^{\alpha_s(0)} = 100$. With that, the combined uncertainty can be calculated with

$$\sigma^{NNPDF}(\alpha_s+PDF) = \sqrt{\frac{1}{N_{rep}-1}\sum_{j=1}^{N_\alpha}\sum_{k_j=1}^{N_{rep}^{\alpha_s(j)}}\left(\mathcal{O}\left(PDF(k_j,j),\alpha_s(j)\right)-\mathcal{O}_0\right)^2}. \tag{5.22}$$

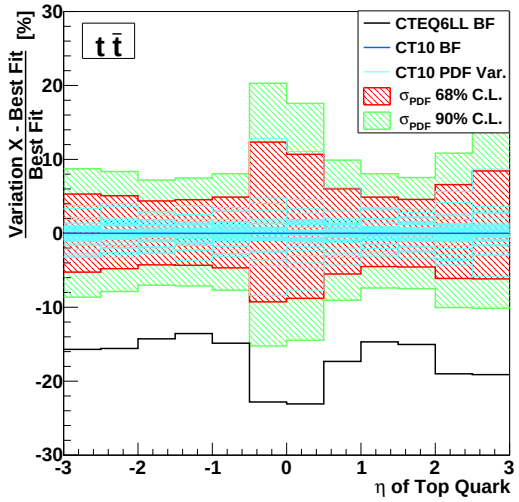

(a) Relative PDF variations. The black line represents the PDF the Monte-Carlo originally was produced with.

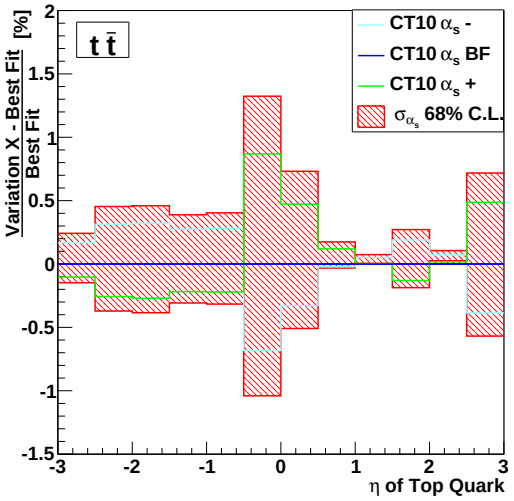

(b) Relative variation of α_s.

Figure 5.27: Uncertainties obtained from CT10 as a function of the pseudorapidity of the top quark. Shows the variation of member X in light blue and the obtained $1-$ and 2σ error bands.

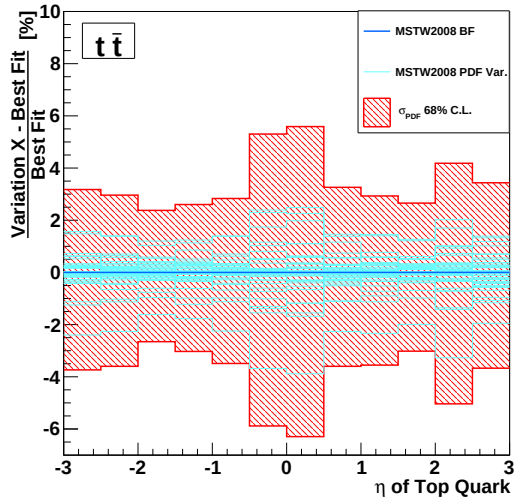

(a) Relative PDF variations.

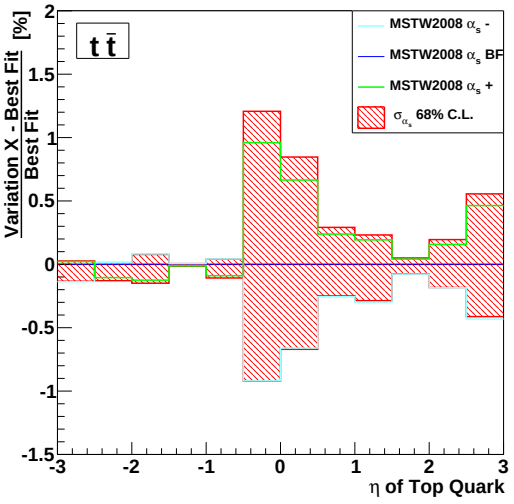

(b) Relative variation of α_s.

Figure 5.28: Uncertainties obtained from MSTW2008 as a function of the pseudorapidity of the top quark. Shows the variation of member X in light blue and the obtained 1σ error bands.

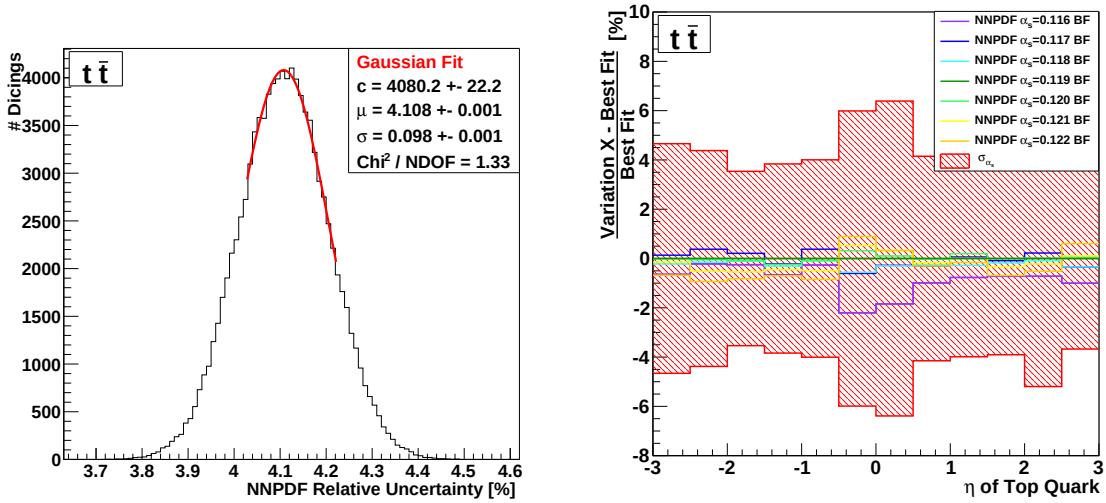

(a) The combined PDF and α_s uncertainty when choosing randomly the number of used replicas. The red line is a fitted Gaussian to obtain the final value, here $\sigma(PDF, \alpha_s = 4.1)$.

(b) Combined relative PDF and α_s uncertainties as a function of the pseudorapidity of the top quark. It shows the variation of different members with respect to the best fit $\alpha_s = 0.119$ in green and the 1σ error band.

Figure 5.29: Distributions corresponding to NNPDF2.1.

The number of samples and thus the number of values for α_s is $N_\alpha = 7$. For the samples, from which only a fraction of all replicas is used, a method has to be found how to decide which ones are taken. One possibility is to take all replicas and apply a weighted mean. Another way is to randomly choose the right number repeatedly, histogram the result each time and find a mean value by fitting a gaussian function. Both methods are used, whereas for the random part, 100000 dicings are performed.

As the $t\bar{t}$ Monte Carlo has the highest statistics of the remaining samples, it is chosen to present the obtained results of the described procedure as shown in figures 5.27-5.29. Still the statistics is quite low, which results in not smooth distributions.

The distributions show the uncertainties relative to the best fits, either for the PDF and α_s uncertainties separately, or both together in case of NNPDF in figure 5.29. Relative means, that the difference of member X to the best fit member is calculated. The resulting total PDF and α_s uncertainties are shown by the red error bands.

Looking at the red error bands, the α_s uncertainties of CT10 and MSTW2008 have comparable shapes, which also can be observed in the corresponding PDF uncertainty distributions. Nevertheless, the absolute values are slightly different in both cases. The shape and values of the combined PDF and α_s uncertainties of NNPDF are comparable to the PDF values of the other sets, what is expected as the α_s contribution seems to be rather small compared to that of the PDFs.

Figure 5.29(a) shows the combined PDF and α_s uncertainties of NNPDF2.1 when the random choice of the used replicas is made repeatedly. A Gaussian can be observed with the mean $\sigma(PDF, \alpha_s) = 4.1\%$.

Table 5.8 sums up some exemplary results of the major backgrounds and signals. The complete list can be found in the appendix (table C.1). It can be seen that the dominating

contribution comes from the PDF uncertainty while the α_s-uncertainties are rather small. As can be seen in the last two columns, both methods to calculate the uncertainties for NNPDF lead to same results. The combined errors on the event yield are in ranges of $3-6\%$ and differ whith respect to those of other sets in the same Monte-Carlo sample. Especially the PDF-uncertainties are partially asymmetric. Some signal samples show remarkable higher values (LM7, LM10, LM12). Those lie in regions of high m_0-values, that are not reached by the search grid. Hence the lower values of the remaining benchmark points are trusted and a pessimistic combined PDF and α_s-uncertainty of 6% is applied to all signal Monte-Carlos. In the paper [82], an uncertainty of 5% is mentioned, that is compatible with the results gained here.

Concerning the background Monte-Carlos, for each sample, the most deviating value of the up- and downward uncertainty is chosen from the three PDF-sets. From those two, the mean is calculated and taken as symmetric uncertainty on each background sample individually.

	CTEQ10			MSTW2008			NNPDF	
[%]	PDF	α_s	combined	PDF	α_s	combined	weighted mean	random replicas
$W \to l\nu$	+ 4.2 - 4.5	+ -0.4 - 0.4	+ 4.2 - 4.5	+ 4.1 - 3.3	+ -0.3 - -0.3	+ 4.1 - 3.3	3.9	3.9
$t\bar{t}$	+ 5.5 - 5.1	+0.0 - 0.1	+5.5 - 5.1	+3.2 - 3.7	+0.2 - 0.2	+3.2 - 3.7	4.1	4.1
$LM1$	+ 3.0 - 4.1	+0.0 - -0.1	+3.0 - 4.1	+2.5 - 2.1	+0.2 - 0.2	+2.5 - 2.1	2.8	2.8
$HM1$	+ 3.5 - 5.1	+-0.6 - 0.6	+3.6 - 5.2	+2.9 - 2.4	+-0.4 - -0.4	+3.0 - 2.4	3.3	3.3
$HM3$	+ 4.4 - 6.1	+-0.8 - 0.8	+4.5 - 6.1	+3.4 - 2.6	+-0.7 - -0.7	+3.5 - 2.6	4.1	4.1

Table 5.8: The results of the PDF and α_s-error estimation for $W + Jets$ and $t\bar{t}$ and three signals. The complete list can be found in the appendix. All numbers on final event yield.

5.6.4 Other Systematics

- **Luminosity**: The systematic uncertainty on the luminosity was measured to be 2.2% [83]. As the total integrated luminosity enters the event weight linearly, this value can be applied to the final event yield.
- **Jet Energy Scale**: The calorimetric response of the detector depends on many factors and cannot be predicted precisely. Hence it was measured by the Jet Energy Correction Subgroup [84] with the first CMS data that was delivered. They provide an η and p_T-dependent correction to different types of jets, as well as a corresponding systematic uncertainty. For the analysis the Monte-Carlo jets are shifted corresponding to the factor. To estimate the influence of the systematic uncertainty, the jet energy is shifted up and down corresponding to the delivered values. The influence on the final event yield arising from cuts is the observable for the systematic uncertainty. It corresponds to 2.5% for the backgrounds and up to 10% for the

signals. The value for the signals is a pessemistic estimation that includes points of the phase-space, where the uncertainty is worse than others.

- **Muon Momentum Scale & -Resolution**: They were determined by the muon physics object group using two different approaches [85]. Both use the Z-decay as standard candle. In the first method, a function is fitted to the Z-peak, in the second the peak is compared to a simulation.

  For the muon momentum resolution, a relative extra smearing of 0.5% is found. In this analysis, the corresponding systematic uncertainty is estimated by smearing all muons using a gaussian function of that width. The effect on the event count after all cuts is less than 0.5% for both, signal and backgrounds.

  The uncertainty on the muon momentum scale is found to be less than 0.1% relative to the Z-mass. Hence, in the analysis it is taken into account by shifting all muons up and down by $0.1\% \cdot p_T/(91\,\mathrm{GeV})$. The result on the final event yield is small, 0.5%. This is a satisfying value.

  The effects of smearing and shifting are propagated into $\not\!\!E_T$.

- **Cross Section Uncertainties**: They were already mentioned and listed in section 5.1. Their origin are the uncertainties of the factorisation and renormalisation scale. Taking those two as fully correlated, both are varied up and down by a factor of two [46]. For those backgrounds, where no higher order cross-section and uncertainty are given, an error of 50% is used.

- **Signal Cross Section**: Relying on information from [82] the uncertainty on the signal cross section is assumed to have a 5% contribution from the factorisation scale and additional 7% from NLO-QCD corrections.

- **Trigger Efficiency**: The behaviour of the triggers that are used in data has to be simulated in Monte-Carlo. Especially the efficiency, which is the ratio of the number of events that were triggered by a muon to those, that really contain one, is a potential source of discrepancies. Hence, the trigger efficiency is measured in both Monte-Carlo and Data and the results are compared. Here, results are used that were obtained in the Aachen RPV-group [47]. The trigger efficiency was measured in an independent data sample using the jet-triggered data. It was skimmed with the same requirements as the analysis samples, meaning that at least two muons per event were required with $p_T > 15\,\mathrm{GeV}$ for the leading muon and $p_T > 7\,\mathrm{GeV}$ for the second leading one. The efficiency was defined as

$$\epsilon_{trig} = \frac{\text{events with a muon that triggered}}{\text{events with a muon}}, \tag{5.23}$$

  whereas the muons have to fulfil the full ID requirements described in section 5.3. It was measured depending on the muon transverse momentum and is shown in figure 5.30 for data and $t\bar{t}$-MC. It can be seen, that after the region of the turn-on effects, the efficiency is flat at $92 \pm 1\%$ in data and $94 \pm 1\%$ in Monte-Carlo. The difference between data and Monte-Carlo is of about 2%. This value is included as a systematic uncertainty.

- **Lepton ID Efficiency**: It describes, how efficiently a lepton, here a muon, is reconstructed as one. The muon POG provides a value of 3% as the probability

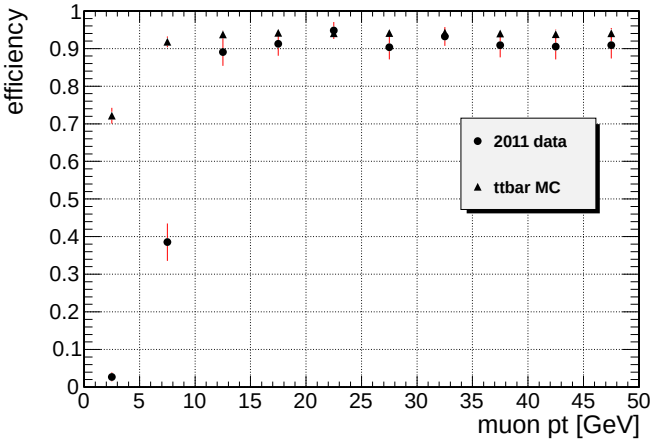

Figure 5.30: Trigger efficiency, as measured in data and $t\bar{t}$-MC depending on the muon p_T. Adopted from [47]. The discrepancy in the low p_T regions is because of the high prescale factors of the triggers with low thresholds. In Monte-Carlo no prescales are applied.

that a muon is mis-reconstructed. In [85] a value of even better than 2% is stated. 3% is included here as systematic uncertainty.

5.6.5 Summary of all Results

After all selection cuts, 26 events are found in data. Applying the tight-to-loose ratio method to estimate the W+Jets and Multijet backgrounds, leads to an overall background prediction of 17.3 events. Now the corresponding uncertainties will be summarised.

The results of the calculations of the systematic uncertainties are listed in table 5.9. The numbers in that table are applied to all samples equally. Others, that are marked $(*)$ have an individual contribution to different backgrounds and are treated separately. The listed uncertainties are added in quadrature to gain the total uncertainty for background and signal, respectively. The last three lines indicate uncertainties, that are treated completely separated from those described before.

Table 5.10 shows the event yields of the remaining background contributions after all cuts with their individual systematic uncertainties. The statistical error comes from the Monte-Carlo statistics. The listed systematic errors in the last column are obtained from the numbers in table 5.9, whereas the individual errors were added in quadrature. QCD and W+Jets predictions come from the T/L-method and the 30% systematic uncertainty is applied.

The uncertainties of the T/L-predictions are assumed to be 100% correlated. Hence they are added linearly to the other uncertainties, which are added in quadrature.

Uncertainty	BG [%]	Signal [%]
Pileup	2.5	1.0
PDF	$*$	6.0
Jet Energy Resolution	0.5	1.0
Jet Energy Scale	2.5	10.0
Muon Scale	0.5	0.5
Muon Resolution	0.5	0.5
Cross Section	$*$	8.6
$\sum$	3.6	14.6
Luminosity	2.2	
Lepton ID	3.0	
Trigger Efficiency	2.0	

Table 5.9: Summary of systematic uncertainties for the sum of all used Standard Model backgrounds and the numbers that are used for the signals. Asterisks ($*$) indicate, that these uncertainties are determined for every background sample individually. Those numbers are not included into the sum.

Background	Events	$\pm$ Stat. Err.	$\pm$ Syst. Err.
WWW	0.49	0.04	0.25
$W^{\pm}W^{\pm}$	0.32	0.01	0.16
$t\bar{t}+V$	0.58	0.03	0.29
Single top	0.72	0.28	0.07
$WZ \rightarrow 3L\nu$	1.94	0.08	0.10
$ZZ \rightarrow 4L$	0.20	0.01	0.01
$t\bar{t}$	6.48	0.38	0.57
$W + Jets(T/L)$	4.99	–	1.50
$QCD(T/L)$	1.59	–	0.48
$\sum$	17.31	0.48	2.70

Table 5.10: Backgrounds that contribute after all cuts, shown with individual event numbers and statistical and systematic uncertainties.

5.7 Limit Calculation

Even though the measurements result in a slight excess, it should be possible to exclude values of λ'_{211} to a certain degree. The excess seems not significant enough that one could claim a discovery, what is why exclusion limits are calculated. The limit is set in the m_0-$m_{1/2}$-plane as the 95% C.L. limit on the coupling parameter λ'_{211}. For that purpose, the grid of signal points (refer to sec. 5.1.3) is used. Their values for the systematic uncertainties are adopted from the studies of the CMS benchmark point samples.

5.7.1 The CL_s Method

To quantify the agreement of measured data with respect to the signal prediction, a statistical method is used that is able to consider different variables like systematic un-

certainties. Here, a modified frequentist method is used that is known as the CL_s-method [86, 87]. It compares two hypotheses. In particle physics, the first hypothesis usually is the prediction from the Standard Model. It is often referred to as the null-hypothesis, here H_0. The second hypothesis is the signal hypothesis H_1. It contains the predictions from both, signal and Standard Model added.

The definition of CL_s is

$$CL_s = \frac{CL_{s+b}}{CL_b} \tag{5.24}$$

and it excludes a signal hypothesis by a confidence level (CL), if

$$1 - \mathrm{CL_s} \leq CL. \tag{5.25}$$

CL_{s+b} and CL_b represent the confidences, that the measured (observed) result corresponds to the hypotheses H_1 or H_0 respectively. They are calculated by

$$CL_x = P_x(Q \leq Q_{obs}) = \int_{-\infty}^{Q_{obs}} f_x(Q)\mathrm{d}Q. \tag{5.26}$$

The $f_x(Q)$ are probability distribution functions (pdf) that are obtained by performing pseudoexperiments that are based on the background prediction. More precise, Q is calculated from the pseudoexperiments and being histogramed (cf. fig 5.31). The pdf is the resulting envelope function. Q is a likelihood ratio of the likelihood of hypothesis H_1 to that of H_0:

$$Q = \frac{\mathcal{L}(s+b, n)}{\mathcal{L}(b, n)}, \tag{5.27}$$

where n is the expected mean of the corresponding hypothesis, that is diced following a poisson distribution. Using a likelihood ratio allows to combine several channels by multiplying their individual ratios.

Looking at figure 5.31 again, it becomes clear, what the integrals of equation 5.26 are. It shows the distribution of $-2\ln(Q)$. The vertical line is the result that is computed by using the measured data - the observation. The distribution of the null hypothesis is represented by the blue line and is integrated from infinity to the observation, so that CL_b is the area under the blue line excluding the yellow part. The same procedure is applied to the alternative hypothesis H_1. The green area shows the result for CL_{s+b}.

As the yellow area is rather small, the background hypothesis is well fulfilled. Not so the alternative hypothesis. The green area fills only about half of its distribution. Using guessed example values $CL_b = 0.9$ and $CL_{s+b} = 0.5$ leads to $CL_s = 0.56$ and hence to an exclusion limit of $CL = 0.44$. This cannot be called a proper exclusion as in this case usually an exclusion of $CL \geq 0.95$ is required.

5.7.2 Parameter Modelling

The limit-setting is performed as a single bin counting experiment. That means, the final distributions of the analysis are integrated and only the total event counts of the different contributions enter the calculation. The choice of the test statistic, as well as the modelling of parameters that is used here, is based on an agreement of LHC Higgs search

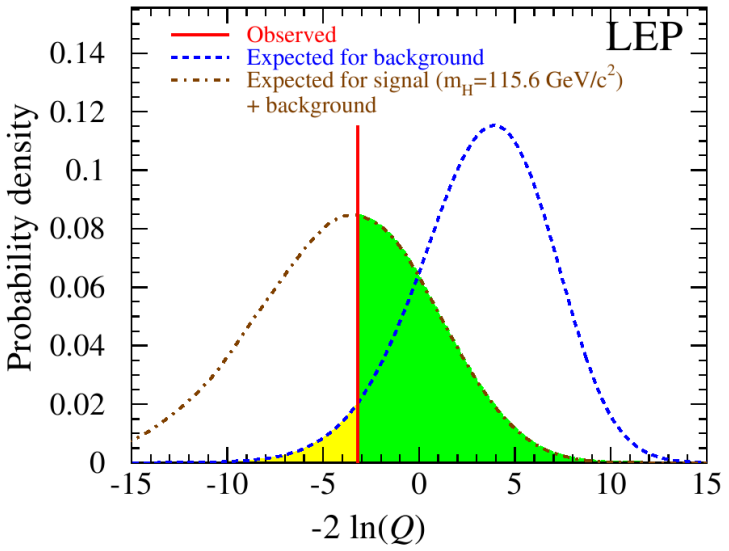

Figure 5.31: Example for a probability density function [86].

groups from CMS and ATLAS [88] that is recommended to other CMS searches. It has some modifications compared to the CL_s method described before.

The test statistic is a profile likelihood ratio

$$Q = -2 \ln \frac{\mathcal{L}(\mu \cdot s + b, n, \hat{\theta}_\mu)}{\mathcal{L}(\hat{\mu} \cdot s + b, n, \hat{\theta})}, \; 0 \leq \hat{\mu} \leq \mu, \tag{5.28}$$

with the expectations from signal s, background b, the poisson-distributed pseudo-data (or observed data) n and the signal strength parameter μ that scales the signal prediction. Systematic uncertainties are included into the likelihoods by multiplying nuisance parameters θ. $\hat{\mu}$ and $\hat{\theta}$ are obtained from the global likelihood maximum, whereas $\hat{\theta}_\mu$ depends on a given μ and n. With that test statistic, $\mathrm{CL_s}$ is determined depending on μ. To find an upper confidence level (CL), μ is varied, until $CL_s = 0.05$ is reached.

The nuisance parameters are modelled with log-normal functions that are able to deal with large systematic uncertainties better than a Gaussian. Additionally, a Gaussian might be a bad choice to describe positively defined observables like cross sections or luminosity, in case it falls below 0 [88].

5.7.3 Results

Using the methods described before and the quoted numbers, the expected and observed upper limits are computed using the ROOSTATS package [89].

With that method, an upper limit on the signal cross section is computed. As $\sigma \propto (\lambda'_{ijk})^2$ it is possible to convert the results into a limit on the coupling parameter:

$$\lambda'_{211}(CL_{95}) = \lambda'_{211}(0) \cdot \sqrt{\frac{\sigma(CL_{95})}{\sigma(0)}} \tag{5.29}$$

Here, $\lambda'_{211}(0) = 0.01$ and $\sigma(0)$ is the corresponding signal cross section.

The results are shown in figure 5.32. The deviations between the observed and the expected upper limits are histogramed in figure 5.33(a) in terms of standard deviations. They have values distributed around 1.8σ. As a cross-check, the observed limits are recomputed using the Higgs-Combine tool [90], as shown in figure 5.33(b). The ROOSTATS results are systematically higher than those from Higgs-Combine by $\approx 5\%$.

Comparing the limits to those of D0 at Tevatron [17] (cf. figure 3.5(b)) it can be seen that the range in the m_0-$m_{1/2}$-plane could be extended significantly. In the region that is covered by both analyses, the limit on λ'_{211} is improved by approximately a factor 10. Compared to the reinterpretation of searches for like-sign dileptons with ATLAS data [14], figure 3.5(c), the results are very similar. It has to be mentioned that the choice of the remaining CMSSM parameters differs in all three analyses. The D0 analysis uses $\tan\beta = 5$, $sign(\mu) < 0$ and $A_0 = 0$, while the limits of the reinterpretation are presented in a sparticle mass plane and thus independent of a certain CMSSM parameter set.

5.8 Candidate Events

Table 5.11 lists all events measured in data, that survive the analysis cuts. The last two columns show the reconstructed invariant jet-dimuon and jet-muon masses, that correspond to the hypothetical slepton- and gaugino-masses.

The values of the masses point out, that regions of excesses in the slepton mass like the one at $700\,\text{GeV} - 750\,\text{GeV}$ in figure 5.14 right, do not necessarily correspond to an excess in the reconstructed gaugino mass (same figure, left).

Figure 5.34 shows the display of one typical event that illustrates the features the search is based on. It is a clean event with two jets and only a small amount of $\not{E}_T$. Jets and muons have medium transverse momenta and the reconstructed masses correspond to $m(\tilde{l}) = 294\,\text{GeV}$ and $m(\tilde{\chi}) = 172\,\text{GeV}$. It can be seen, that not the angle between the two muons but between one muon and the combined dijet-muon particle make the event's back to back topology. Trying different combinations of the available particles including $\not{E}_T$ to reconstruct masses does not lead near a known resonance like W or Z.

5.9 Discussion and Further Thoughts

Since a moderate excess was found in data, some further possibilities of its origin need to be discussed. Different ways of how to imitate the like-sign signal with Standard Model backgrounds were mentioned and examined, such as faked or non-prompt muons. But there is another way, which is that the charge of one muon could be measured incorrectly. In that case, a simple Drell-Yan event with additional jets from initial state radiation would mimic the signal.

There are two possibilities why the charge-flip could not contribute to this analysis. As this effect is expected to be quite rare because of the good muon trajectory resolution, it could be a statistical effect. In principal, the statistics of the used Drell-Yan sample is quite high with per-event weights less than one. But in regions of high momenta (resp. Z-masses) the statistical coverage becomes bad (cf. figure 5.13(b)). It is in that region,

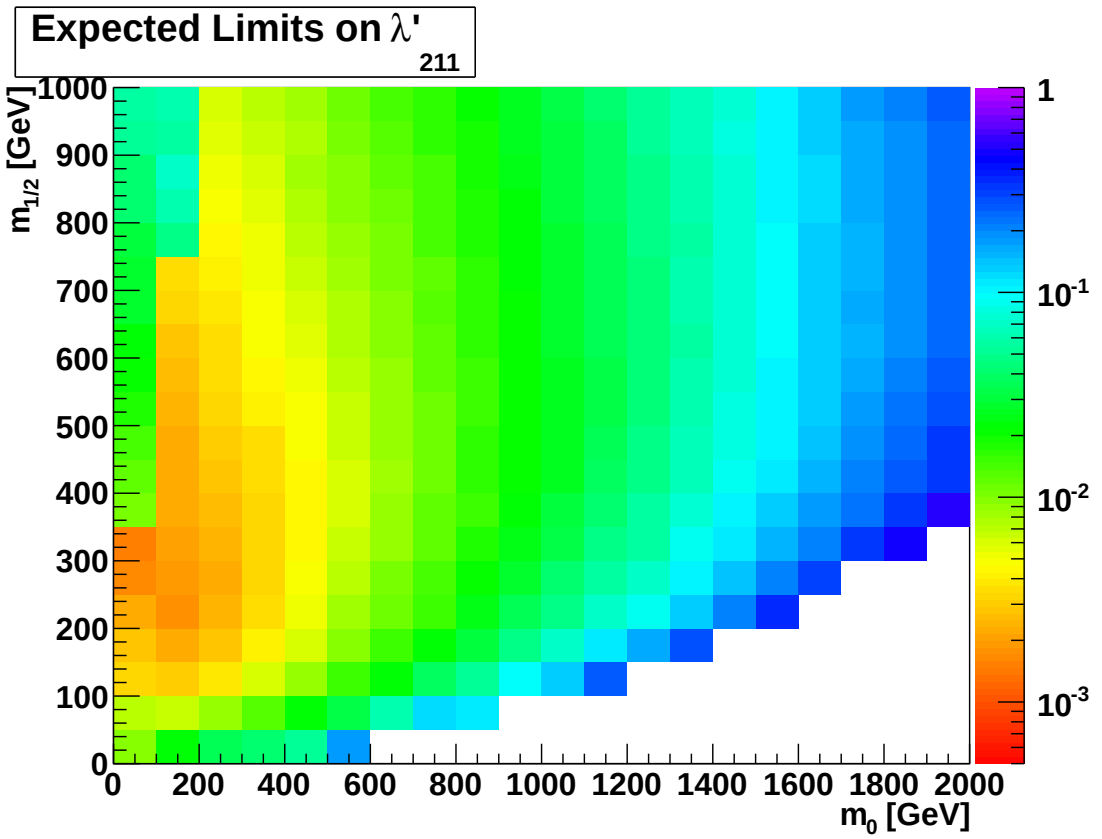

(a) Expected upper limit on λ'_{211}. The plot shows the coupling excluded at 95% C.L.

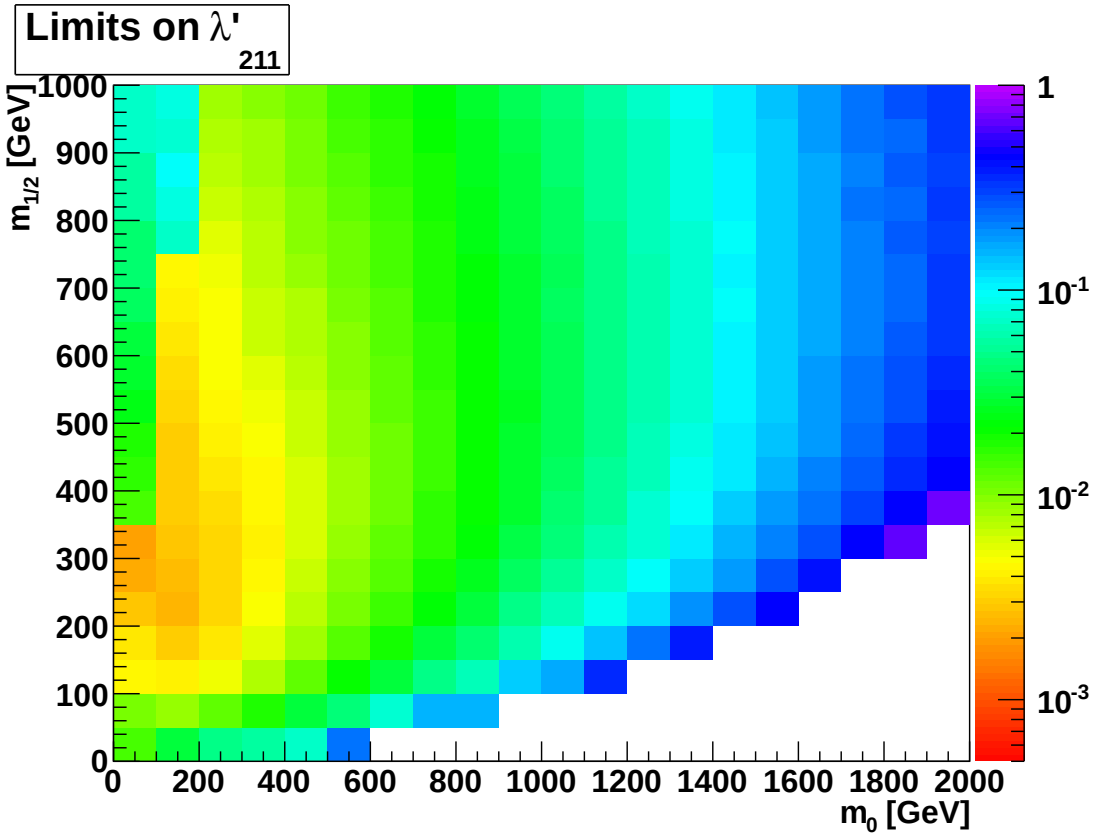

(b) Measured upper limit on λ'_{211}. The plot shows the coupling excluded at 95% C.L.

Figure 5.32: Limit plots obtained with the ROOSTATS package.

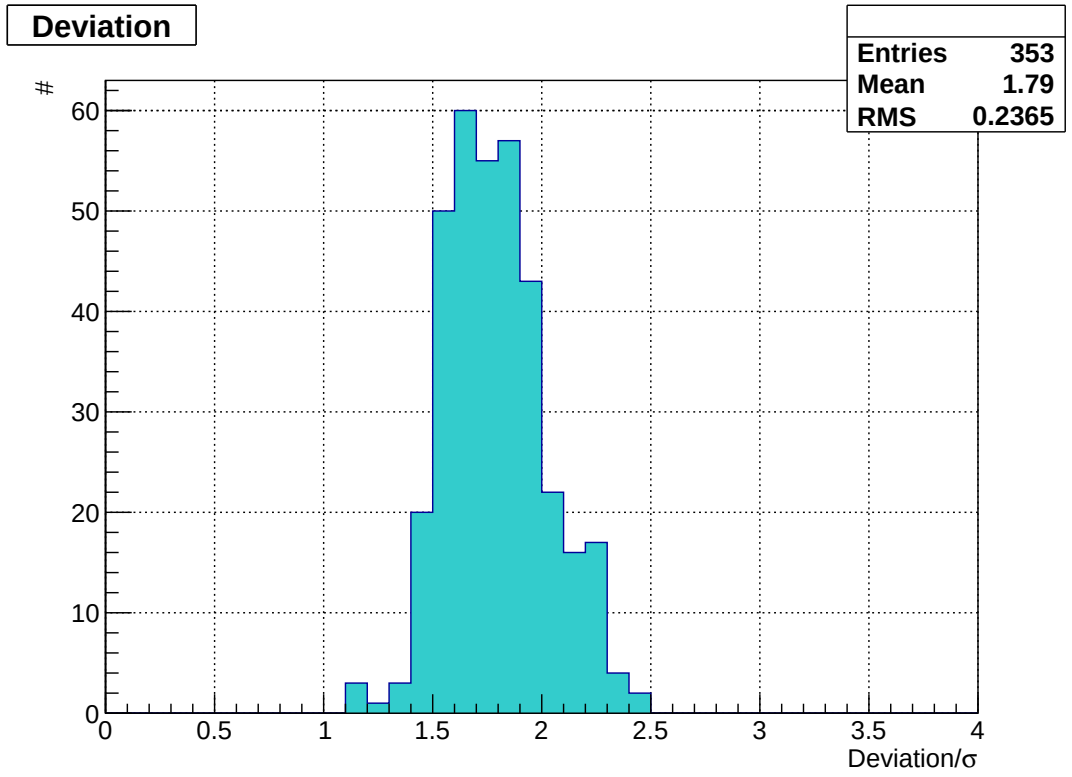

(a) Difference between expected and measured limit in σ.

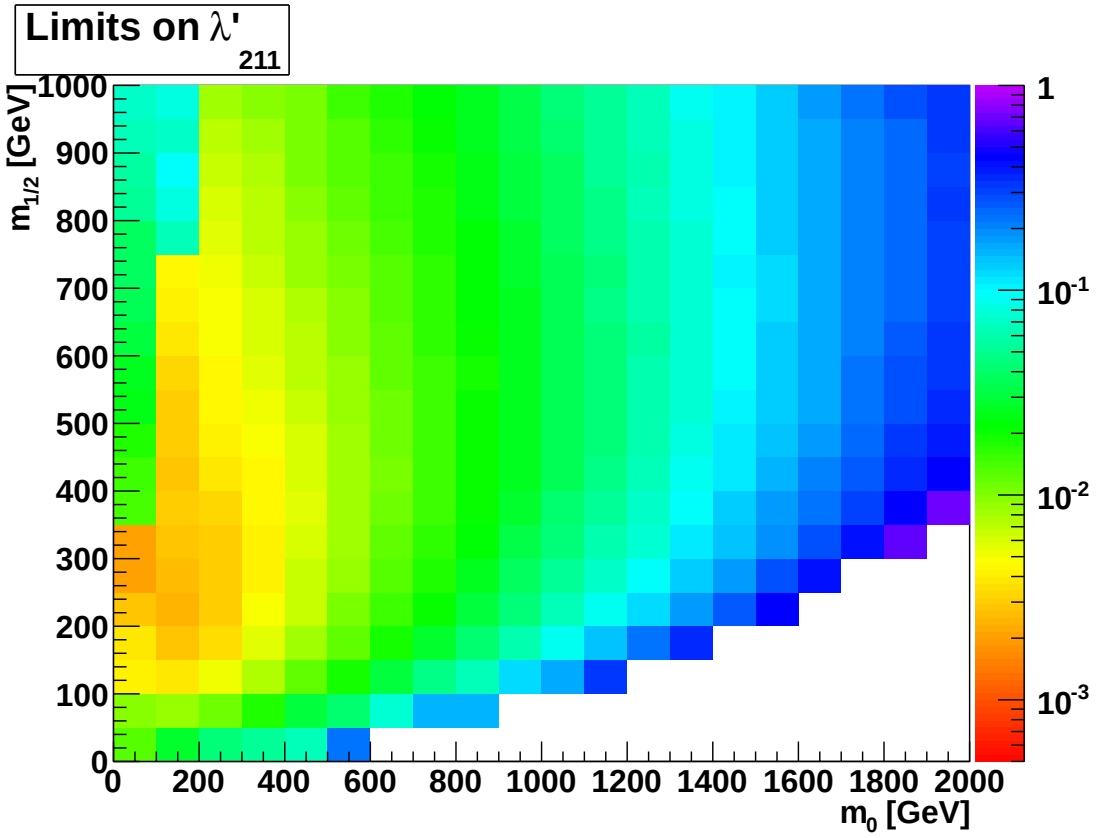

(b) Measured upper limit on λ'_{211}. The plot shows the coupling excluded at 95% C.L. The calculation was done using the Higgs-Combine package.

Figure 5.33

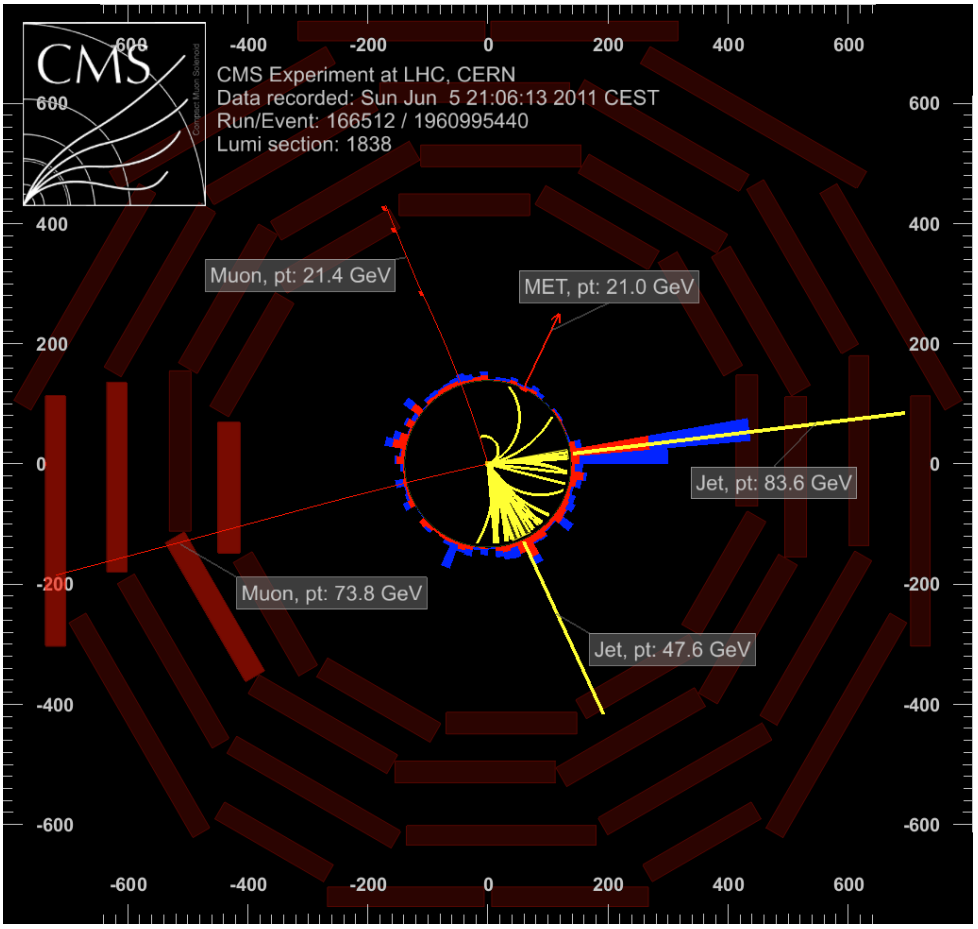

(a) View of the ρ-ϕ-plane.

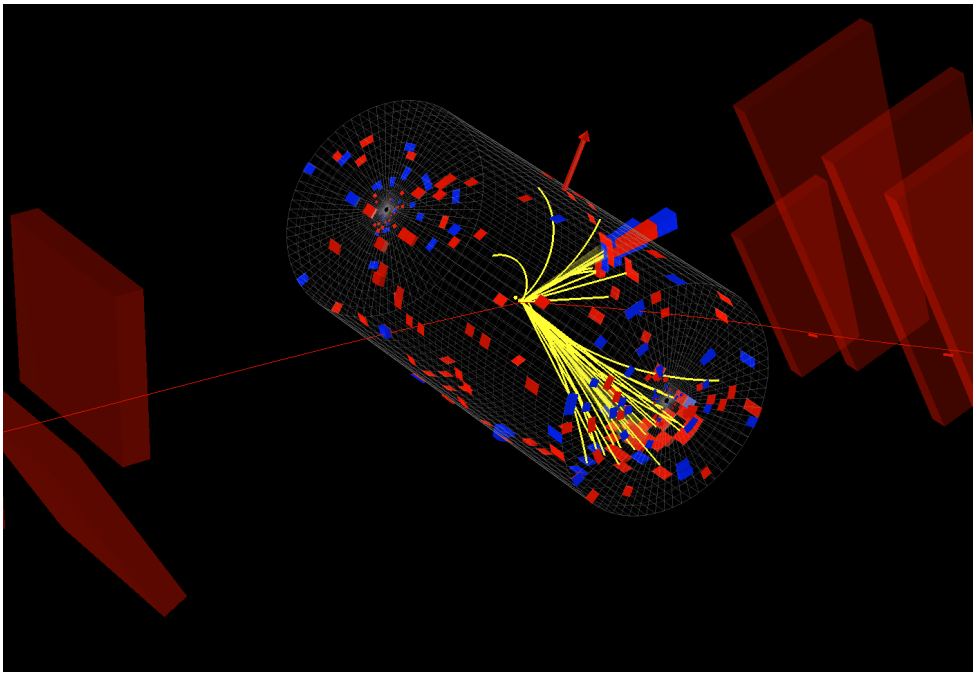

(b) 3D-view

Figure 5.34: Example for an event surviving all selection cuts, measured in data. Further properties: $m(\mu_1, \mu_2, \text{jets}) = 294.4\,\text{GeV}$, $m(\mu_2, \text{jets}) = 172.3\,\text{GeV}$

#	Event	Run	Lumi Sec.	$m(\tilde{l})$ [GeV]	$m(\tilde{\chi})$ [GeV]
1	1043945016	173692	727	749	666
2	120604108	178970	102	271	153
3	123849719	167676	136	317	275
4	139613388	166784	144	477	371
5	147072872	167746	133	402	281
6	1502851976	167807	1215	380	308
7	1899449147	167807	1593	375	246
8	1960995440	166512	1838	294	172
9	206697197	170854	199	612	551
10	229894176	179497	183	676	292
11	281242923	176304	223	386	264
12	2823842297	173692	2162	284	202
13	282811171	166033	206	306	270
14	28354675	176468	19	636	591
15	28913697	179476	29	227	110
16	315939955	180076	174	258	176
17	346617209	171050	273	429	241
18	40043881	161008	65	202	139
19	45811820	176201	58	210	101
20	463960899	172868	334	351	219
21	499712875	176309	412	337	177
22	513532091	176309	423	739	549
23	552288010	167898	466	171	130
24	553847916	172033	418	291	267
25	56669144	179889	65	718	447
26	77393327	177096	53	872	833

Table 5.11: The data events that remain after the complete analysis procedure with the reconstructed slepton- and gaugino masses.

where one would expect a possible charge-flip to be most probable, as the muon trajectory becomes straighter with increasing momentum.

Another possibility is, that the charge mis-reconstruction is not properly simulated in Monte-Carlo. Trying to estimate contributions of muon charge mis-reconstruction in data would allow to clarify both of the previously described possibilities.

Finding out, if a charge-flip effect is correctly simulated is difficult. Here, a rough and very pessimistic estimate is presented which effect the charge mis-reconstruction could have.

For that purpose, results based on "Cosmic Run At Four Tesla" (CRAFT) data, relying on cosmic muon measurements of the time before LHC operation are used [91]. Cosmic muons passing through the detector were split into an upper and a lower part from point of view of the beam axis and both charges were determined. Figure 5.35(a) shows the probability,that the charges differ with respect to the measured momentum of the upper muon part.

The values of the global muon fit (black dots) are taken to obtain figure 5.35(b). The

column on the left represents the number of background events as given by the analysis before the like-sign cut. In the middle the effect of the cut is shown, completely based on Monte-Carlo prediction (no T/L-results). The right column shows the events of the left one, whereas each event is weighted with its probability that the charge of one of the two muons was mis-reconstructed.

This probability is calculated by

$$P = P(p_T(\mu_1)) + P(p_T(\mu_2)) - 2P(p_T(\mu_1))P(p_T(\mu_2)), \tag{5.30}$$

where $P(p_T(\mu_i))$ is the probability for a mis-reconstructed charge depending on the transverse momentum of the i_{th} muon, taken from the global muon values (black dots) of the plot in figure 5.35(a).

With that prediction more than thirty events from Drell-Yan are expected, which would be very much compared to 26 events measured in data. But as mentioned before, this can only be a very rough estimation. On the one hand, the detector alignment is expected to be improved since this measurement. On the other hand, the values are connected to global muons only. The ID criteria that are used in this analysis should lower the values considerably.

Another way to determine the charge flip effect would be to do a measurement in data. This measurement is far from being trivial as one has to assume that in case of a mis-reconstructed charge, the momentum would be measured wrong too. This measurement is not performed here and thus the conclusion is, that with the result from the cosmics, a contribution to the final selection, caused by charge mis-reconstruction is possible, but cannot trustfully be determined and thus is not considered in the results.

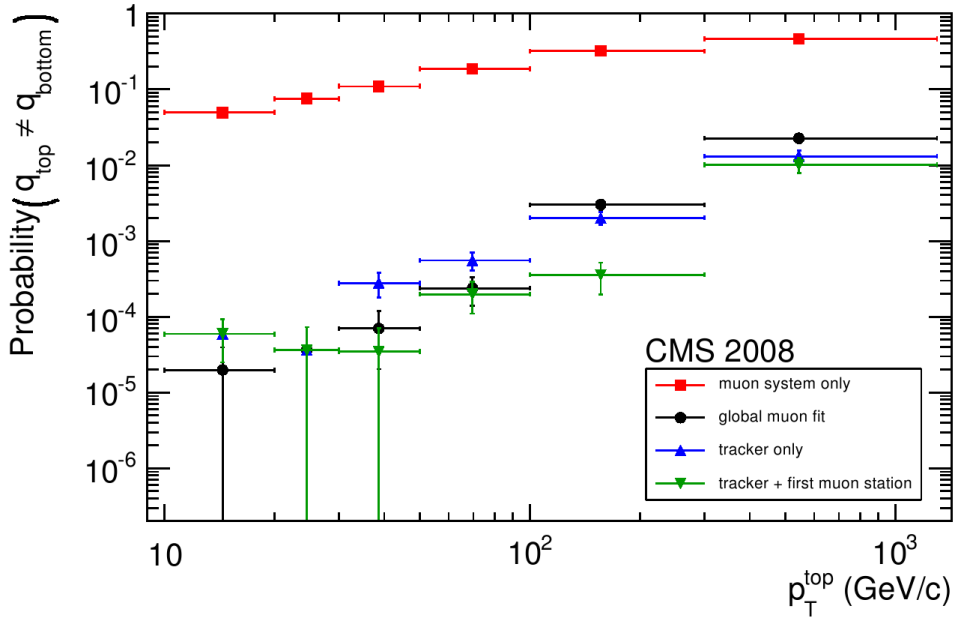

(a) The probability of a charge mis-reconstruction measured with cosmic muons [91].

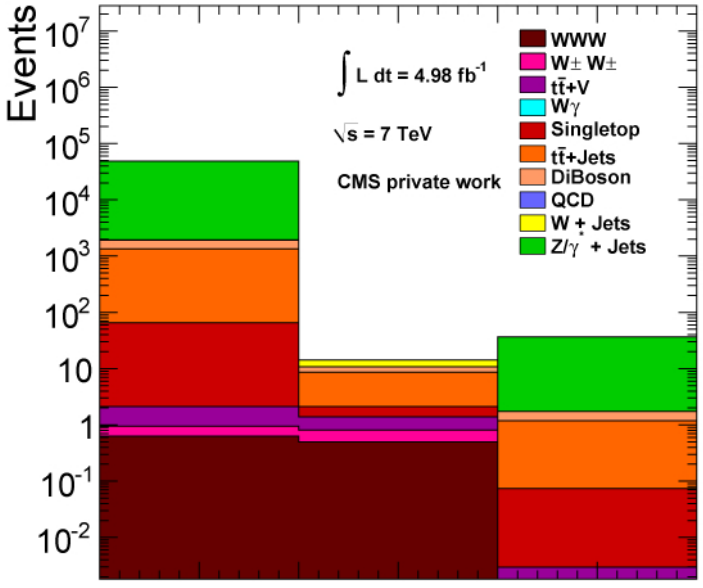

(b) Rough, pessimistic estimation of the influence of charge mis-reconstruction. Left column: Monte-Carlo background prediction before applying the same charge cut. Middle: Background prediction after this cut. Right: Estimated contribution of charge-flip events (ref. to text).

Chapter 6

Conclusions & Outlook

This thesis presents a search for resonantly produced sleptons of the second generation. Based on the baryon triality model, the supersymmetric theory includes a mechanism to violate R-parity. The yukawa coupling that was examined is λ'_{211} that enables the resonant production of a smuon or a muon sneutrino from two quarks. Concerning the final state, the search was limited to two muons and jets.

Several cuts were optimized and applied to increase the signal-to-background ratio. It was taken advantage of the lepton number violation that is implied by the coupling λ'_{211}, by requiring the muons to have same charges. This cut drastically increases the signal to noise ratio as it removes most of the Standard Model background. Several systematic uncertainties have been considered.

Background contributions, that show signal properties because of non-prompt or faked muons were estimated using a data-driven approach known as the tight-to-loose-ratio method. Additional contributions could originate from muon charge mis-reconstruction but were not considered here. After all selection cuts the number of events remaining is:

Data:	26 events
SM-Background:	17.31 ± 0.48 (MC stat.) ± 2.80 (syst.) events

The difference is moderate, around 1.8σ assuming a statistical uncertainty of $\sqrt{17.31}$events on the background, and there is no significant sign for a discovery. Hence, exclusion limits on the value of the coupling λ'_{211} were calculated in the m_0-$m_{1/2}$-plane using the CL_s-method. The results exceed those from the Tevatron in the range of the considered parameter space and in overlapping regions, the limits could be improved by approximately a factor 10. The limits lie in regions from $\lambda'_{211} < 0.002$ to $\lambda'_{211} < 0.708$.

The small observed excess is a great motivation to proceed with the analysis with 2012 and future data. If it has statistical reasons, it is very likely that it decreases, allowing significantly tighter exclusion limits. In case that it has a physics reason, more data will allow a closer look at its origin. Future searches could also widen the parameter space, as the barriers of $m_0 = 2000\,\text{GeV}$ and $m_{1/2} = 1000\,\text{GeV}$ are quite arbitrary and one can see from the limit plots that there is still potential for further exclusions. Furthermore, higher energies will push the boundaries for exclusion (or those that hide a potential discovery), especially in the m_0-direction.

In any case, a future analysis can benefit from the results shown here, for example in questions of signal Monte-Carlo generation. The selection efficiencies differ considerably between the signal points and it is possible to tune the number of generated events to the required individual statistic in the parameter space regions that were considered here.

In principal the search could be extended to other final states. Those include decays into neutrinos and thus $\not{E}_T$-signatures. Their disadvantage is that it is not possible to fully

reconstruct the sparticle masses -only transverse masses- and that the cut on same muon charges cannot be used. This case leads to significances that are considerably worse but as an additional source for statistical interpretation this still might become interesting.

Appendix A

Standard Model Background Monte-Carlo Samples

Please turn the page.

Monte-Carlo Sample	σ [pb]	Gen. Events
DYJetsToLL_M-10To50_TuneZ2_7TeV-madgraph_Fall11-PU_S6_START42_V14B-v1_AODSIM	9611	31280628
DYJetsToLL_TuneZ2_M-50_7TeV-madgraph-tauola_Fall11-PU_S6_START42_V14B-v1_AODSIM	$3048 \pm 34 **$	35982657
TTJets_TuneZ2_7TeV-madgraph-tauola_Fall11-PU_S6_START42_V14B-v1_AODSIM	$165 \pm 10 * *$[41]	49254221
WJetsToLNu_TuneZ2_7TeV-madgraph-tauola_Fall11-PU_S6_START42_V14B-v1_AODSIM	$31314 \pm 407 **$	59940000
QCD_Pt-15to20_MuPt5Enriched_TuneZ2_7TeV-pythia6_Fall11-PU_S6_START42_V14B-v1_AODSIM	$579.2 \cdot 10^6$	2564156
QCD_Pt-20to30_MuPt5Enriched_TuneZ2_7TeV-pythia6_Fall11-PU_S6_START42_V14B-v1_AODSIM	$236.3 \cdot 10^6$	10076800
QCD_Pt-30to50_MuPt5Enriched_TuneZ2_7TeV-pythia6_Fall11-PU_S6_START42_V14B-v1_AODSIM	$53.07 \cdot 10^6$	10830209
QCD_Pt-50to80_MuPt5Enriched_TuneZ2_7TeV-pythia6_Fall11-PU_S6_START42_V14B-v1_AODSIM	$6351 \cdot 10^3$	10830209
QCD_Pt-80to120_MuPt5Enriched_TuneZ2_7TeV-pythia6_Fall11-PU_S6_START42_V14B-v1_AODSIM	$785.1 \cdot 10^3$	8213422
QCD_Pt-120to150_MuPt5Enriched_TuneZ2_7TeV-pythia6_Fall11-PU_S6_START42_V14B-v1_AODSIM	92950	7933763
QCD_Pt-150_MuPt5Enriched_TuneZ2_7TeV-pythia6_Fall11-PU_S6_START42_V14B-v1_AODSIM	47580	3935565
T_TuneZ2_s-channel_7TeV-powheg-tauola_Fall11-PU_S6_START42_V14B-v1_AODSIM	$3.19 \pm 0.06 * *$[42]	259971
T_TuneZ2_t-channel_7TeV-powheg-tauola_Fall11-PU_S6_START42_V14B-v1_AODSIM	$41.92^{+1.59}_{-0.21} * *$[43]	3900171
T_TuneZ2_tW-channel-DR_7TeV-powheg-tauola_Fall11-PU_S6_START42_V14B-v1_AODSIM	$7.87 \pm 0.20 * *$[44]	814390
Tbar_TuneZ2_s-channel_7TeV-powheg-tauola_Fall11-PU_S6_START42_V14B-v1_AODSIM	$1.44 \pm 0.01 * *$[42]	137980
Tbar_TuneZ2_t-channel_7TeV-powheg-tauola_Fall11-PU_S6_START42_V14B-v1_AODSIM	$22.65 \pm 0.50 * *$[43]	1944826
Tbar_TuneZ2_tW-channel-DR_7TeV-powheg-tauola_Fall11-PU_S6_START42_V14B-v1_AODSIM	$7.87 \pm 0.20 * *$[44]	323401
WWJetsTo2L2Nu_TuneZ2_7TeV-madgraph_Fall11-PU_S6_START42_V14B-v1_AODSIM	$4.51 \pm 0.16*$	1197558
WZJetsTo2L2Q_TuneZ2_7TeV-madgraph_Fall11-PU_S6_START42_V14B-v1_AODSIM	$1.24 \pm 0.05*$	932332
WZJetsTo3LNu_TuneZ2_7TeV-madgraph_Fall11-PU_S6_START42_V14B-v1_AODSIM	$0.60 \pm 0.02*$	1221000
ZZJetsTo2L2Nu_TuneZ2_7TeV-madgraph_Fall11-PU_S6_START42_V14B-v1_AODSIM	$0.238 \pm 0.006*$	1103468
ZZJetsTo2L2Q_TuneZ2_7TeV-madgraph_Fall11-PU_S6_START42_V14B-v1_AODSIM	$0.83 \pm 0.02*$	1013369
ZZJetsTo4L_TuneZ2_7TeV-madgraph_Fall11-PU_S6_START42_V14B-v1_AODSIM	$0.060 \pm 0.002*$	1165188
WGToMuNuG_TuneZ2_7TeV-madgraph_Fall11-PU_S6_START42_V14B-v1_AODSIM	114.6	520066
TTWTo2Lplus2Nu_7TeV-madgraph_Fall11-PU_S6_START42_V14B-v1_AODSIM	0.0068	48764
TTWTo2Lminus2Nu_7TeV-madgraph_Fall11-PU_S6_START42_V14B-v1_AODSIM	0.0027	50435
TTZTo2Lplus2Nu_7TeV-madgraph_Fall11-PU_S6_START42_V14B-v1_AODSIM	0.0020	36740
TTZTo2Lminus2Nu_7TeV-madgraph_Fall11-PU_S6_START42_V14B-v1_AODSIM	0.0019	36781
WWminusTo2L2Nu_7TeV-madgraph_Fall11-PU_S6_START42_V14B-v1_AODSIM	0.0016	51063
WWplusTo2L2Nu_7TeV-madgraph_Fall11-PU_S6_START42_V14B-v1_AODSIM	0.0042	48244
WWWTo2Lminus2Nu_7TeV-madgraph_Fall11-PU_S6_START42_V14B-v1_AODSIM	0.0041	16147
WWWTo2Lplus2Nu_7TeV-madgraph_Fall11-PU_S6_START42_V14B-v1_AODSIM	0.0152*[45]	43322

Table A.1: Standard Model Background Monte-Carlo: *NLO, **NNLO, ***NNLL cross-sections. Higher order cross-sections from [46], if no other source is given. Cross sections without further information are from the generator output.

Appendix B

Object ID Plots

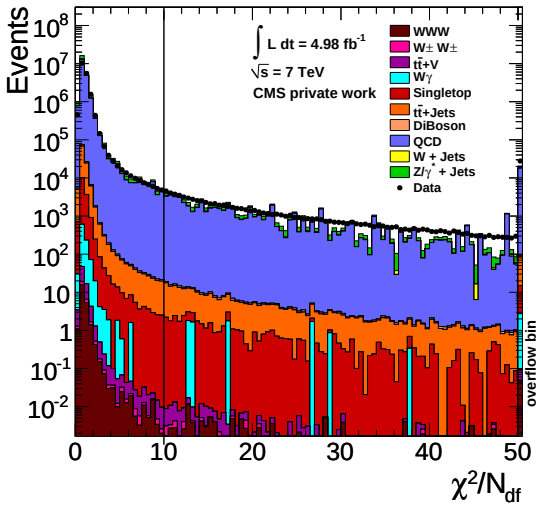

(c) $\chi^2/N_{df} < 10$: The quality of the global muon fit.

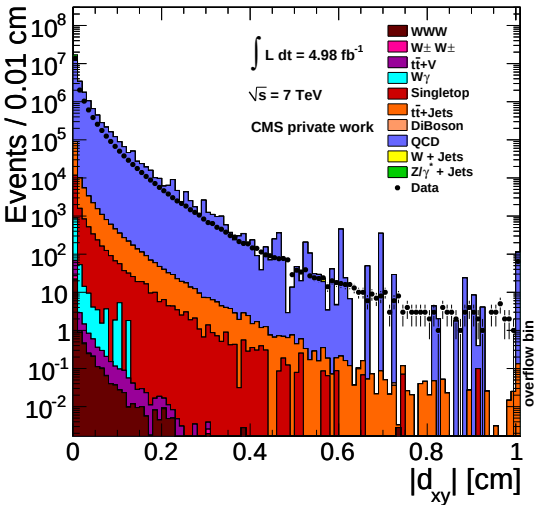

(d) $|d_{xy}| < 0.2\,\text{cm}$: The impact parameter of the muon trajectory w.r.t. the primary vertex.

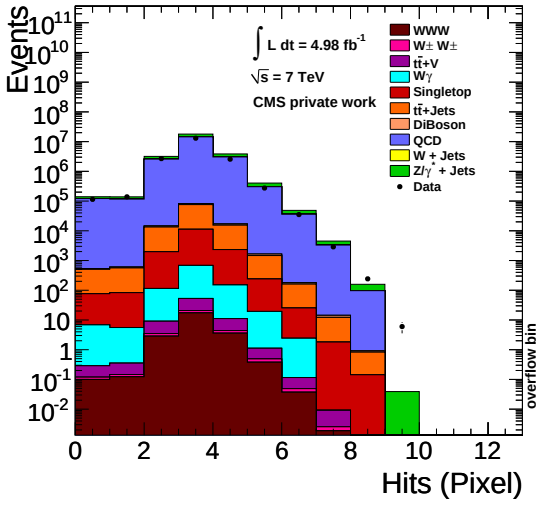

(e) Number of pixel hits in the tracker.

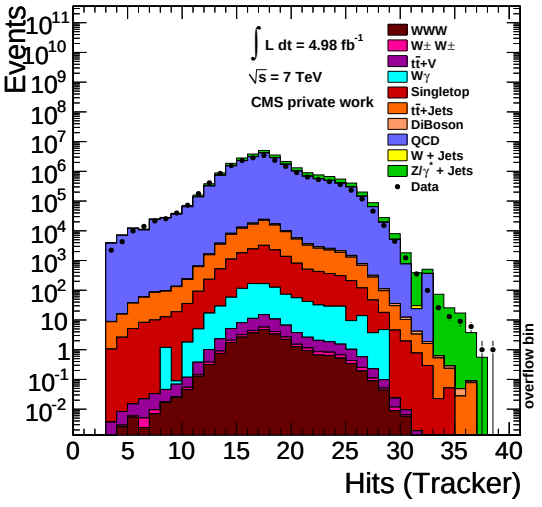

(f) Number of total hits in the tracker.

Figure B.1: N-1-plots of the muon-ID variables.

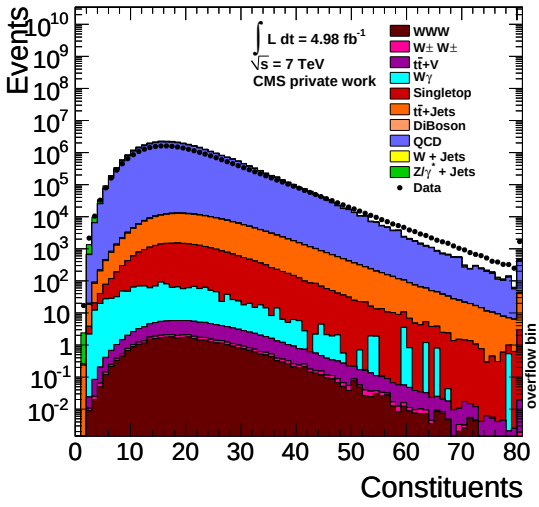

(a) #Constituents > 1

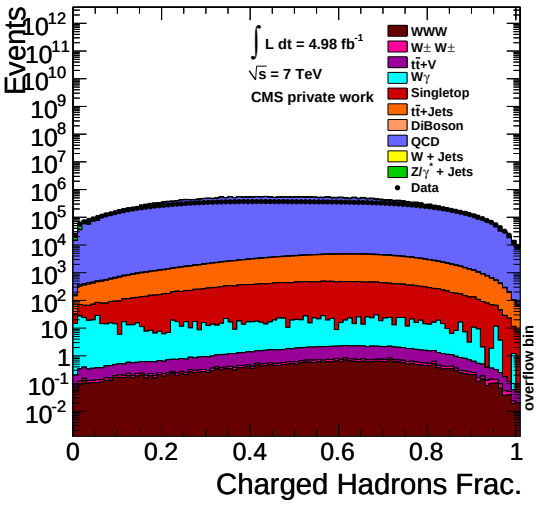

(b) Charged hadron fraction > 0

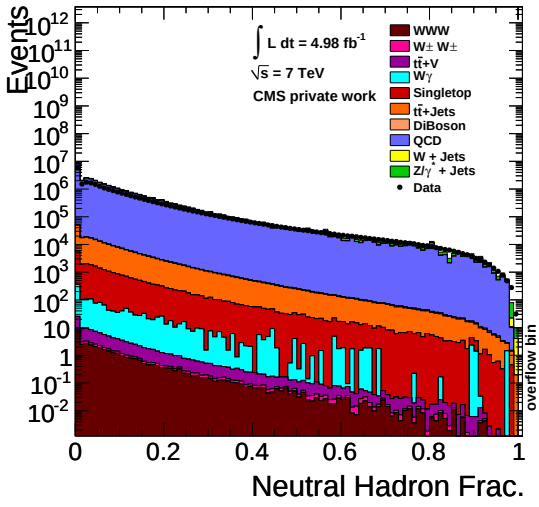

(c) Neutral hadron fraction < 0.99

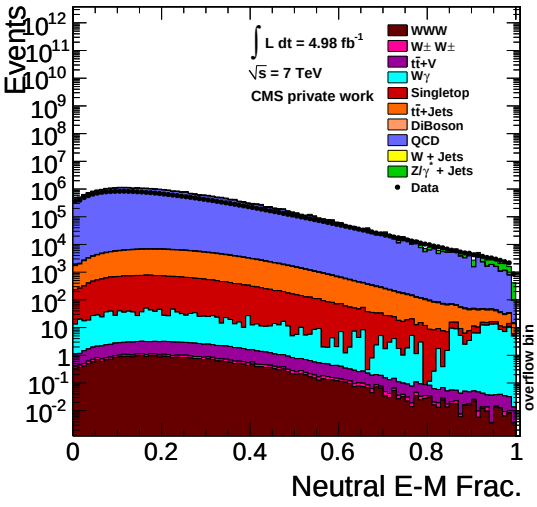

(d) Neutral EM fraction < 0.99

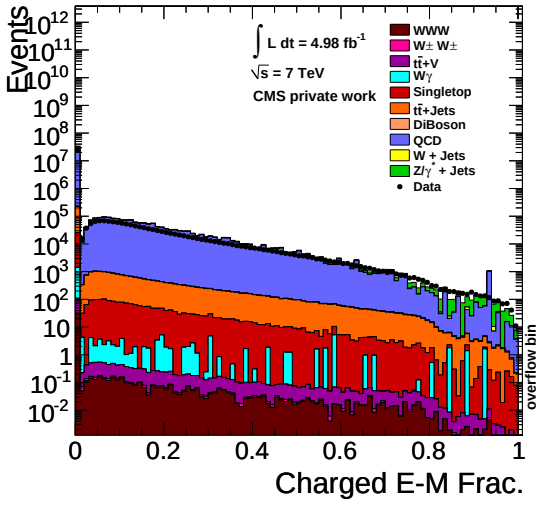

(e) Charged EM fraction < 0.99

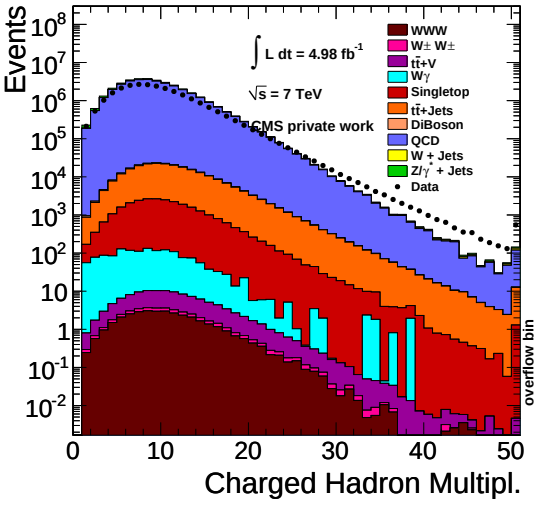

(f) Number of charged hadrons > 0

Figure B.2: N-1-plots of the Particle-Flow Jet-ID variables. For the meaning of the variables, see section 5.3.

Appendix C

PDF-Uncertainty Results

	CTEQ10			MSTW2008			NNPDF	
[%]	PDF	α_s	combined	PDF	α_s	combined	weighted mean	random replicas
$W \to \mu\nu$	+ (4.2) - (4.5)	+ (-0.4) - (0.4)	+ (4.2) - (4.5)	+ (4.1) - (3.3)	+ (-0.3) - (-0.3)	+ (4.1) - (3.3)	3.9	3.9
$t\bar{t}$	+ (5.5) - (5.1)	+ (0.0) - (0.1)	+ (5.5) - (5.1)	+ (3.2) - (3.7)	+ (0.2) - (0.2)	+ (3.2) - (3.7)	4.1	4.1
$WZ \to 3L\nu$	+ (1.5) - (1.8)	+ (0.1) - (-0.1)	+ (1.5) - (1.8)	+ (1.5) - (1.1)	+ (0.2) - (0.2)	+ (1.5) - (1.1)	1.3	1.3
$ZZ \to 4L$	+ (2.0) - (2.3)	+ (0.0) - (-0.0)	+ (2.0) - (2.3)	+ (1.9) - (1.5)	+ (0.2) - (0.2)	+ (1.9) - (1.6)	1.6	1.6
$t(tW)$	+ (6.7) - (5.7)	+ (1.0) - (-0.9)	+ (6.8) - (5.8)	+ (4.7) - (5.4)	+ (1.3) - (1.3)	+ (4.8) - (5.5)	6.3	6.3
$\bar{t}(tW)$	+ (9.0) - (8.1)	+ (0.7) - (-0.5)	+ (9.1) - (8.1)	+ (6.0) - (7.5)	+ (1.2) - (1.2)	+ (6.1) - (7.6)	8.1	8.1
$W^+W^+W^-$	+ (3.5) - (5.0)	+ (-0.3) - (0.3)	+ (3.6) - (5.0)	+ (2.9) - (2.2)	+ (-0.1) - (-0.1)	+ (2.9) - (2.2)	3.6	3.6
$W^+W^-W^-$	+ (4.3) - (4.8)	+ (-0.5) - (0.5)	+ (4.3) - (4.9)	+ (3.2) - (2.8)	+ (-0.3) - (-0.3)	+ (3.3) - (2.8)	3.6	3.6
W^+W^+	+ (4.4) - (3.7)	+ (-0.2) - (0.2)	+ (4.4) - (3.7)	+ (3.5) - (2.7)	+ (-0.1) - (-0.1)	+ (3.5) - (2.7)	3.2	3.2
W^-W^-	+ (1.8) - (2.1)	+ (-0.1) - (0.1)	+ (1.8) - (2.1)	+ (2.8) - (1.9)	+ (-0.0) - (-0.0)	+ (2.8) - (1.9)	2.0	2.0
$t\bar{t}W \to 2L^+2\nu$	+ (3.7) - (5.1)	+ (-0.5) - (0.5)	+ (3.8) - (5.1)	+ (3.1) - (2.1)	+ (-0.3) - (-0.3)	+ (3.1) - (2.1)	3.6	3.6
$t\bar{t}W \to 2L^-2\nu$	+ (4.6) - (5.1)	+ (-0.6) - (0.6)	+ (4.6) - (5.2)	+ (3.3) - (2.7)	+ (-0.4) - (-0.4)	+ (3.3) - (2.8)	3.8	3.8
$t\bar{t}Z \to 2L^+2\nu$	+ (5.7) - (5.0)	+ (0.1) - (-0.0)	+ (5.7) - (5.0)	+ (3.1) - (2.7)	+ (0.3) - (0.3)	+ (3.1) - (2.7)	9.6	9.6
$t\bar{t}Z \to 2L^-2\nu$	+ (4.3) - (4.3)	+ (-0.2) - (0.3)	+ (4.3) - (4.3)	+ (2.6) - (2.4)	+ (-0.0) - (-0.0)	+ (2.6) - (2.4)	3.4	3.4
$LM0$	+ (3.0) - (4.1)	+ (-0.1) - (0.1)	+ (3.0) - (4.1)	+ (2.6) - (2.1)	+ (0.0) - (0.0)	+ (2.6) - (2.1)	2.6	2.6
$LM1$	+ (3.0) - (4.1)	+ (0.0) - (-0.1)	+ (3.0) - (4.1)	+ (2.5) - (2.1)	+ (0.2) - (0.2)	+ (2.5) - (2.1)	2.8	2.8
$LM2$	+ (3.0) - (4.3)	+ (-0.2) - (0.2)	+ (3.0) - (4.3)	+ (2.6) - (2.1)	+ (-0.0) - (-0.0)	+ (2.6) - (2.1)	2.5	2.5
$LM3$	+ (3.1) - (4.5)	+ (-0.3) - (0.3)	+ (3.1) - (4.5)	+ (2.6) - (2.2)	+ (-0.1) - (-0.1)	+ (2.6) - (2.2)	2.6	2.6
$LM4$	+ (3.1) - (4.3)	+ (-0.2) - (0.2)	+ (3.1) - (4.3)	+ (2.6) - (2.2)	+ (-0.0) - (-0.0)	+ (2.6) - (2.2)	2.5	2.5
$LM5$	+ (3.1) - (4.4)	+ (-0.3) - (0.3)	+ (3.1) - (4.4)	+ (2.6) - (2.2)	+ (-0.1) - (-0.1)	+ (2.6) - (2.2)	2.6	2.6
$LM6$	+ (3.1) - (4.3)	+ (-0.2) - (0.2)	+ (3.1) - (4.3)	+ (2.6) - (2.1)	+ (-0.0) - (-0.0)	+ (2.6) - (2.1)	2.5	2.5
$LM7$	+ (8.1) - (8.3)	+ (0.0) - (0.1)	+ (8.1) - (8.3)	+ (4.0) - (3.2)	+ (-0.2) - (-0.2)	+ (4.0) - (3.2)	11.0	11.0
$LM8$	+ (3.4) - (5.0)	+ (-0.6) - (0.6)	+ (3.5) - (5.0)	+ (2.9) - (2.3)	+ (-0.3) - (-0.3)	+ (2.9) - (2.4)	3.1	3.1
$LM9$	+ (7.2) - (8.9)	+ (-0.7) - (0.7)	+ (7.3) - (8.9)	+ (4.6) - (3.0)	+ (-0.9) - (-0.9)	+ (4.7) - (3.1)	5.4	5.4
$LM10$	+ (12.8) - (11.7)	+ (0.3) - (-0.2)	+ (12.8) - (11.7)	+ (5.8) - (4.9)	+ (-0.1) - (-0.1)	+ (5.8) - (4.9)	14.2	14.2
$LM11$	+ (3.1) - (4.4)	+ (-0.3) - (0.3)	+ (3.1) - (4.4)	+ (2.6) - (2.2)	+ (-0.1) - (-0.1)	+ (2.6) - (2.2)	2.6	2.6
$LM12$	+ (12.8) - (12.7)	+ (-0.0) - (0.0)	+ (12.8) - (12.7)	+ (5.8) - (4.7)	+ (-0.5) - (-0.5)	+ (5.8) - (4.7)	7.7	7.7
$LM13$	+ (3.0) - (4.2)	+ (-0.3) - (0.2)	+ (3.0) - (4.2)	+ (2.6) - (2.1)	+ (-0.1) - (-0.1)	+ (2.6) - (2.1)	2.5	2.5
$HM1$	+ (3.5) - (5.1)	+ (-0.6) - (0.6)	+ (3.6) - (5.2)	+ (2.9) - (2.4)	+ (-0.4) - (-0.4)	+ (3.0) - (2.4)	3.3	3.3
$HM2$	+ (3.7) - (5.3)	+ (-0.7) - (0.7)	+ (3.7) - (5.3)	+ (3.0) - (2.4)	+ (-0.4) - (-0.4)	+ (3.0) - (2.5)	3.4	3.4

$HM3$	+ (4.4) - (6.1)	+ (-0.8) - (0.8)	+ (4.5) - (6.1)	+ (3.4) - (2.6)	+ (-0.7) - (-0.7)	+ (3.5) - (2.6)	4.1	4.1
$HM4$	+ (7.0) - (8.6)	+ (-0.7) - (0.8)	+ (7.1) - (8.6)	+ (4.6) - (3.0)	+ (-1.0) - (-1.0)	+ (4.7) - (3.1)	5.5	5.5

Table C.1: The results of the PDF and α_s uncertainty determination. All values in (%) variation on the final event yield.

Bibliography

[1] D. Griffith, "Introduction to Elementary Particles". WILEY-VCH Verlag, Weinheim, 2008.

[2] Particle Data Group, "Review of Particle Physics", *Journal of Physics G* 37 (2010).

[3] CERN, "CERN experiments observe particle consistent with long-sought Higgs boson", *CERN Press Release* (July, 2012).

[4] CMS Collaboration, "Observation of a new boson with a mass near 125 GeV", *http://cdsweb.cern.ch/record/1460438* (2012).

[5] L. Alvarez-Gaume and J. Ellis, "Eyes on a prize particle", *Nat. Phys.* 7 (2011), no. 1, 2–3. Editorial Material.

[6] V. C. Rubin and W. K. Ford, Jr., "Rotation of the Andromeda Nebula from a Spectroscopic Survey of Emission Regions", *APJ* 159 (February, 1970) 379. doi:10.1086/150317.

[7] S. P. Martin, "A Supersymmetry Primer", arXiv:hep-ph/9709356.

[8] P. Binétruy, "Supersymmetry Theory, Experiment, and Cosmology". Oxford University Press Inc., New York, 2007.

[9] S. AbdusSalam, B. Allanach, H. Dreiner et al., "Benchmark Models, Planes, Lines and Points for Future SUSY Searches at the LHC", *Eur.Phys.J.* C71 (2011) 1835, arXiv:1109.3859. doi:10.1140/epjc/s10052-011-1835-7.

[10] L. E. Ibanez and G. G. Ross, "Discrete gauge symmetries and the origin of baryon and lepton number conservation in supersymmetric versions of the standard model", *Nuclear Physics B* 368 (1992), no. 1, 3 – 37. doi:10.1016/0550-3213(92)90195-H.

[11] H. K. Dreiner, C. Luhn, and M. Thormeier, "What is the discrete gauge symmetry of the minimal supersymmetric standard model", *Phys. Rev. D* 73 (Apr, 2006) 075007. doi:10.1103/PhysRevD.73.075007.

[12] H. K. Dreiner, M. Hanussek, J.-S. Kim et al., "Neutrino masses and mixings in the baryon triality constrained minimal supersymmetric standard model", *Phys.Rev.* D84 (2011) 113005, arXiv:1106.4338. doi:10.1103/PhysRevD.84.113005.

[13] D0 Collaboration Collaboration, "Search for resonant second generation slepton production at the Tevatron", *Phys.Rev.Lett.* 97 (2006) 111801, arXiv:hep-ex/0605010. doi:10.1103/PhysRevLett.97.111801.

[14] H. Dreiner and T. Stefaniak, "Bounds on R-parity Violation from Resonant Slepton Production at the LHC", arXiv:1201.5014.

[15] B. C. Allanach, A. Dedes, and H. K. Dreiner, "R-parity violating minimal supergravity model", *Phys. Rev. D* 69 (Jun, 2004) 115002. doi:10.1103/PhysRevD.69.115002.

[16] CMS Collaboration, "Observed limits from several 2011 CMS SUSY searches plotted in the CMSSM (m_0,$m1/2$) plane", *https://twiki.cern.ch/twiki/pub/CMSPublic/PhysicsResultsSUS/CMS_SUSY_2011Limits5fb_tanb10.pdf* (2011).

[17] C. Autermann, "Resonant Second Generation Slepton Production at the Tevatron". PhD thesis, RWTH Aachen University, Dec., 2006.

[18] L. Evans and P. Bryant, "LHC Machine", *Journal of Instrumentation* 3 (2008), no. 08, S08001.

[19] CERN, "The CERN accelerator complex", *http://cdsweb.cern.ch/record/1260465* (2008).

[20] ATLAS Collaboration, "The ATLAS Experiment at the CERN Large Hadron Collider", *Journal of Instrumentation* 3 (2008), no. 08, S08003.

[21] CMS Collaboration, "The CMS experiment at the CERN LHC", *Journal of Instrumentation* 3 (2008), no. 08, S08004.

[22] LHCb Collaboration, "The LHCb Detector at the LHC", *Journal of Instrumentation* 3 (2008), no. 08, S08005.

[23] ALICE Collaboration, "The ALICE experiment at the CERN LHC", *Journal of Instrumentation* 3 (2008), no. 08, S08002.

[24] CMS Collaboration, "CMS-PHO-GEN-2012-002-5", *http://cdsweb.cern.ch/record/1433717* (2012).

[25] V. KarimÃ¤ki, "The CMS tracker system project: Technical Design Report". Technical Design Report CMS. CERN, Geneva, 1997.

[26] "The CMS electromagnetic calorimeter project: Technical Design Report". Technical Design Report CMS. CERN, Geneva, 1997.

[27] "The CMS hadron calorimeter project: Technical Design Report". Technical Design Report CMS. CERN, Geneva, 1997.

[28] "The CMS muon project: Technical Design Report". Technical Design Report CMS. CERN, Geneva, 1997.

[29] R. Frühwirth, "Application of Kalman filtering to track and vertex fitting", *NIM A* 262 (1987), no. 2, 444 – 450. doi:10.1016/0168-9002(87)90887-4.

[30] CMS Collaboration, "CMS Physics Technical Design Report Volume I: Detector Performance and Software". Technical Design Report CMS. CERN, 2006.

[31] CMS Collaboration, "Muon Reconstruction in the CMS Detector", *CMS Note* AN-2008/097 (2008).

[32] S. Baffioni, C. Charlot, F. Ferri et al., "Electron reconstruction in CMS", *CMS Note* CMS NOTE-2006/040 (2006).

[33] M. Cacciari, G. P. Salam, and G. Soyez, "The anti- k t jet clustering algorithm", *Journal of High Energy Physics* 2008 (2008) 063. doi:doi:10.1088/1126-6708/2008/04/063.

[34] S. Catani, Y. Dokshitzer, M. Seymour et al., "Longitudinally-invariant kT-clustering algorithms for hadron-hadron collisions", *Nuclear Physics B* 406 (1993), no. 1, 187 – 224. doi:10.1016/0550-3213(93)90166-M.

[35] Y. L. Dokshitzer, G. Leder, S. Moretti et al., "Better jet clustering algorithms", *JHEP* 9708 (1997) 001, arXiv:hep-ph/9707323.

[36] CMS Collaboration, "Particle-Flow Event Reconstruction in CMS and Performance for Jets, Taus, and MET", *CMS Physics Analysis Summary* CMS-PAS-PFT-09-001 (2009).

[37] J. Alwall, M. Herquet, F. Maltoni et al., "MadGraph 5 : Going Beyond", *JHEP* 1106 (2011) 128, arXiv:1106.0522. doi:10.1007/JHEP06(2011)128.

[38] T. Sjöstrand, S. Mrenna, and P. Skands, "PYTHIA 6.4 physics and manual", *Journal of High Energy Physics* 2006 (2006), no. 05, 026.

[39] S. Frixione, P. Nason, and G. Ridolfi, "The POWHEG-hvq manual version 1.0", arXiv:0707.3081.

[40] S. Jadach, J. H. Kühn, and Z. Wąs, "TAUOLA - a library of Monte Carlo programs to simulate decays of polarized τ leptons", *Computer Physics Communications* 64 (1991), no. 2, 275 – 299. doi:10.1016/0010-4655(91)90038-M.

[41] N. Kidonakis, "Higher-order corrections to top-antitop pair and single top quark production", arXiv:0909.0037.

[42] N. Kidonakis, "NNLL resummation for s-channel single top quark production", *Phys.Rev.* D81 (2010) 054028, arXiv:1001.5034. doi:10.1103/PhysRevD.81.054028.

[43] N. Kidonakis, "Next-to-next-to-leading-order collinear and soft gluon corrections for t-channel single top quark production", *Phys.Rev.* D83 (2011) 091503, arXiv:1103.2792. doi:10.1103/PhysRevD.83.091503.

[44] N. Kidonakis, "Two-loop soft anomalous dimensions for single top quark associated production with a W^- or H^-", *Phys.Rev.* D82 (2010) 054018, arXiv:1005.4451. doi:10.1103/PhysRevD.82.054018.

[45] T. Binoth, G. Ossola, C. Papadopoulos et al., "NLO QCD corrections to tri-boson production", *JHEP* 0806 (2008) 082, arXiv:0804.0350. doi:10.1088/1126-6708/2008/06/082.

[46] CMS Collaboration, "Standard Model Cross Sections for CMS at 7 TeV", *https://twiki.cern.ch/twiki/bin/view/CMS/StandardModelCrossSections*. accessed Aug. 2012.

[47] CMS Collaboration, "Search for resonant smuon production", *CMS Note* AN-2012/023 (2012).

[48] CMS Collaboration, "SUSY benchmarks", *https://twiki.cern.ch/twiki/bin/view/CMS/SUSYBenchmarks*. accessed Aug. 2012.

[49] CMS Collaboration, "MSUGRA Test Points for CMS", *http://cmsdoc.cern.ch/cms/PRS/susybsm/msugra_testpts/msugra_testpts.html*. accessed Aug. 2012.

[50] B. Allanach, "SOFTSUSY: a program for calculating supersymmetric spectra", *Comput.Phys.Commun.* 143 (2002) 305–331, arXiv:hep-ph/0104145. doi:10.1016/S0010-4655(01)00460-X.

[51] B. Allanach and M. Bernhardt, "Including R-parity violation in the numerical computation of the spectrum of the minimal supersymmetric standard model: SOFTSUSY", *Comput.Phys.Commun.* 181 (2010) 232–245, arXiv:0903.1805. doi:10.1016/j.cpc.2009.09.015.

[52] F. E. Paige, S. D. Protopopescu, H. Baer et al., "ISAJET 7.69: A Monte Carlo event generator for pp, anti-p p, and e+e- reactions", arXiv:hep-ph/0312045.

[53] G. Corcella, I. Knowles, G. Marchesini et al., "HERWIG 6: An Event generator for hadron emission reactions with interfering gluons (including supersymmetric processes)", *JHEP* 0101 (2001) 010, arXiv:hep-ph/0011363.

[54] S. Moretti, K. Odagiri, P. Richardson et al., "Implementation of supersymmetric processes in the HERWIG event generator", *JHEP* 0204 (2002) 028, arXiv:hep-ph/0204123.

[55] H. K. Dreiner, S. Grab, M. Krämer et al., "Supersymmetric NLO QCD corrections to resonant slepton production and signals at the Fermilab Tevatron and the CERN LHC", *Phys. Rev. D* 75 (Feb, 2007) 035003. doi:10.1103/PhysRevD.75.035003.

[56] CMS Collaboration, "Performance of muon identification in pp collisions at $\sqrt{s} = 7$ TeV", *CMS Physics Analysis Summary* CMS PAS-2010/002 (2010).

[57] M. Mulders, I. Bloch, E. James et al., "Muon Identification in CMS", *CMS Note* AN-2008/098 (2008).

[58] N. Saoulidou, "Particle Flow Jet Identification Criteria", *CMS Note* AN-2010/003 (2010).

[59] CMS Collaboration, "JetID", *https://twiki.cern.ch/twiki/bin/view/CMS/JetID#Documentation*. accessed Aug. 2012.

[60] CMS Collaboration, "Simple Cut Based Ele ID", *https://twiki.cern.ch/twiki/bin/viewauth/CMS/SimpleCutBasedEleID*. accessed Aug. 2012.

[61] CMS Collaboration, "Study of photon conversion rejection at CMS", *CMS Note* AN-2009/159 (2009).

[62] CMS Collaboration, "Instructions on filters for HBHE noise for 2011 analysis", *https://twiki.cern.ch/twiki/bin/view/CMS/HBHEAnomalousSignals2011*. acessed September 2012.

[63] D. Barge, C. Campagnari, P. Kalavase et al., "Fake Rates for dilepton Analyses", *CMS Note* AN-2010/257 (2010).

[64] D. Barge, C. Campagnari, P. Kalavase et al., "Inclusive search for New Physics with Same-Sign Dileptons using early LHC data", *CMS Note* AN-2010/247 (2010).

[65] W. Andrews, D. Barge, G. Bauer et al., "Search for Higgs Boson Decays to Two W Bosons in the Fully Leptonic Final State $\sqrt{s} = 7$ TeV with 2011 data of CMS detector", *CMS Note* AN-2011/148 (2011).

[66] W. Clarida, J. Ellison, F. Giordano et al., "Search for Isosinglet Heavy Majorana Neutrinos in Same Sign Dilepton Events in pp Collisions at $\sqrt{s} = 7$ GeV", *CMS Note* AN-11/382 (2011).

[67] CMS Collaboration, "Pileup Scenarios", *https://twiki.cern.ch/twiki/bin/view/CMS/Pileup_MC_Gen_Scenarios*. accessed Aug. 2012.

[68] CMS Collaboration, "Pileup Reweighting for 2011 Data and Monte Carlo", *https://twiki.cern.ch/twiki/bin/view/CMS/Pileup_*2011*_Reweighting*. accessed Aug. 2012.

[69] CMS Collaboration, "Estimating Systematic Errors Due to Pileup Modeling", *https://twiki.cern.ch/twiki/bin/viewauth/CMS/PileupSystematicErrors*. accessed Aug. 2012.

[70] A. Martin, W. Stirling, R. Thorne et al., "Parton distributions for the LHC", *IPPP/08/95, DCPT/08/190, Cavendish-HEP-08/16* (2009) `arXiv:0901.0002v3`. `doi:10.1140/epjc/s10052-009-1072-5`.

[71] S. Alekhin, S. Alioli, R. D. Ball et al., "The PDF4LHC Working Group Interim Report", `arXiv:1101.0536`.

[72] PDF4LHC Group, "Recommendation for LHC cross section calculations", *http://www.hep.ucl.ac.uk/pdf4lhc/*.

[73] PDF4LHC Group, "PDF4LHC Recommendations", *www.hep.ucl.ac.uk/pdf4lhc/PDF4LHCrecom.pdf*.

[74] PDF4LHC Group, "Practical implementation of the PDF4LHC recipe", *www.hep.ucl.ac.uk/pdf4lhc/PDF4LHC_practical_guide.pdf*.

[75] H.-L. Lai, M. Guzzi, J. Huston et al., "New parton distributions for collider physics", *Phys. Rev.* D82 (2010) 074024, `arXiv:1007.2241`. `doi:10.1103/PhysRevD.82.074024`.

[76] G. Watt and R. Thorne, "Study of Monte Carlo approach to experimental uncertainty propagation with MSTW 2008 PDFs", *CERN-PH-TH/2012-132; LCTS/2012-11* (2012) `arXiv:1205.4024v1`.

[77] NNPDF Collaboration Collaboration, "Unbiased global determination of parton distributions and their uncertainties at NNLO and at LO", *Nucl.Phys.* B855 (2012) 153–221, arXiv:1107.2652. doi:10.1016/j.nuclphysb.2011.09.024.

[78] R. D. Ball, V. Bertone, F. D. Cerutti et al., "On the Impact of NMC Data on NLO and NNLO Parton Distributions and Higgs Production at the Tevatron and the LHC", *Phys. Lett. B704* (2011) 36, arXiv:1102.3182. doi:10.1016/j.physletb.2011.08.055.

[79] J. Pumplin, D. Stump, J. Huston et al., "New generation of parton distributions with uncertainties from global QCD analysis", *JHEP* 0207 (2002) 012, arXiv:hep-ph/0201195.

[80] CMS Collaboration Collaboration, "Measurement of the Underlying Event Activity at the LHC with $\sqrt{s} = 7$ TeV and Comparison with $\sqrt{s} = 0.9$ TeV", *JHEP* 1109 (2011) 109, arXiv:1107.0330. doi:10.1007/JHEP09(2011)109.

[81] "LHAPDF the Les Houches Accord PDF Interface", *http://lhapdf.hepforge.org/*. accessed Aug. 2012.

[82] H. Dreiner, S. Grab, M. Kramer et al., "Supersymmetric NLO QCD corrections to resonant slepton production and signals at the Tevatron and the CERN LHC", *Phys.Rev.* D75 (2007) 035003, arXiv:hep-ph/0611195. doi:10.1103/PhysRevD.75.035003.

[83] CMS Collaboration, "Absolute Calibration of the Luminosity Measurement at CMS: Winter 2012 Update", *CMS Physics Analysis Summary* CMS-PAS-SMP-12-008 (2012).

[84] CMS Collaboration, "Jet Energy Correction Subgroup", *https://twiki.cern.ch/twiki/bin/view/CMS/JetEnergyScale*. accessed Aug. 2012.

[85] CMS, "Performance of muon reconstruction and identification in pp collisions at $\sqrt{s} = 7$ TeV", *CMS Physics Analysis Summary* CMS PAS MUO-10-004 (2010).

[86] A. L. Read, "Presentation of search results: the CL s technique", *Journal of Physics G: Nuclear and Particle Physics* 28 (2002), no. 10, 2693.

[87] A. L. Read, "Modified frequentist analysis of search results (the CL_s method).", *1st Workshop on Confidence Limits* (Jan., 2000) 81–101.

[88] CMS, ATLAS, LHC Higgs Combination Group Collaboration, "Procedure for the LHC Higgs boson search combination in Summer 2011", *CMS Note* CMS NOTE-2011/005 (2011).

[89] L. Moneta, K. Cranmer, G. Schott et al., "The RooStats project", in *Proceedings of the 13th International Workshop on Advanced Computing and Analysis Techniques in Physics Research. February 22-27, 2010, Jaipur, India.* 2010. arXiv:1009.1003.

[90] CMS Collaboration, "Documentation of the RooStats-based statistics tools for Higgs PAG", *https://twiki.cern.ch/twiki/bin/viewauth/CMS/SWGuideHiggsAnalysisCombinedLimit*. accessed September 2012.

[91] CMS Collaboration, "Performance of CMS muon reconstruction in cosmic-ray events", *Journal of Instrumentation* 5 (March, 2010) 3022, arXiv:0911.4994. doi:10.1088/1748-0221/5/03/T03022.

Danksagung

Zum Schluss möchte ich mich noch bei einigen Menschen bedanken, ohne die diese Arbeit in dieser Form nicht hätte entstehen können.

Zu erst danke ich Prof. Thomas Hebbeker für die Gelegenheit, in einer spannenden Zeit für die Teilchenphysik, an einem interessanten Thema arbeiten zu können. Nicht nur die Arbeit im Institut, sondern auch die Erfahrung einer großen Kollaboration sowie die gelegentlichen Dienstreisen haben mir große Freude bereitet.

Ich danke Prof. Christopher Wiebusch, dass er sich bereit erklärt hat die Rolle des Zweitgutachters zu übernehmen.

Ein weiterer Dank geht an die Aachener RPV-Gruppe. Dort insbesondere an Martin Weber für Hilfestellungen, Diskussionen, Kritiken, Ratschläge, Koordination und vieles mehr. Das gleiche gilt für Arnd Meyer. Ein Riesenlob an Lars Sonnenschein für seine Mühen bei der Signalproduktion, die zu solch schönen Resultaten geführt haben. In dem Zusammenhang möchte auch Dominique Dresen danken für sein Limitprogramm, sowie Daniel Teyssier für seine Beteiligung an der Analyse und Andreas Güth für viele Hilfreiche Beiträge.

Vielen Dank auch an alle, die sich um die (weiter-) Entwicklung der verwendeten Software gekümmert haben. Das heißt, vielen Dank an Carsten Magaß, den Autor unseres Analyseframeworks, als auch an die Kollegen aus dem UnBüro, insbesondere Klaas Padeken und Sebastian Thüer, die sich um die Weiterentwicklung gekümmert haben.

Die gesamte Arbeitsgruppe hat für eine sehr angenehme Atmosphäre gesorgt. Dankend erwähnen möchte ich noch Deborah Duchardt für ihre Ratschläge zu Begin meiner Zeit, Markus Merschmeyer für das Korrekturlesen eines Teils dieser Arbeit, sowie für hilfreiche Tipps oder nette Gespräche Stefan Schmitz, Mark Olschewski, Paul Papacz, Holger Pieta und Michael Brodski.

Zu guter letzt gilt mein Dank meinen Eltern, die mir dieses Studium ermöglicht haben.

Selbständigkeitserklärung

Hiermit erkläre ich, dass ich die Arbeit selbstständig und ohne fremde Hilfe verfasst habe. Zitate habe ich kenntlich gemacht und keine anderen als die genannten Hilfsmittel oder Quellen verwendet.

Aachen, den 04.10.2012

Matthias Endres